

การพัฒนาผลิตภัณฑ์วัสดุสารอินทรีย์ที่มีสมรรถนะสูงในการวิเคราะห์พลังงานรังสีแกมมา



นาย มานิตย์ จิตรภักดี

ศูนย์วิทยทรัพยากร

จุฬาลงกรณ์มหาวิทยาลัย

วิทยานิพนธ์นี้เป็นส่วนหนึ่งของการศึกษาตามหลักสูตรปริญญาวิศวกรรมศาสตรดุษฎีบัณฑิต
สาขาวิชาวิศวกรรมนิวเคลียร์ ภาควิชานิวเคลียร์เทคโนโลยี

คณะวิศวกรรมศาสตร์ จุฬาลงกรณ์มหาวิทยาลัย

ปีการศึกษา 2552

ลิขสิทธิ์ของจุฬาลงกรณ์มหาวิทยาลัย

DEVELOPMENT OF HIGH PERFORMANCE INORGANIC SCINTILLATOR
FOR GAMMA-RAY SPECTROSCOPY



Mr. Manit Jitpukdee

ศูนย์วิทยทรัพยากร

A Dissertation Submitted in Partial Fulfillment of the Requirements

for the Degree of Doctor of Engineering Program in Nuclear Engineering

Department of Nuclear Technology

Faculty of Engineering

Chulalongkorn University

Academic year 2009

Copyright of Chulalongkorn University

จุฬาลงกรณ์มหาวิทยาลัย

Thesis Title DEVELOPMENT OF HIGH PERFORMANCE INORGANIC
 SCINTILLATOR FOR GAMMA-RAY SPECTROSCOPY

By Mr. Manit Jitpukdee

Field of Study Nuclear Technology

Thesis Advisor Doonyapong Wongsawaeng, Ph.D.

Thesis Co-Advisor Associate Professor Virul Mangclaviraj

Accepted by the Faculty of Engineering, Chulalongkorn University in Partial
 Fulfillment of the Requirements for the Doctoral Degree

..... *B. Lerdhirunwong* Dean of the Faculty of Engineering
 (Associate Professor Boonsom Lerdhirunwong, Dr. Ing.)

THESIS COMMITTEE

..... *S. Chanyotha* Chairman
 (Associate Professor Supitcha Chanyotha, Ph.D.)

..... *Doonyapong Wongsawaeng* Thesis Advisor
 (Doonyapong Wongsawaeng, Ph.D.)

..... *Virul Mangclaviraj* Thesis Co-Advisor
 (Associate Professor Virul Mangclaviraj)

..... *Nares Chankow* Examiner
 (Associate Professor Nares Chankow)

..... *Kajornyod Yoodee* External Examiner
 (Assistant Professor Kajornyod Yoodee, Ph.D.)

..... *T. Osochan* External Examiner
 (Assistant Professor Tanakorn Osochan, Ph.D.)

ศูนย์วิจัยและพัฒนา
 จุฬาลงกรณ์มหาวิทยาลัย

มานิตย์ จิตรภักดี : การพัฒนาผลึกวัดรังสีชนิดสารอนินทรีย์ที่มีสมรรถนะสูงในการวิเคราะห์พลังงานรังสีแกมมา. (DEVELOPMENT OF HIGH PERFORMANCE INORGANIC SCINTILLATOR FOR GAMMA-RAY SPECTROSCOPY) อ. ที่ปรึกษาวิทยานิพนธ์หลัก : อ.ดร. ศุภยพงศ์ วงศ์แสง, อ. ที่ปรึกษาวิทยานิพนธ์ร่วม : รศ.วิรุฬห์ มังคละวิรัช, 94 หน้า.

งานวิจัยนี้เป็นการพัฒนาผลึกวัดรังสีชนิดสารอนินทรีย์สมรรถนะสูงสำหรับใช้วิเคราะห์พลังงานรังสีแกมมา ในส่วนแรกได้ออกแบบเตาปลูกผลึกแบบสองโซน ที่ควบคุมการเคลื่อนที่ของเกรตของอุณหภูมิ ประยุกต์เข้ากับระบบปลูกผลึกบริดจ์แมนแบบดั้งเดิม เทคนิคนี้ช่วยให้ไม่ต้องใช้ระบบกลไกสำหรับขับเคลื่อนท่อปลูกผลึก จึงลดการสั่นสะเทือนที่อาจจะเกิดขึ้นทำให้ได้ผลึกที่มีคุณภาพดีขึ้น ส่วนที่สองได้พัฒนาการเตรียมสารและอุปกรณ์สำหรับกระบวนการปลูกผลึก จากนั้นทดลองปลูกผลึก CsI:TI, LaCl₃:Ce และ Ba₂CsI₅:TI

ผลการพัฒนาพบว่าเตาปลูกผลึกแบบเคลื่อนที่ของเกรตของอุณหภูมิ ให้อุณหภูมิบริเวณโซนปลูกผลึกมีความเสถียรดีกว่า มีความคลาดเคลื่อนของเกรตของอุณหภูมิน้อยกว่า 2% สามารถปลูกผลึก CsI:TI ขนาดเส้นผ่านศูนย์กลาง $\varnothing 22 \times 22$ mm ได้ง่าย จากสารเริ่มต้นที่ความบริสุทธิ์ต่ำ 99.9% เมื่อใช้อัตราการก่อผลึก 1 mm/hr เกรตของอุณหภูมิ 25.5°C/cm และอัตราการเคลื่อนที่ของเกรตของอุณหภูมิ 2.5°C/hr จากการทดสอบสมรรถนะในการวิเคราะห์สเปกตรัมพลังงาน 662 keV ของ Cs-137 พบว่ามีความสามารถในการแจกแจงพลังงาน 7.53% ประสิทธิภาพวัดพีคพลังงาน 10.35% ที่อัตราพีคต่อคอมปีตัน (P/C) เท่ากับ 4.58:1 ส่วนผลการปลูกผลึก LaCl₃:Ce และ Ba₂CsI₅:TI พบปัญหาการไวต่อความชื้นและออกซิเจนของสารในระหว่างการเตรียมสารเริ่มต้น ทำให้การก่อผลึกไม่สมบูรณ์ ผลึกที่ปลูกได้ขุ่นและแตกออกเป็นชิ้นเล็ก โดยได้นำเสนอวิจารณ์ผลไว้ในวิทยานิพนธ์นี้

ศูนย์วิทยทรัพยากร

จุฬาลงกรณ์มหาวิทยาลัย

ภาควิชา.....นิเวศวิทยเทคโนโลยี
สาขาวิชา.....วิศวกรรมนิเวศวิทย
ปีการศึกษา.....2552

ลายมือชื่อนิสิต มานิตย์ จิตรภักดี
ลายมือชื่อ อ.ที่ปรึกษาวิทยานิพนธ์หลัก วิรุฬห์ มังคละวิรัช
ลายมือชื่อ อ.ที่ปรึกษาวิทยานิพนธ์ร่วม วิรุฬห์ มังคละวิรัช

487182.321 : MAJOR NUCLEAR ENGINEERING

KEYWORDS : MOVING-TEMPERATURE-GRADIENT / BRIDGMAN-STOCKBARGER /
SCINTILLATOR / CsI:TI / LaCl₃:Ce / Ba₂CsI₅:TI

MANIT JITPUKDEE : DEVELOPMENT OF HIGH PERFORMANCE
INORGANIC SCINTILLATOR FOR GAMMA-RAY SPECTROSCOPY. THESIS
ADVISOR : DOONYAPONG WONGSAWAENG, Ph.D., THESIS CO-ADVISOR :
ASSOCIATE PROFESSOR VIRUL MANGCLAVIRAJ, 94 pp.

This research was aimed to develop high performance inorganic scintillators for gamma-ray spectroscopy. In the first part of the experimental work, a dual zone vertical moving-temperature-gradient furnace was developed and applied to the Bridgman method. This technique helps to eliminate a driving mechanism leading to a reduction of vibrations which can adversely affect crystal growth quality. In the second part of the experimental work, charge preparation and equipment for growing process were developed. Crystal growth experiments of CsI:TI, LaCl₃:Ce and Ba₂CsI₅:TI were performed.

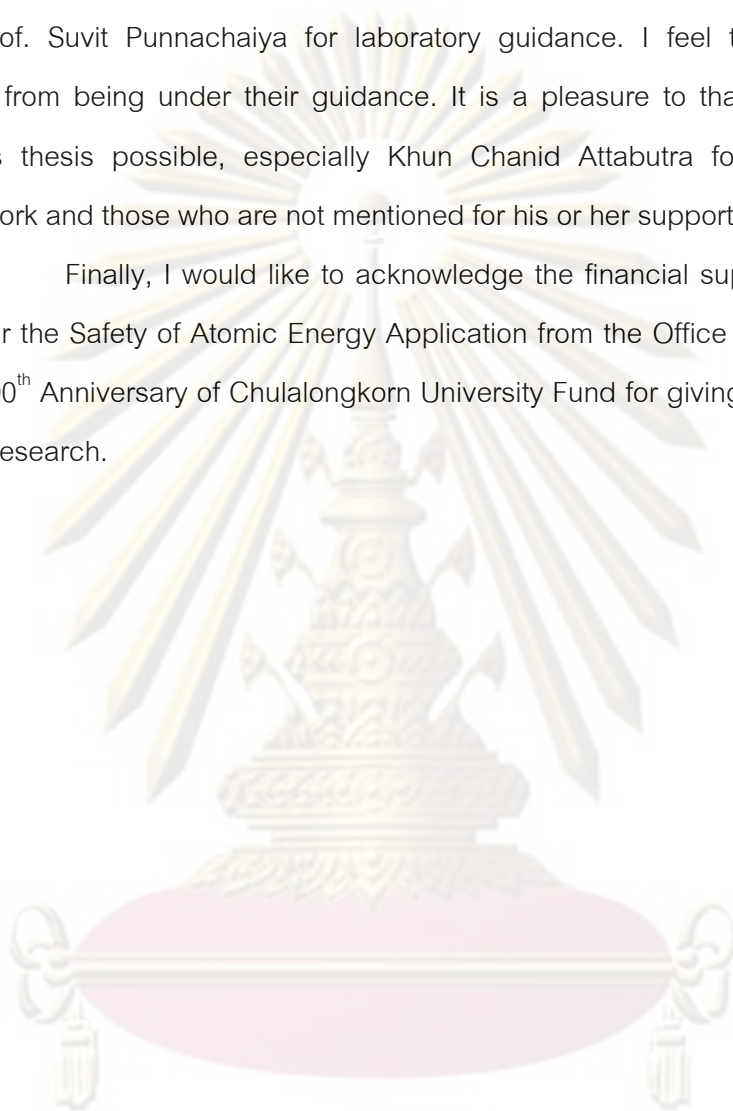
Tested results of the moving-temperature-gradient furnace illustrated that the growth zone exhibited a better thermal stability than the traditional Bridgman system. Only an error of less than 2% in the temperature gradient was found. The furnace was capable of growing simple CsI(TI) crystal of $\varnothing 22 \times 22$ mm size, starting from powder element of 99.9% purity, using 1 mm/hr growth rate with 25.5°C/cm temperature gradient and 2.5°C/hr temperature gradient drift rate. The analyzed crystal performance using the 662 keV energy of Cs-137 spectrum revealed the energy resolution of 7.53% and the intrinsic peak detection efficiency of 10.35% at 4.58:1 peak to Compton ratio. For LaCl₃:Ce and Ba₂CsI₅:TI grown crystals, the chemical activity of oxygen and moisture presented problem with charge preparation and affected crystal growth perfection, as grown crystals were foggy and cracked into small pieces. These experimental results were presented in this dissertation.

Department : Nuclear Technology Student's Signature *manit*
Field of Study : Nuclear Engineering Advisor's Signature *Doonyapong*
Academic Year : 2009 Co-Advisor's Signature *Virul Mangclaviraj*

Acknowledgments

I am gratefully thankful to my supervisors, Dr. Doonyapong Wongsawaeng and Prof. Virul Manglaviraj for their guidance. I also would like to thank Assist. Prof. Suvit Punnachaiya for laboratory guidance. I feel that I have greatly benefited from being under their guidance. It is a pleasure to thank those who help make this thesis possible, especially Khun Chanid Attabutra for supporting glass blowing work and those who are not mentioned for his or her support on my research.

Finally, I would like to acknowledge the financial support from the OAP GRANT for the Safety of Atomic Energy Application from the Office of Atoms for Peace and The 90th Anniversary of Chulalongkorn University Fund for giving me an opportunity to do my research.



ศูนย์วิทยทรัพยากร
จุฬาลงกรณ์มหาวิทยาลัย

Contents

	Page
Abstract (Thai).....	iv
Abstract (English).....	v
Acknowledgement.....	vi
Contents.....	vii
List of tables.....	x
List of figures.....	xi
Chapter	
I INTRODUCTION.....	1
1.1 Background on problems of interest.....	1
1.2 Thesis objective.....	2
1.3 Scope of work.....	2
1.4 Expected benefit.....	3
II THEORY AND LITERATURE REVIEW.....	4
2.1 Bridgman-Stockbarger crystal growing method.....	4
2.1.1 Bridgman technique.....	4
2.1.2 Crystal growth.....	5
2.2 Scintillator.....	5
2.2.1 The good properties of material for scintillator.....	6
2.2.2 Scintillator mechanism.....	7
2.2.3 Types of scintillation process.....	10
2.2.4 Inorganic scintillators doped with cerium.....	12
2.2.5 Scintillation crystal evaluation.....	12
2.2.5.1 Thermoluminescence.....	12
2.2.5.2 Emission spectrum.....	13
2.2.5.3 Energy resolution.....	13
2.2.5.4 Pulse height measurement.....	15
2.2.5.5 Detection efficiency.....	16

Contents (Continue)

Chapter	Page
2.2.5.6 Scintillation decay time.....	17
2.3 Photosensitive device.....	18
2.3.1 Photomultiplier tube.....	18
2.3.2 Photodiode.....	20
2.4 Literature review.....	23
2.4.1 Modified Bridgman-Stockbarger method.....	23
2.4.2 Rare earth halide preparation.....	25
2.4.3 Commercial and high performance scintillator.....	26
2.4.4 Scintillator performance testing method.....	30
III DESIGN AND DEVELOPMENT.....	32
3.1 Equipment design and construction	32
3.1.1 Crystal growing furnace	32
3.1.2 Charge crucible.....	37
3.1.3 Refractory tube.....	39
3.1.4 Glove box.....	41
3.2 Scintillation crystal assembly.....	42
3.2.1 Scintillation crystal encapsulation	42
3.2.2 Scintillator coupling.....	43
3.2 Energy spectroscopy system.....	45
3.2.1 Test system configuration.....	45
3.2.2 Front-end under test stage	46
IV EXPERIMENTS AND RESULTS.....	47
4.1 Furnace performance test.....	48
4.1.1 Temperature gradient of conventional Bridgman furnace.....	48
4.1.2 Temperature gradient of moving-temperature-gradient furnace	49
4.1.3 Evaluation of furnace.....	52

Contents (Continue)

Chapter	Page
4.2 Crystal growing.....	52
4.2.1 Commercial CsI:Tl crystal growing.....	53
4.2.2 High performance LaCl ₃ :Ce crystal growing.....	55
4.2.3 Ternary compound of Ba ₂ CsI ₅ :Tl crystal growing.....	57
4.3 Crystal performance test.....	58
4.3.1 CsI:Tl scintillation crystal	59
4.3.2 LaCl ₃ :Ce scintillation crystal.....	66
4.3.3 Ba ₂ CsI ₅ :Tl scintillation crystal.....	67
V CONCLUSION DISCUSSION AND SUGGESTION.....	70
5.1 Conclusion.....	70
5.1.1 Furnace development.....	70
5.1.2 Charge material preparation.....	71
5.1.3 Crystals growing.....	71
5.2 Discussion.....	73
5.3 Suggestion.....	75
References.....	76
Appendices.....	80
Appendix A Microstepping drive specification.....	81
Appendix B Photosensitive device specification.....	84
Appendix C Grown crystal properties.....	88
Appendix D Commercial NaI:Tl spectroscopy.....	89
Appendix E Calculation of intrinsic peak efficiency and peak to Compton ratio.....	91
Biography.....	94

List of Tables

	Page
Table 2.1 Materials commonly used to produce photodiodes.....	21
Table 4.1 The growth crystal quality from conventional and modified Bridgman furnace.....	52
Table 4.2 Charge material preparation for 10 mm diameter for CsI:Tl.....	54
Table 4.3 Charge material preparation of 10 mm diameter crystals of Ba ₂ CsI ₅ :Tl	57
Table 4.4 Results of energy resolution and relative pulse height of CsI:Tl.....	59
Table 4.5 The grown crystal quality from conventional and modified Bridgman furnaces.....	61
Table 4.6 The scintillated light yield enhancement of CsI:Tl crystals.....	62
Table 4.7 Results of the detection efficiency of grown CsI:Tl crystal.....	66
Table 4.8 Results of energy resolution and relative pulse height of Ba ₂ CsI ₅ :Tl....	67
Table 5.1 Summary on tested results of grown scintillation crystals.....	73



ศูนย์วิทยทรัพยากร
จุฬาลงกรณ์มหาวิทยาลัย

List of Figures

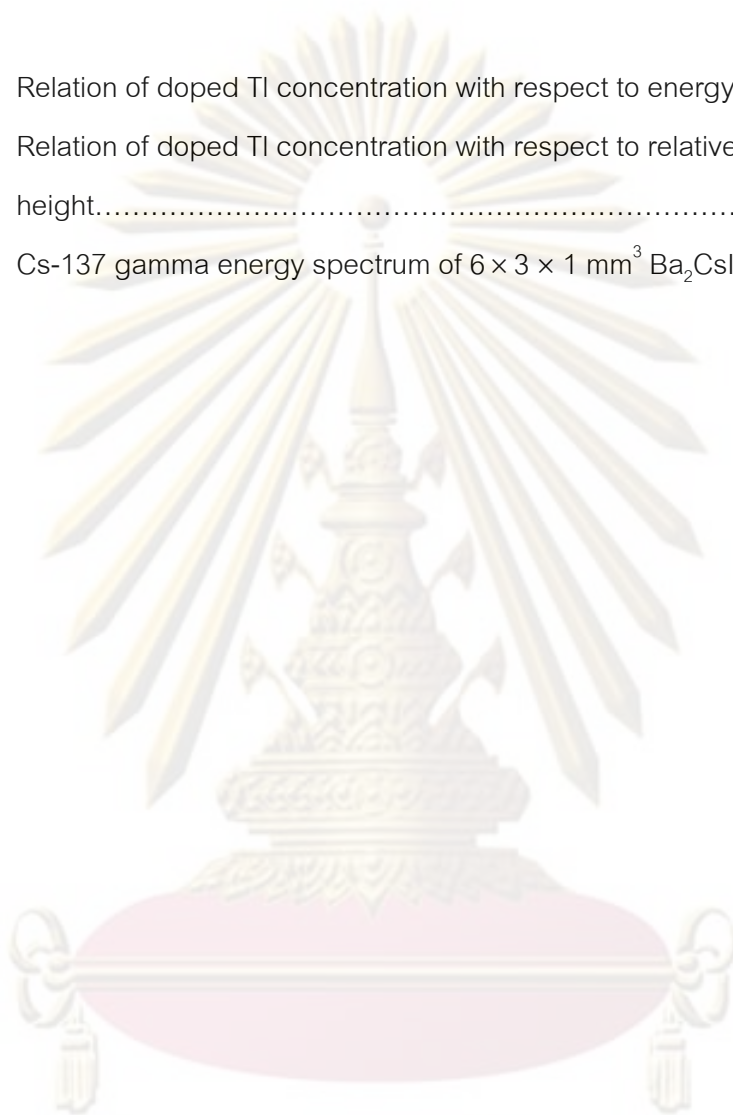
	Page
Fig. 1.1 Radiation detection of scintillation detector.....	1
Fig. 2.1 Diagram of conventional Bridgman-Stockbarger method.....	4
Fig. 2.2 Energy band gap and scintillation mechanism of scintillator.....	9
Fig. 2.3 Definition of detector resolution in Gaussian shape peak.....	13
Fig. 2.4 The full energy peak in a differential pulse height spectrum.....	17
Fig. 2.5 Conventional method for determination of scintillation decay time.....	17
Fig. 2.6 Photosensitive devices for scintillator.....	18
Fig. 2.7 Diagram of photomultiplier tube.....	19
Fig. 2.8 Emission spectra of scintillators and response curve of photocathode	20
Fig. 2.9 Diagram of photodiode.....	20
Fig. 2.10 Spectra response of a silicon photodiode with wavelength.....	22
Fig. 3.1 The furnace system block diagram.....	33
Fig. 3.2 Structural diagram of conventional Bridgman-Stockbarger system.....	34
Fig. 3.3 Structural diagram of moving-temperature-gradient system.....	36
Fig. 3.4 Developed combined moving-temperature-gradient and conventional Bridgman-Stockbarger furnace system.....	37
Fig. 3.5 Prepared ampoule crucible with 22 mm inside diameter	38
Fig. 3.6 Crucible for loading in refractory tube	38
Fig. 3.7 Structure of refractory tube.....	40
Fig. 3.8 Developed glove box in laboratory experiment	42
Fig. 3.9 Scintillation crystal encapsulation components.....	43
Fig. 3.10 Scintillator coupling with PMT for scintillation detector.....	44
Fig. 3.11 Scintillator coupling with PIN photodiode for scintillation detector.....	44
Fig. 3.12 Scintillator coupling with PMT and PIN photodiode for scintillation detector.....	44
Fig. 3.13 Energy resolution test system for scintillator.....	45

List of Figures (Continue)

	Page
Fig. 3.14 Front-end stage configured of PIN photodiode for scintillator assembly.....	46
Fig. 4.1 Temperature response of the furnace during melting period for LaCl ₃ :Ce growth	48
Fig. 4.2 Temperature gradient for LaCl ₃ :Ce crystal growing.....	49
Fig. 4.3 Moving-temperature-gradients along the 8 cm growth zone.....	50
Fig. 4.4 Temperature gradient drift rate along the growth zone.....	51
Fig. 4.5 Temperature profile at the temperature gradient of 25.50°C/hr.....	51
Fig. 4.6 Grown crystal of 10 mm diameter CsI:Tl.....	54
Fig. 4.7 Crystal growth crucible and CsI:Tl of 22 mm diameter and 70 mm length.....	55
Fig. 4.8 Grown crystal of LaCl ₃ :Ce.....	56
Fig. 4.9 Grown crystal of LaCl ₃ :Ce with clear and partially cracked interior.....	56
Fig. 4.10 Grown crystal of Ba ₂ CsI ₅ :Tl	58
Fig. 4.11 Relationship between Tl dopant concentration and energy resolution..	60
Fig. 4.12 Relationship between Tl dopant concentration and relative pulse height.....	60
Fig. 4.13 Comparison of Cs-137 gamma energy spectrum of Ø10 × 10 mm ³ and Ø22 × 22 mm ³ CsI:Tl coupling with PMT.....	61
Fig. 4.14 Comparison of Cs-137 gamma energy spectrum of Ø25 × 25 mm ³ NaI:Tl crystal and Ø22 × 22 mm ³ CsI:Tl coupling with a PMT.....	63
Fig. 4.15 Gamma energy spectrum of Ø10 × 10 mm ³ CsI:Tl coupling with PIN photodiode.....	63
Fig. 4.16 Comparison of photosensitive devices coupling with Ø10 × 10 mm ³ crystal.....	64
Fig. 4.17 Gamma spectrum under different energies for detection efficiencies evaluation.....	65
Fig. 4.18 Gamma energy spectrum of 5 × 5 × 1 mm ³ LaCl ₃ :Ce.....	66

List of Figures (Continue)

	Page
Fig. 4.19 Relation of doped TI concentration with respect to energy resolution...	68
Fig. 4.20 Relation of doped TI concentration with respect to relative pulse height.....	68
Fig. 4.21 Cs-137 gamma energy spectrum of $6 \times 3 \times 1 \text{ mm}^3 \text{ Ba}_2\text{CsI}_5\text{:TI}$	69



ศูนย์วิทยทรัพยากร
 จุฬาลงกรณ์มหาวิทยาลัย

CHAPTER I

INTRODUCTION

1.1 Background on problems of interest

Scintillation detectors have been used in many applications of radiation detection such as gamma-ray detectors, gamma-ray dosimeter, radiation imaging and high energy physics. The scintillator mechanism for gamma-ray detection is the observation of the scintillation light produced when radiation interacts with scintillators to create the electrons and holes before forming exciton pairs after absorption of radiation energy, then the recombination transfers their energy to a luminescent center. The scintillation light is detected by photosensitive devices such as photomultiplier tube (PMT) and photodiode. The photosensitive device converts the scintillation light into an electrical signal as shown in Fig. 1.1. The obtained pulse height of the output signal is proportional to the energy absorbed in a scintillator.

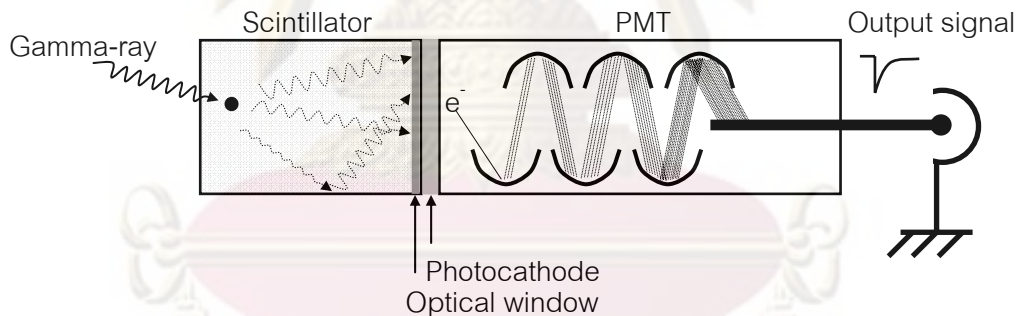


Fig. 1.1 Radiation detection of scintillation detector

Ideally, a scintillator should have high light yield for good energy resolution, fast response time for good time resolution, high density and atomic number Z for efficient gamma ray detection. Obviously, there are many other criteria such as transparency of the material to its own emission, ease of crystal growth, stability in air, and the matching of the scintillation wavelength spectrum with the photosensitive device. However, there is no material that meets all these criteria as the choice of excellent scintillator. For this work, the detection efficiency of a scintillation detector is

improved by modifying inorganic scintillator properties such as energy resolution, light yield and decay time. The lack of a perfect material has resulted in a number of different scintillators being developed and used for different applications.

To achieve the new high-efficiency scintillator we must study the recently new inorganic scintillators for understanding scintillation mechanisms and the growth process. In searching for new and efficient scintillators, most efforts have been directed to cerium-doped crystals. Trivalent cerium emits fast scintillation (15 ~ 60 ns) in the 300-600 nm wavelength region and in many cases the light output is high. Thus, cerium-doped crystals are selected as they have a chance to become high efficiency scintillators. $\text{LaCl}_3:\text{Ce}$, a cerium-doped crystal, is a high efficiency scintillator that gives high light yield, fast decay time and high energy resolution when compare with commercial NaI:Tl . Understanding scintillation mechanisms in $\text{LaCl}_3:\text{Ce}$ helps in searching for new high efficiency scintillators. Finally, the work includes growing new high-efficiency scintillation materials and analyzing scintillation properties compare with commercial NaI:Tl scintillation detector.

1.2 Thesis objective

1. To develop Bridgman-Stockbarger method for growing crystal.
2. To grow high performance inorganic scintillator for gamma-ray spectroscopy.

1.3 Scope of work

1. To design and construct Bridgman-Stockbarger furnace for growing crystal in diameter of 2.5 cm.
2. To grow $\text{LaCl}_3:\text{Ce}^{3+}$ and ternary compound inorganic scintillator such as K_2CeBr_5 or $\text{La}(\text{Br}_x\text{Cl}_{1-x})_3:\text{Ce}^{3+}$.
3. To develop scintillation detector and analyze radiation detection properties by comparing with commercial scintillator.

1.4 Expected benefit

The new high efficiency scintillator can provide more benefits on radiation detection. We can use a new scintillator compatible with applications to result in excellent radiation detection.

Nowadays in Thailand, there aren't many scintillator researches compared with using scintillation detector in various fields. This research can provide more understanding in the mechanism and growth process. Besides, the Bridgman-Stockbarger growing method can be a tool for more scintillator researches in the future.



ศูนย์วิจัยทรัพยากร
จุฬาลงกรณ์มหาวิทยาลัย

CHAPTER II

THEORY AND LITERATURE REVIEW

2.1 Bridgman-Stockbarger crystal growing method

2.1.1 Bridgman technique

The Bridgman technique is the one of most popular bulk crystal growth process. The system consists of four major parts: a dual zone furnace, a driving mechanism, a crucible and a growth pipe. A crucible containing substances is introduced into a gradient furnace which composes of upper and lower furnaces which can generate low and high temperature to create temperature gradient for crystal growing. After loading a charge crucible with specific condition, melting of the loaded substances during the growth process is initiated by moving the crucible or the furnace with specific growth rate for each crystal. A complete grown crystal is cooled down to room temperature before cutting, polishing and investigating. A diagram of the conventional Bridgman-Stockbarger method is shown in Fig. 2.1.

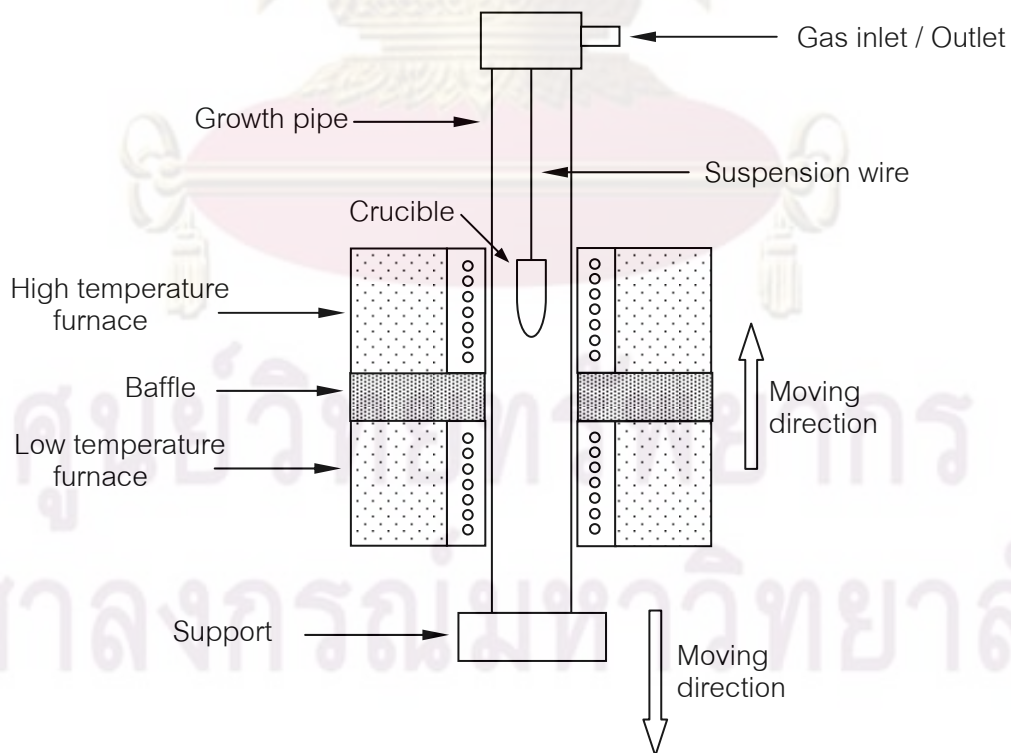


Fig. 2.1 Diagram of conventional Bridgman-Stockbarger method

2.1.2 Crystal growth

The growing of the crystal is referred to as crystallization from solidification process. The solidification process changes substance from liquid to solid phase by nucleation and crystal growth. The first stage is nucleation which is formation of nuclei in heterogeneous nucleation, then formation of crystal with crystal growth to produce single crystal or poly-crystal. The term "solidification" is commonly understood to imply the formation of a crystalline phase from a molten form. The phase transformation is driven by the extraction of heat from the melt, and the progress of the transformation is properly separated into two parts: (1) the initial nucleation of crystals and (2) the growth of these initial nuclei by the accretion of atoms from the melt.

However, the three important aspects to control crystal growths from the melt are: (1) solute manipulation during crystal growth, (2) solid-liquid interface morphologies and (3) defects introduced during crystal growth. These aspects depend on the charge material properties and its phase diagram including the temperature profile of the furnace during growing and cool down processes. Moreover the control of atmosphere, crystal shape and growth rate also influence the final result. Therefore, in crystal growing process, the charge preparation method, growing parameters such as growth rate, temperature gradient in the growth zone and growth pipe atmosphere must be designed.

2.2 Scintillator

In searching of new scintillators [1] for gamma-rays detection, there are basic requirements of scintillator properties: high energy resolution, high light yield (>20,000 photons per absorption), low decay time (10 – 100 ns), high density and atomic number and radiation hardness. However, there are other requirements for good detection efficiency: matching of scintillation wavelength with photosensitive devices, matching of scintillator with refractive index of optical parts, good coupling with photosensitive device, and compatibility of scintillator size with energy. The selection of an appropriate scintillator depends on three categories of radiation measuring system as follows:

a) Integral counting system, the basic counting system for radiation count rate. Energy resolution is not needed from a radiation detector.

b) Differential counting system, the energy spectroscopy system for nuclear spectrum analysis. This system needs energy resolution from a radiation detector.

c) Coincidence counting system, the time spectroscopy system for incidental time spectrum analysis. This system needs fast response time in both rise time and decay time from a radiation detector.

2.2.1 The good properties of material for scintillator

For the differential counting system of gamma spectroscopy, a high energy resolution scintillation detector is required to convert the gamma photon energy into electrical pulse. The ideal scintillation material should possess the following properties: [2]

1. It should convert the kinetic energy of charged particles into detectable light with high scintillation light efficiency.
2. The conversion should be linear and the light yield should be proportional to the deposited energy over as wide range as possible.
3. The medium should be transparent to the wavelength of its own emission for good light collection.
4. The decay time of the induced luminescence should be short so that signal pulse can be generated.
5. The material should be of good optical quality and should be available in size large enough to be of interest as a practical detector.
6. Its index of refraction should be near that of glass (~ 1.5) to permit efficient coupling of the scintillation light to a photoconductive device.

However, no material simultaneously meets all these criteria, and the choice is always a compromise among these and other factors. Inorganic materials tend to have the best light output and linearity, but are very slow in their response time. The high atomic number of constituents and high density of inorganic crystals favor their

choice for gamma-ray spectroscopy, where as enhancement of the probability of visible photon emission during the de-excitation process is modified in the crystal structure.

2.2.2 Scintillator mechanism

Efficient radiation detection for gamma-rays requires understanding of basic interaction mechanisms between the radiation and the scintillator. When gamma-rays interact with a material, there is a probability that energy is absorbed to produce photoelectric effect, Compton scattering and pair production. In the case of photoelectric effect, the total energy of gamma-ray is transferred to the liberated electron. The kinetic energy of the electron is the energy of the incident radiation minus the binding energy of the electron. Compton scattering is the effect where gamma-ray transfers its energy to a weakly bound electron. The energy is distributed to the Compton electron and the scattered photon. The pair production effect only occurs with gamma-ray energies greater than 1.02 MeV. After absorption of gamma-rays, primary electrons lose their energy by collisions with other electrons in the material to generate secondary electrons and holes. These avalanches of secondary particles continue until the energy of the electrons is not sufficient to ionize the material. The excess energy is lost by thermalization. These ionizations consist of mainly electrons and holes. This is a process which is mainly generated in gas and semiconductor based detectors used for detection of low energy gamma-rays and charged particles for creating electrical signals. However, in scintillation mechanism, the process will illuminate scintillation light. A two-stage process that takes place in an ionic crystal, in which electrons trapping center or color centers are present, is ionization or excitation that leads to the formation of exciton. The exciton then de-excites to the ground state and emits scintillation photon from the crystal. The scintillation light is detected by photosensitive devices and converted into an electrical signal.

For higher gamma-ray energy, scintillators are a more compatible choice. A suitable model for inorganic scintillator is the band theory that energy states of atom or molecule consist of a series of discrete energy levels that the higher energy levels, called conduction band, and lower energy levels, called valence band, are separated by a forbidden band. In a normal state, the valence bands are completely

filled with electrons while the conduction bands are empty. The energy difference between conduction band and valence band is the energy gap (E_g) of a few electronvolts (eV). Electrons in the valence band may be raised to the conduction band after absorption of photon energy, leaving positive holes. Photoconduction can then occur due to the free electrons motions in the conduction band and holes in the valence band. In luminescence materials, the excited electron may be trapped at an electron trapping center in the exciton band, and remain bound to the positive hole which constitutes an exciton carrier with no net charge but is free to move through the crystal lattice. The exciton band corresponds to a band of energy below the conduction band. When an electron is promoted into the exciton band, it constitutes excitation. If an electron is promoted into the conduction band, it constitutes ionization. However, electrons in the conduction band may subsequently drop to trapping centers in the exciton band to form excitons. In a similar manner, electrons and positive molecular ions can combine to form excitons. De-excitation from a quick return of electron to the valence band will release energy in a form of photon emission.

This simple model applies only to a perfect crystal lattice. In practice, imperfections due to lattice defects and impurities produce local electronic energy levels in a normally forbidden region between the conduction band and the valence band. If these levels trap electrons or excitons that are moving in the conduction band, they may enter these centers. The luminescence and quenching centers arise from impurities, interstitial ions and/or defects. They introduce local discrete energy levels corresponding to the ground and excited states of the center. The excitation of a center requires capturing of an electron from the conduction band at the "exciton level" and a capture of a hole from the valence band at the "phonon level". Both the capture of exciton and the recombination of electron-hole are simultaneous mechanism. Typical gap widths exhibit too high energy to lie in the visible range. So, most scintillators are added with small amounts of an impurity, called activators, to enhance the probability of a visible photon emission with wavelength matching the PMT. The activators create special sites in the lattice where the normal energy band structure is modified in pure crystal. As a result, there will be an energy state created within the forbidden gap. The electron can de-excite back to the valence band because the energy is less than the full

forbidden band gap. This transition from activator trapping state can shift wavelength in the scintillation process suitable for coupling with photosensitive device as shown in Fig. 2.2.

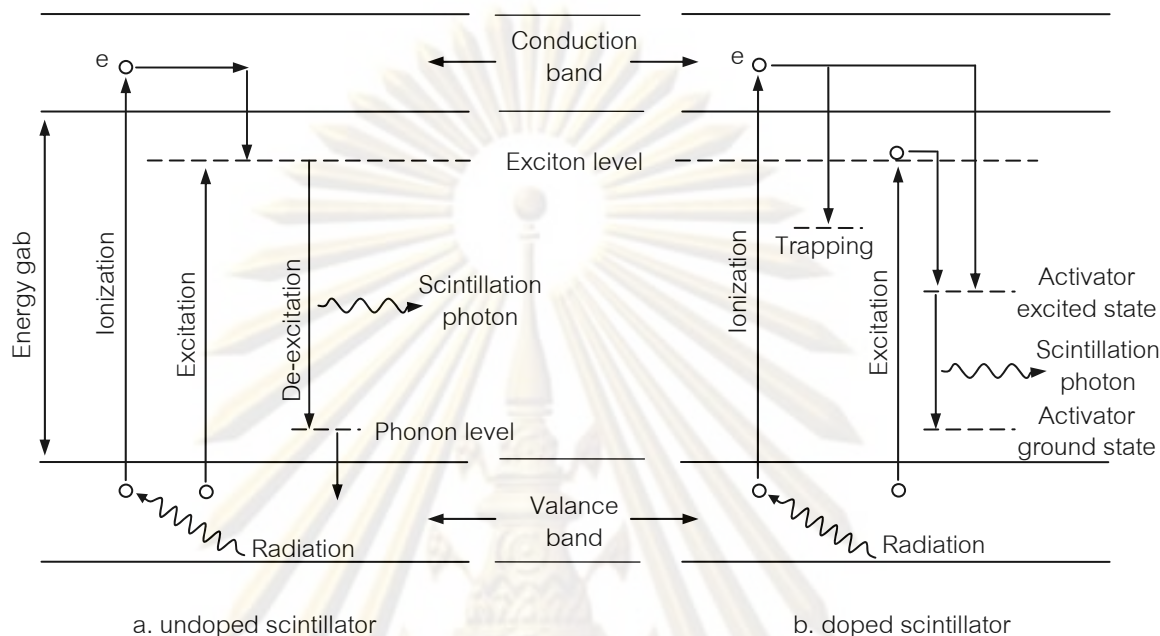


Fig. 2.2 Energy band gap and scintillation mechanism of scintillator [3]

For additional details on mechanisms in inorganic scintillators, we can explain in stages as follows [4].

Stage one: The ionization event creates an inner hole and a primary electron, followed by radiative decay (secondary x-rays), nonradiative decay (Auger process – secondary electrons) and inelastic electron-electron scattering in the time frame of $\sim 10^{-15} - 10^{-13}$ s. Typically, it takes two to seven times the band gap energy of the crystal to create an electron-hole pair. In some crystals the number of pairs created varies with recoil electron energy and this nonlinearity can limit the energy resolution for the detection of gamma-rays by multi-step absorption.

Stage two: When the electron energy becomes less than the ionization threshold, hot electrons and holes are thermalized by intraband transitions and electron-phonon relaxation. The charge carriers can remain as diffuse band states in the case of semiconductors, become trapped by the crystal lattice or form free and impurity-bound excitons, all in a time scale of $\sim 10^{-12} - 10^{-11}$ s. During these stages luminescent centers

may be excited by impact excitation by hot electrons, sequential electron-hole capture or sequential hole-electron capture and sensitizer-activator energy transfer processes over a time scale ranging from $<10^{-12}$ to $>10^{-8}$ s. Depending on the carrier mobility, this time is responsible for the intrinsic rise time of the scintillation light.

Stage three: The excited luminescent species return to the ground state by nonradiative quenching processes or by emitting a photon. The radiative process can be as short as 10^{-9} s for electron-hole recombination, free and bound exciton emission and core-valence recombination, or it can take several minutes for the case of highly forbidden processes. There are many different luminescent species and scintillation mechanisms possible in inorganic materials. The luminescence may be intrinsic to the material and involve electron-hole recombination, constituent transition group or post transition group ion fluorescence, core-valence band transitions or charge transfer transitions within a molecular complex. Or it may be extrinsic such as luminescence associated with impurities or defects and additive dopant ions. As the role of an activator, the dopant ion may be the luminescence species or may promote luminescence as in the case of defect bound exciton emission.

2.2.3 Types of Scintillation Process

There are many types of luminescence for scintillator, but the important scintillation processes are shown as follows [4].

a) **Free and impurity-bound exciton:** Ionization electrons and holes can combine to form free excitons with electron-hole binding energies of a few to ~ 0.06 eV. At low temperatures these are usually bound as an entity to an impurity atom or defect with a binding energy of several MeV. Radiative decay of free or bound excitons can be very fast (<1 ns), however at ambient temperatures the emission is weak because most excitons become unbound or disassociated.

b) **Self-trapped exciton:** In this case the ionization hole localizes on one or more atoms with associated lattice relaxation. The resulting Coulomb defect traps a spatially diffuse electron to create a self-trapped exciton. The unpaired spin associated with the hole and the diffuse electron spin form a triplet state which has a radiative lifetime of typically 10^{-6} s because the transition is spin forbidden. The singlet state

decay can be much faster (10^{-9} s), but is weaker. Examples of self-trapped excitons occur in NaI (pure), CsI (pure) and BaF_2 . In the case of the halides, the self-trapped hole is commonly a V_k center consisting of a bound pair of halogen ions.

c) Self-activated scintillator: In these materials, the luminescent species is a constituent of the crystal. Emission involves intraionic transitions in the cases of Bi^{3+} in $\text{Bi}_4\text{Ge}_3\text{O}_{12}$ and Ce^{3+} in CeF_3 or charge transfer transitions in the case of $(\text{WO}_4)^{2-}$ in CaWO_4 and CdWO_4 . In $\text{Bi}_4\text{Ge}_3\text{O}_{12}$ the ionization process results in a hole in the 6s level of Bi^{3+} and an excited electron in the 6p level. Since the hole is on a cation, these are also called cation excitons. The radiative $3P_{0,1} \rightarrow 1S_0$ transitions are spin forbidden and slow at cryogenic temperatures. At room temperature both the decay time and the luminosity are reduced by competing nonradiative transitions.

d) Activator ions: For dopant ions such as Tl^+ , Ce^{3+} and Eu^{2+} the ionization holes and electrons are sequentially trapped on the same luminescent ion. In several materials [e.g., CsI:Tl and $\text{LaCl}_3\text{:Ce}$] the luminosities can be very high, near the theoretical limit. For Ce^{3+} the electric-dipole $5d \rightarrow 4f$ transition is allowed, but is relatively slow (typically 20-40 ns) due to the poor spatial overlap between the 5d and 4f orbital. The Eu^{2+} $5d \rightarrow 4f$ and Tl^+ $3P_{0,1} \rightarrow 1S_0$ decays are slower (about 1 μs) because the transitions are only partially spin allowed. The rise time of the activator luminescence may be slow if one of the carriers has limited mobility as, for example, the slow hole migration in CsI:Tl and NaI:Tl.

e) Core-valence luminescence: In these materials (examples are BaF_2 , CsF, RbF, KMgF_3 , BaLu_2F_8) the energy gap between the valence band and the top core band is less than the fundamental band gap. A photon is emitted when an electron in the valence band fills an ionization hole in the top core band. This is an allowed process and the decay time is on the order of 1 ns, however the luminosity is limited to about 2,000 ph/MeV due to the inefficiency of creating holes in an upper core band.

2.2.4 Inorganic scintillators doped with cerium

The last stage in the scintillation process is the transfer of energy to the luminescent center which will emit a photon with a certain probability. In inorganic scintillators doped with cerium, the Ce^{3+} ion acts as luminescent centre. This trivalent lanthanide ion has one electron in the 4f ground state configuration. The 4f electron is shielded from the crystal field [5] by 5p and 5s electron shells. Excitation of Ce^{3+} promotes the 4f electron to a higher 5d orbital. Subsequent de-excitation will occur by a 5d - 4f electric dipole allowed transition with a decay time of about $\tau = 15 - 60$ ns. Since the energy difference between the lowest energy of the Ce^{3+} 5d configuration and the highest energy of the Ce^{3+} 4f configuration is large, multiphonon-relaxation from the 5d to the 4f ground state is unlikely to occur. However, when the lowest multiplet of the Ce^{3+} 5d configuration is admixed with conduction band wave functions, excitation of the 4f electron to a higher 5d orbital may result in auto-ionisation of Ce^{3+} and the excitation energy is lost; the electron immediately de-localises in the conduction band and may eventually be trapped at another impurity or at a dislocation in the perfect lattice. For this reason $\text{La}_2\text{O}_3:\text{Ce}$, $\text{Lu}_2\text{O}_3:\text{Ce}$ and $\text{LaAlO}_3:\text{Ce}$ do not show Ce^{3+} luminescence. Therefore, knowledge of the positions of the Ce^{3+} 5d levels inside the band gap is of great importance to the understanding of the scintillation mechanisms and the probability of energy transfer to Ce^{3+} and its luminescence.

2.2.5 Scintillation Crystal Evaluation

In scintillation crystal evaluation, the growth crystal is cut and polished then the dopant concentration in the crystal is analyzed by XRF and the bulk crystal structure is analyzed by XRD. Optical and radiation detection properties are analyzed by the methods as described below:

2.2.5.1 Thermoluminescence

Thermoluminescence is measured with samples mounted on the cold finger. The samples, cooled down to 14 K with liquid He, are irradiated with X-ray generated pulses and then heated up to 340K at a rate of 10 K/min. The luminescence is detected by a PMT. Isothermal decays are measured in a similar manner with the

difference that the sample is heated up to a selected temperature which the emission is measured versus time.

2.2.5.2 Emission spectrum

In measuring the emission spectra of scintillator crystals, the crystals are excited with radiation from the X-ray tube at energy about 80 kV, 4mA . The scintillation light is entered through a monochromator in a spectrophotometer and detected with a PMT with a quartz window. The system is calibrated with a standard light source to enable correction for sensitivity variations as a function of wavelength.

2.2.5.3 Energy resolution

For determination of the energy resolution, the scintillator is coupled with a PMT and is irradiated with a Cs-137 source at energy 662 keV. The gamma-ray spectrum is analyzed by a gamma-ray spectrometer with MCA (Multichannel analyzer). The energy resolution of the 662 keV photopeak from gamma-ray spectrum can be calculated from a FWHM (Full width at half maximum) at room temperature related to photopeak energy.

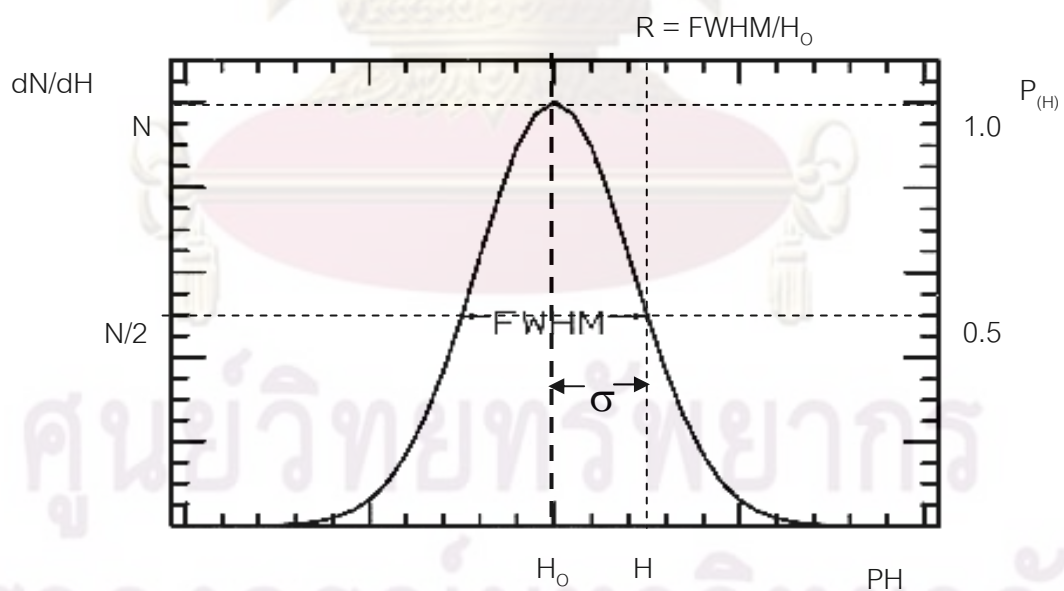


Fig. 2.3 Definition of detector resolution in Gaussian shape peak

The formal definition of detector energy resolution [2] is illustrated in Fig. 2.3. The differential pulse height distribution for a hypothetical detector assumes that a single energy is being recorded. The full width at half maximum (FWHM) is defined as the width of the distribution at the level that is just half of the maximum ordinate of the peak. The energy resolution of the detector is conventionally defined as the FWHM divided by the location of the peak centroid H_0 as shown in Eq. (2.1)

$$\text{Energy resolution (R)} = \frac{\text{FWHM}_{\text{PH}}}{H_0} = \frac{\text{FWHM}_E}{E_0} \quad (2.1)$$

Where FWHM_{PH} and H_0 are the full width at half maximum and the peak centroid of pulse height, respectively. In the case that if the energy scale is calibrated, FWHM_E and E_0 is the full width at half maximum and the peak centroid of energy, respectively.

There are a number of potential sources of fluctuation in the response of a given detector which result in imperfect energy resolution. The statistical explanation arises from the fact that the number of charge carrier n generated within the detector by radiation includes noise. An estimate can be made of the amount of inherent fluctuation by assuming that the formation of each charge carrier follows a Poisson process. The average charge expected in the standard deviation will be \sqrt{n} . If this were only source of fluctuation in the pulse height signal, the response function should exhibit a Gaussian shape as shown in Fig. 2.3. In this case, the probability Gaussian function in Eq. (2.2) is introduced for a resolution prediction.

$$P_{(H)} = \frac{1}{\sigma\sqrt{2\pi}} \exp - \frac{(H - H_0)^2}{2\sigma^2} \quad (2.2)$$

From Eq. (2.2), $P_{(H)}$ at H_0 is equal to $1/\sigma\sqrt{2\pi}$. Thus, the width of σ at $P_{(H)} = 0.5$ can be expressed as

$$0.5 = \frac{1}{\sigma\sqrt{2\pi}} \exp - \frac{(H - H_0)^2}{2\sigma^2}$$

$$H - H_0 = 1.1774\sigma$$

$$\text{FWHM} = 2(H - H_0) = 2.35\sigma$$

We then can calculate a limiting resolution R due only to statistical fluctuations in the number of charge carrier n corresponding to the amplitude H_0 as

$$R_p = \frac{\text{FWHM}}{H_0} = \frac{2.35\sqrt{n}}{n} = \frac{2.35}{\sqrt{n}} \quad (2.3)$$

This limiting value of R depends only on the number of charge carrier n , and the resolution improves as n is increased. In scintillation detector, the charge carriers are number of electrons collected from the photocathode of the photomultiplier tube which is generated by the scintillation light. An improvement of the energy resolution can be achieved by increasing the light yield of the scintillator.

2.2.5.4 Pulse height measurement

Pulse height measurements are generally performed to obtain information on the light yield of the scintillation material under ionizing radiation [5]. Gamma-rays emanating from a radioactive source excite the crystal. In most cases a Cs-137 source is used. The scintillation light is detected by a PMT and generates analog signal output proportion to a light yield. The analog signal is converted to a digital pulse by a conventional ADC unit. The signal can be stored and processed by a computerized data handling system.

Scintillation light yields expressed in photoelectrons per MeV (ph/MeV) of absorbed gamma-ray energy can be calculated by comparing the peak position of the photopeak to that of the single electron spectrum [6]. In order to transform the number of photoelectrons per MeV into an absolute light yield expressed as the number of photons per MeV (ph/MeV) of absorbed gamma-ray energy, the overall detection efficiency of the PMT has to be known. The detection efficiency $\eta(\lambda)$ is given by:

$$\eta_D(\lambda) = \eta_Q(\lambda)\eta_C\eta_L \quad (2.4)$$

where $\eta_Q(\lambda)$ is the quantum efficiency of the PMT, η_C is the charge collection efficiency of the photoelectrons emanating from the photocathode and

η_L is the light collection efficiency which represents the fraction of the light emitted by the crystal reaching the photocathode.

The quantum efficiency $\eta_Q(\lambda)$ of the PMT is provided by the manufacturer of the tube. The charge collection efficiency η_C and the light collection efficiency η_L can be estimated. The number of photons per MeV of absorbed gamma-ray energy N_{ph} is calculated by multiplying the number of photoelectrons per MeV of absorbed gamma-ray by the average quantum efficiency of the PMT.

$$N_{ph} = N_{Phe} \frac{\int I_{Xray}(\lambda) \eta_D(\lambda) d\lambda}{\int I_{Xray}(\lambda) d\lambda} \quad (2.5)$$

where $I_{Xray}(\lambda)$ is the intensity distribution of the gamma-ray excited emission spectrum of the crystal.

2.2.5.5 Detection efficiency

Usually, the detection efficiency depends primarily on the radiation energy, the crystal size and is tabulated value in intrinsic efficiency ϵ_{int} [2]. In terms of a hypothetical differential pulse height distribution shown in Fig. 2.4, the entire area under the spectrum is a measure of the number of all pulses that are recorded but the full energy event appears only photo-peak area and the other are Compton escape area. Therefore, the peak efficiency can be determined that only those interactions that deposit the full energy of the incident radiation are counted. The total and peak efficiencies are related by the peak to total ratio [2]. However, the peak to total ratio is difficult to determine exactly [7] and hence a related figure which is directly dependent on it is measured. This is the ratio of the full energy peak height to the Compton height measured below the Compton edge called "peak to Compton ratio, P/C".

The detector efficiency should be specified according to both of peak and total efficiency. Therefore, the most common type of efficiency tabulated for gamma-ray detector is the "intrinsic peak efficiency" which related to the full energy peak counts (N), the number of radiation quanta (S) and the solid angle subtended by the detector at the source position (Ω), as in Eq. (2.6).

$$\epsilon_{int} = 4\pi N / \Omega S \quad (2.6)$$

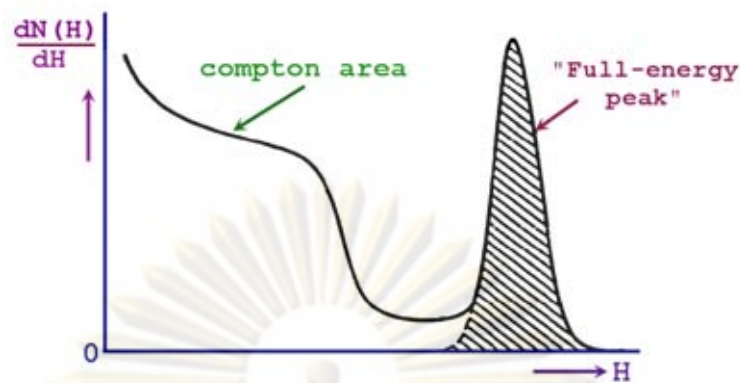


Fig. 2.4 The full energy peak in a differential pulse height spectrum

2.2.5.6 Scintillation decay time

In the method called the *conventional method* [5], the sample under study is mounted on the start PMT and is excited by gamma-rays from a Cs-137 source. If a gamma-ray is absorbed in the crystal, the generated scintillation pulse is detected by the start PMT and converted into start timing pulse. The stops are derived from the detection of single photons detected by the stop PMT. They are converted into stop timing pulses. The time between start and stop timing pulses is then digitized. After recording a large number of scintillation events, the number of single photons detected per scintillation event in a time interval t , $t + dt$ (where dt is the TDC time resolution) is plotted as a function of t . As such, the time distribution equals the shape of the scintillation pulse as shown in Fig. 2.5.

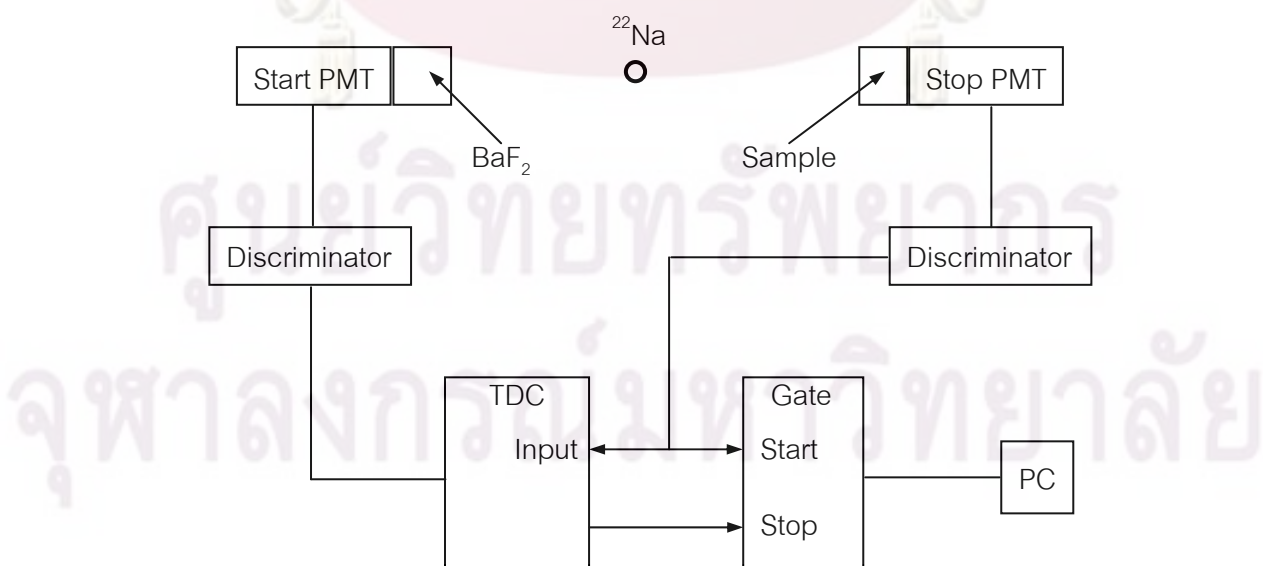
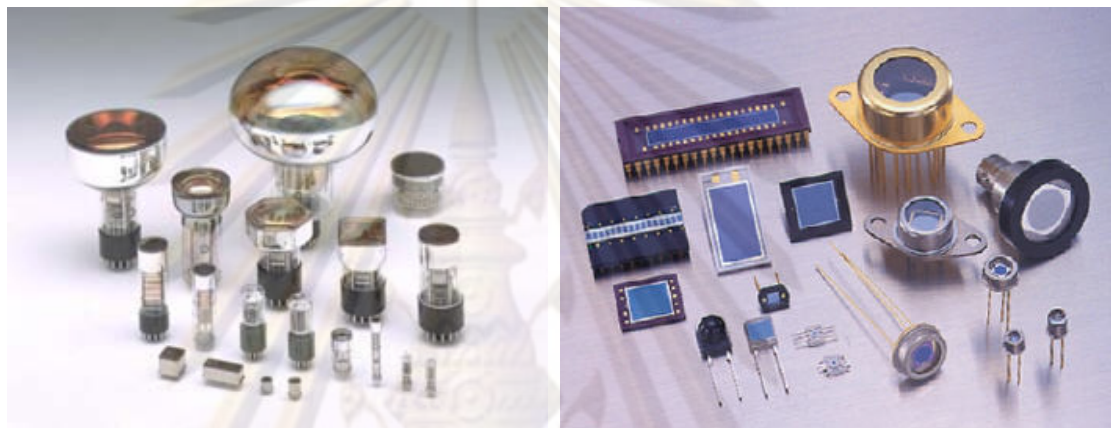


Fig. 2.5 Conventional method for determination of scintillation decay time

2.3 Photosensitive device

A scintillation detector detects radiation by interaction with radiation and creation of scintillation light which can be detected with photosensitive devices. Generally, a photomultiplier tube is most popular to coupling with a scintillator to form scintillation detectors. In recent years, as photonic technology has become rapidly developed, a photodiode is also an important photosensitive device for scintillation detector. Both types of photosensitive devices are illustrated in Fig. 2.6.



a) Photomultiplier tube

b) PIN Photodiode

Fig. 2.6 Photosensitive devices for scintillator

2.3.1 Photomultiplier tube

Photomultiplier tubes (PMT) are extremely sensitive detectors of light in the ultraviolet, visible and near-infrared ranges of the electromagnetic spectrum. These detectors multiply the electron produced by the incident light by as much as 100 million times in multiple dynode stages as shown in Fig 2.7. The combination of high gain, low noise, high frequency response, and large collection area features of photomultipliers are essential functions in nuclear and particle physics, astronomy, medical diagnostics including blood tests, medical imaging, motion picture film scanning, and high-end image scanners.

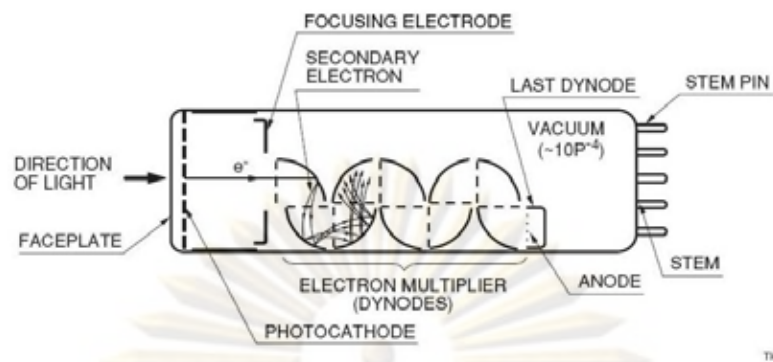


Fig. 2.7 Diagram of Photomultiplier tube [8]

In the early 1940s the JEDEC (Joint Electron Devices Engineering Council), an industry committee on standardization, developed a system of designating spectral responses [9]. The philosophy included the idea that the product's user need only be concerned with the response of the device rather than how the device may be fabricated. Various combinations of photocathode and window materials were assigned "S-numbers" (spectral numbers) ranging from S-1 through S-40, which are still in use today. For example, S-11 uses the cesium-antimony photocathode with a lime glass window, S-13 uses the same photocathode with a fused silica window, and S-25 uses a so-called "multialkali" photocathode that provides extended response in the red portion of the visible light spectrum. Fig 2.8 illustrates emission spectra of several common inorganic scintillators with the response curves of S-11 and bialkali photocathodes. No suitable photoemissive surfaces have yet been reported to detect wavelengths longer than approximately 1700 nanometers, which can be approached by a special (InP/InGaAs(Cs)) photocathode.

ศูนย์วิทยทรัพยากร

จุฬาลงกรณ์มหาวิทยาลัย

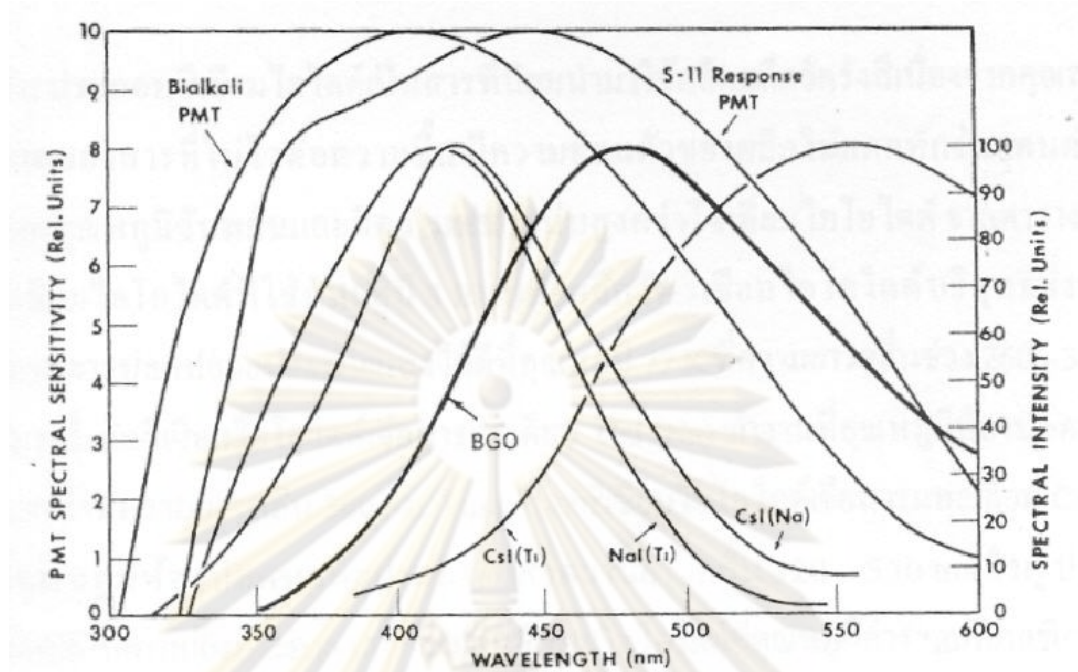


Fig. 2.8 Emission spectra of scintillators and response curve of photocathode [2]

2.3.2 Photodiode

A photodiode is a type of photodetector capable of converting light into either current or voltage, depending upon the mode of operation. Photodiodes are similar to regular semiconductor diodes except that they may be either exposed packaged with a window or optical fiber connection to allow light to reach the sensitive part of the device. Many diodes designed for use specifically as a photodiode will also use a PIN junction rather than the typical PN junction as shown in Fig. 2.9.

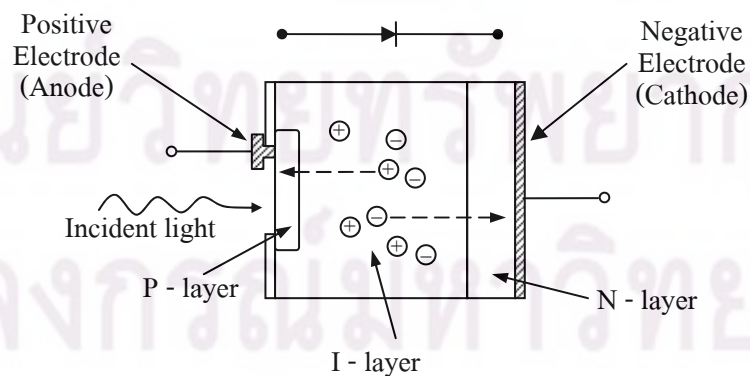


Fig. 2.9 Diagram of photodiode

A photodiode is a PN junction. When a photon of sufficient energy strikes the diode, it excites an electron, thereby creating a mobile electron and a positively charged electron hole. If the absorption occurs in the junction's depletion region or one diffusion length away from it, these carriers are swept from the junction by the built-in field of the depletion region. Thus, holes move toward the anode, and electrons move toward the cathode and a photocurrent is produced. When used in a zero bias or a photovoltaic mode, the flow of photocurrent out of the device is restricted and a voltage builds up. The diode becomes forward biased and dark current begins to flow across the junction in the direction opposite to the photocurrent. This mode is responsible for the photovoltaic effect. In the photoconductive mode, a reverse bias dramatically reduces the response time at the expense of the increased noise. This increases the width of the depletion layer, which decreases the junction's capacitance resulting in faster response times. The reverse bias induces only a small amount of current (known as saturation or dark current) along its direction while the photocurrent remains virtually the same. The photocurrent is linearly proportional to the light illumination. Although this mode provides faster response, it tends to exhibit more electronic noise. The leakage current of a good PIN diode is so low ($< 1\text{ nA}$) that the Johnson–Nyquist noise of the load resistance in a typical circuit often dominates.

The material used to make a photodiode is critical to defining its properties, because only photons with sufficient energy to excite electrons across the material's band gap will produce significant photocurrents.

Table 2.1 Materials commonly used to produce photodiodes [10]

Material	Wavelength range (nm)
Silicon	190–1100
Germanium	400–1700
Indium gallium arsenide	800–2600
Lead(II) sulfide	$<1000\text{--}3500$

Because of their greater band gap, silicon-based photodiodes generate less noise than germanium-based photodiodes, but germanium photodiodes must be used for wavelengths longer than approximately $1\ \mu\text{m}$. Fig. 2.10 shows spectra response for wavelength of a silicon photodiode.

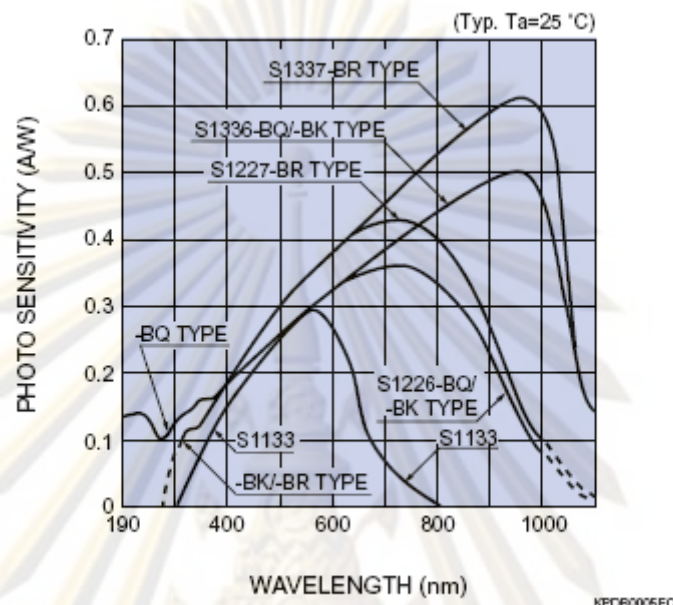


Fig. 2.10 Spectra response of a silicon photodiode with wavelength [11]

Properties of photodiode depend on critical performance parameters including responsivity, dark current and noise equivalent power.

a) **The responsivity** is the ratio of generated photocurrent to incident light power, typically expressed in A/W when used in photoconductive mode. The responsivity (sensitivity at response spectrum) may also be expressed as quantum efficiency or the ratio of the number of photo-generated carriers to incident photons.

b) **The dark current** is the current through the photodiode in the absence of light when it is operated in photoconductive mode. The dark current includes photocurrent generated by background radiation and the saturation current of the semiconductor junction. Dark current must be accounted for by calibration if a photodiode is used to make an accurate optical power measurement, and it is also a source of noise when a photodiode is used in radiation measurement as it affects energy resolution.

c) **Noise-equivalent power** is the minimum input optical power to generate photocurrent equal to the rms noise current in a 1 hertz bandwidth. The noise-equivalent power is roughly the minimum detectable input power of a photodiode.

2.4 Literature review

Literature review has been conducted on researches in the past in designing Bridgman-Stockbarger method, commercial and high efficiency crystal growing, high efficiency scintillator performances and scintillation detector evaluation method.

2.4.1 Modified Bridgman-Stockbarger method

In recent years, there were many researches aimed to improve the traditional vertical Bridgman technique for growing high-quality crystals. L.C. Wang, Y.C. Liu, W.C. Yu, B. Roux, T.P. Lyubimova and C.W. Lan [12] investigated the controlled dopant segregation by accelerated crucible rotation for the vertical Bridgman growth of Ga-doped germanium crystals. The accelerated crucible rotation technique (ACRT) and the angular rotation technique (AVT) were considered. Both techniques were found effective in radial segregation control; however, ACRT generated more global mixing and thus slightly larger axial segregation. E. Saucedo, P. Rudolph and E. Dieguez [13] aimed to improve structural perfection and reduce Te particle concentration in CdTe crystals. A modified Bridgman method with artificial seeding has been developed. It allows the adjustment of different degrees in superheating of the melt before the growth process is started. A turning furnace was designed and employed. Crystals with 20 mm diameter and 100 mm length were grown using different superheating temperatures and then structurally, optically and electrically characterized. A moderate improvement of the structural quality is obtained, when the CdTe melt is superheated 110 K above the melting point (1365 K) for 24 hours before the crystal growth process. An effective reduction of the Te particle concentration has been observed in the as-grown crystals. The results are correlated to the highly associated melt structure that dissociates after superheating of 110 K by the formation of mono-dimensional species. The technical growth modification could be an interesting

alternative to produce CdTe crystals with improved quality for detector devices. Kevin T. Zawilski, M. Claudia C. Custodio, Robert C. DeMattei and Robert S. Feigelson [14] studied the ability of vibroconvective stirring to control the growth interface shape during vertical Bridgman growth. It was demonstrated using the coupled vibrational stirring (CVS) technique. CVS involves the application of low-frequency vibrations to the outside of the growth ampoule and produces strong flows emanating from the fluid surface. Previous studies showed that the growth rate and interface shape fluctuations occurred under growth with a constant vibrational frequency. In order to eliminate these fluctuations, the paper examines methods to apply the lower vibrational frequency as growth progressed to maintain a constant fluid flow rate in the vicinity of the growth interface. These flow control methods were tested on two growth systems of NaNO_3 and lead-magnesium niobate–leadtitanate (PMNT). The previously observed fluctuations were greatly reduced when flows were appropriately controlled. Using this control method, CVS flows were then applied to reduce the concavity of the growth interface in the NaNO_3 system at fast growth rates of more than 10 mm/h. K.A. Kokh, B.G. Nenashev, A.E. Kokh and G.Yu. Shvedenkov [15] reported the use of heat field rotation as a contact-free influence upon the heat-mass transfer processes in vertical Bridgman–Stockbarger crystal growth. The modified heating furnace which allows the creation of a rotating heat field with various amplitude–frequency characteristics is described. A high-quality, conical, single crystal of AgGaS_2 of 30 mm diameter and 80 mm length was grown using this heat field rotation method (HFRM). Jiayue Xu, Shiji Fan and Baoliang Lu [16] used multi-crucible Bridgman furnace for industrial growth of 4" diameter $\text{Li}_2\text{B}_4\text{O}_7$ single crystals and 3 – 6 crystals can be grown in the furnace at the same time. The growth conditions were optimized and growth defects, such as twins, bubbles and striations, were investigated. Using $\text{Ø}82$ mm LBO crystal as seed, bubble free, twin-free and striation-free LBO crystals 105 mm in diameter and 80 – 120 mm in length were reproducibly grown along $\langle 110 \rangle$ direction. Commercial availability of $\text{Ø}4$ " $\text{Li}_2\text{B}_4\text{O}_7$ crystal crucibles has been realized in laboratory and it indicated the validity of the furnace for mass-production of 4" $\text{Li}_2\text{B}_4\text{O}_7$ crystals. Therefore, the special technique of non-moving crucible and furnace during the growth process such as Electro-Dynamic Gradient (EDG) was studied by Csaba Szeles, Scott E. Cameron, Jean-Olivier Ndap and

William C. Chalmers [17]. The growth of large-volume semi-insulating CdZnTe single crystals with improved structural perfection has been demonstrated by the electrodynamic gradient (EDG) technique and active control of the Cd partial pressure in the ampoule. The EDG furnace nearly completely eliminates the uncontrolled radiative heat transport commonly encountered in traditional Bridgman systems where the charge and furnace move relative to each other. Since the new furnace utilizes electronically controlled high-precision gradient translation, it achieves superior thermal stability throughout the growth. The control of the Cd partial pressure allowed the solidification and cool-down of the ingots close to the stoichiometric composition. As a result, the formation and incorporation of large-size ($>1 \mu\text{m}$ diameter) Te inclusions was avoided during crystallization and ingots with high structural perfection were achieved. Adequate electrical compensation has been achieved in most of the crystal growth experiments yielding CdZnTe crystals with bulk electrical resistivity in the 10^9 - $10^{10} \Omega\cdot\text{cm}$ range and electron mobility-lifetime product as high as $\mu\tau = 1.2 \times 10^{-3} \text{ cm}^2/\text{V}$. The materials exhibit good spectral performance in the parallel plate detector configuration.

2.4.2 Rare earth halide preparation

Guohao Ren, Xiaofeng Chen, Yu Pei, Huanying Li and Hongxiang Xu [18] grew LaCl_3 crystals from hydrated LaCl_3 . Five endothermic peaks at 100.4, 156.0, 181.0, 210.6 and 840 °C were observed in the DTA curves with thermal dehydration. The process of dehydration is described to be 7 \rightarrow 6 \rightarrow 3 \rightarrow 1 \rightarrow 0 in the dehydration process but little amount of LaOCl phase could be identified from oxidation of LaCl_3 at high temperature. In addition, LaOCl phases also appear in the grown crystals which were suggested to be responsible for the transmission loss of the crystals. The oxidation temperature of LaCl_3 with oxygen is much lower than that with water. Hongbing Chen, Peizhi Yang, Changyong Zhou and Chengyong Jiang [19] grew $\text{LaCl}_3:\text{Ce}$ by dehydration procedure of $\text{LaCl}_3\cdot 7\text{H}_2\text{O}$ and $\text{CeCl}_3\cdot 7\text{H}_2\text{O}$ which were prepared by heating $\text{LaCl}_3\cdot 7\text{H}_2\text{O}$ and $\text{CeCl}_3\cdot 7\text{H}_2\text{O}$ at 200 – 230 °C for 6–7 hours in dried HCl atmosphere. A 4 mol% Ce^{3+} doped LaCl_3 crystal with a size of $\text{Ø}28 \times 70 \text{ mm}^3$ was grown under growth rate of 0.5 – 0.8 mm/h and a temperature gradient of around 30 °C/cm across solid–liquid interface. G. Meyer and P. Ax [20] studied the ammonium

chloride route to anhydrous rare-earth metal by reaction of rare earth oxide with HCl and NH_4Cl . They found that there is a two-step procedure consisting of the (dry or wet) synthesis of a complex chloride in the form of $(\text{NH}_4)_3\text{RECl}_6$ at temperature of 220 °C and decomposition either directly for small-size rare earth or via the intermediates of $(\text{NH}_4)_2\text{RECl}_5$ and $\text{NH}_4\text{RE}_2\text{Cl}_7$ for large and medium size rare earth, respectively. G. Meyer, S. Dötsch and T. Staffel [21] converted NH_4Br from rare earth oxides or hydrated rare earth bromides. The two-step procedures start with the synthesis of a ternary bromide and then the decomposition of the ternary bromide to the binary tribromide in vacuum at 350 – 400 °C. The actual decomposition pathways are dependent upon the size of the trivalent cation and may pass through the intermediate $\text{NH}_4\text{M}_2\text{Br}_7$.

2.4.3 Commercial and high performance scintillator

CsI:TI scintillation crystal is non-hygroscopic and has no cleave plane properties, thus, it is useful in many applications such as gamma dosimeter, radiation imaging and high energy physics. Han Soo Kim, Jang Ho Ha, Se Hwan Park, Seung Yeon Cho and Yong Kyun Kim [22] fabricated CsI:TI/PIN diode radiation sensors for application in various fields such as an NDT and an environmental radiation monitoring system. CsI:TI crystals of $11 \times 11 \times 21 \text{ mm}^3$ were processed as an optical grade from a CsI:TI ingot and matched with PIN diodes based on light loss and external impact. The photodiode signal is amplified by a low-noise preamplifier and a pulse shape amplifier. At room temperature, the fabricated CsI:TI/PIN diode radiation sensors demonstrate an energy resolution of 7.9% for 660 keV gamma-rays and 4.9% for 1330 keV gamma. The fluctuation of the directional dependency was below 14% from 0 to 90 degrees for the incident 660 keV gamma-rays. The compactness, the low-voltage power supply and the physical hardness are very useful features for industrial applications of the fabricated CsI:TI/PIN diode sensor. N. Balamurugan, A. Arulchakkaravarthi, S. Selvakumar, M. Lenin, Rakesh Kumar, S. Muralithar, K. Sivaji and P. Ramasamy [23] grew single crystals of pure and thallium doped cesium iodide by Bridgman technique. The grown crystals underwent powder x-ray diffraction and high-resolution XRD analysis. The cut and polished crystals were characterized for luminescence studies. UV-visible

transmission studies have been carried out on the grown crystal in the wavelength range of 200 – 650 nm. From the transmission spectrum, it was found that the cut off wavelength increases with the increase in Tl concentration and that the transmittance is about 70%. The 0.06 mol% of Tl doped CsI crystal shows a good energy resolution of 7.6%. The hardness decreases with increasing doping concentration. Etching studies have been carried out on doped and undoped crystals using methanol and water as etchant. Guohao Ren, Xiaofeng Chen, Sheng Lu, Zhongbo Li, Xuanping Xue and Dingzhong Shen [24] grew CsI crystals doped with different concentrations of Tl. The dependency of the light output on Tl content was studied and 1000 ppm (mol) of Tl was suggested as a suitable doping level for growing large CsI:Tl crystals with this crystal growth technique. The distribution of thallium along the longitudinal direction of the CsI crystal has been proved to be inhomogeneous. The non-uniformity of light output along the longitudinal axis of a large crystal with dimension of $80 \times 80 \times 400 \text{ mm}^3$ was rather evident, however, it could be amended, during the mechanical processing of the crucible, by properly defining one of the end faces (tail side) as the particle incident face, named as front face, and another end face (seed side) for attachment with PMT or photodiode to be named as rear face. The influence of irradiation on the non-uniformity of light output was investigated as well.

The cerium doped crystals were grown in many researches in the past few years. O. Guillot-Noël, J.T.M. de Haas, P. Dorenbos, C.W.E. van Eijk, K. Krämer and H.U. Güdel [25] studied the optical and scintillation properties of $\text{LaCl}_3: 0.57\% \text{ Ce}$, $\text{LuBr}_3: 0.021\%$, 0.46% , $0.76\% \text{ Ce}$ and $\text{LuCl}_3: 0.45\% \text{ Ce}$ under optical, x- and gamma-ray excitation. The highest light yield of 40000 ± 4000 photons per MeV of absorbed gamma-ray energy was measured for $\text{LaCl}_3: 0.57\% \text{ Ce}$. An energy resolution of, respectively, $7.0 \pm 0.5\%$, $6.0 \pm 0.1\%$, $7.8 \pm 0.3\%$, $6.5 \pm 0.5\%$ and $18.0 \pm 0.5\%$ was observed for the 662 keV full absorption peak. The scintillation decay curves can be described with three components: 20 ± 2 , $330 \pm 30 \text{ ns}$ and $2.2 \pm 0.2 \mu\text{s}$ for $\text{LaCl}_3: 0.57\%$; 32 ± 3 , $450\text{-}550 \text{ ns}$ and $>5 \mu\text{s}$ for $\text{LuBr}_3: 0.76\%$; 50 ± 5 , $250\text{-}350 \text{ ns}$ and $>4 \mu\text{s}$ for $\text{LuCl}_3: 0.45\%$. J. Andriessen, O.T. Antonyak, P. Dorenbos, P.A. Rodnyi, G.B. Stryganyuk, C.W.E. van Eijk and A.S. Voloshinovskii [26] studied the spectroscopic properties of Ce^{3+} in LaCl_3 single crystals at a temperature of 8 K by means of (vacuum) ultra violet excitation between

4 and 20 eV. $\text{LaCl}_3:\text{Ce}$ shows an exceptionally small crystal field splitting of the Ce 5d levels and the Stokes shift between absorption and emission is large. Theoretical calculations were performed using a combination of the Hartree–Fock ionic cluster model and the density functional band structure model. Very good agreement with experiment was obtained. In the excited 5d configuration the Ce ion appears to move off-centre by lattice relaxation and the crystal field splitting almost doubles, resulting in the large Stokes shift. A comparison with the properties of the concentrated system CeCl_3 is made. It seems that in this crystal a slight off-centre position already occurs in the ground state 4f configuration. E. V. D. van Loef, P. Dorenbos, C. W. E. van Eijk, K. Krämer and H. U. Güdel [27] studied the scintillation properties of LaCl_3 doped with different Ce^{3+} concentrations. Ce^{3+} emission is observed peaking at 330 and 352 nm. For LaCl_3 doped with 2%, 4%, 10%, and 30% Ce^{3+} and pure CeCl_3 , a light yield of 46000 ± 3000 photons per MeV of absorbed energy were measured. The scintillation decay curve can be described by three decay components: short ($\tau = 25$ ns), intermediate ($\tau = 200\text{--}800$ ns) and long ($\tau = 0.8\text{--}14$ μs). The contribution of the short decay component to the total light yield increases with Ce^{3+} concentration: ranging from 10% for $\text{LaCl}_3:2\% \text{Ce}^{3+}$ to 69% for pure CeCl_3 . An energy resolution for the 662 keV full energy peak of $3.5 \pm 0.4\%$, $3.5 \pm 0.4\%$, $3.1 \pm 0.3\%$, $3.3 \pm 0.3\%$ and $3.4 \pm 0.3\%$, respectively, was observed for $\text{LaCl}_3: 2\%, 4\%, 10\%, 30\% \text{Ce}^{3+}$ and pure CeCl_3 . C.P. Alliera, E.V.D. van Loef, P. Dorenbos, R.W. Hollander, C.W.E. van Eijk, K. Krämer and H. U. Güdel [28] obtained a high resolution gamma-ray detector consisting of an 8 mm diameter and 5 mm thick $\text{LaCl}_3:\text{Ce}$ scintillation crystal coupled to a 16 mm diameter APD from Advanced Photonix Inc. The energy resolution at 662 keV is about 3.7%. The low intrinsic resolution of about 2%, the high light yield of the crystal of 46000 ± 5000 photons per MeV and the high quantum efficiency of the avalanche photodiode make this gamma-ray detector an excellent choice for applications where high energy resolution is required. J. Glodo, K.S. Shah, M. Klugerman, P. Wong and B. Higgins [29] characterized $\text{LaCl}_3:\text{Ce}$ and $\text{LaBr}_3:\text{Ce}$ scintillators by a high light yield and a very fast nanosecond primary emission. To study scintillation mechanisms in these materials, they have measured low-temperature thermoluminescence. Both crystals exhibited prominent glow peaks below 100 K. $\text{LaCl}_3:10\%\text{Ce}$ sample showed multiple glow peaks

with two major ones at 65 and 66 K, whereas the $\text{LaBr}_3:0.5\%\text{Ce}$ sample showed two major peaks at 65 and 75 K. Assuming first-order kinetics, the traps responsible for those peaks can be described by the following parameters: $E=0.168$ eV, $s=1\times 10^{12}$ s⁻¹; $E=0.135$ eV, $s=1\times 10^9$ s⁻¹ for $\text{LaCl}_3:\text{Ce}$ and $E=0.144$ eV, $s=1\times 10^{10}$ s⁻¹; $E=0.166$ eV, $s=1\times 10^{10}$ s⁻¹ for $\text{LaBr}_3:\text{Ce}$. The lifetimes of listed traps at room temperature are in the range of radiative lifetime of Ce^{3+} emission (0.5 – 50 ns).

In recent days, there are many types of ternary compounds that have been researched. E.D. Bourret-Courchesne, G. Bizarri, S.M. Hanrahan, G. Gundiah, Z. Yan and S.E. Derenzo [30] reported the scintillation properties of $\text{BaBr}_2:\text{Eu}^{2+}$. A light yield of $81,000\pm 3000$ ph/MeV of absorbed gamma-ray energy was measured. An energy resolution of $4.8\pm 0.5\%$ was observed for the 662 keV full absorption peak. Pulsed x-ray luminescence measurements show two exponential decay components of 297 and 482 ns with a contribution to the total light output of 23% and 77%, respectively. Under x-ray and UV excitation, the emission corresponds to a broad band center at 413 nm. These initial values make $\text{BaBr}_2:\text{Eu}^{2+}$ one of the brightest and the fastest known Eu^{2+} -doped scintillators. E.D. Bourret-Courchesne, G. Bizarri, R. Borade, Z. Yan, S.M. Hanrahan, G. Gundiah, A. Chaudhry, A. Canning and S.E. Derenzo [31] reported the excellent scintillation properties of $\text{Ba}_2\text{CsI}_5:\text{Eu}^{2+}$. An estimated light yield of $97,000\pm 5,000$ ph/MeV of absorbed gamma-ray energy was measured. An energy resolution of $3.8\pm 0.3\%$ was observed for the 662 keV full absorption peak. Pulsed x-ray luminescence measurements show a relatively complex time response with four exponential decay components of 48, 383, 1500 and 9900 ns with a contribution to the total light output of 1%, 26%, 68% and 25%, respectively. Under x-ray and UV excitation, the emission corresponds to a broad band centered at 2.85 eV. First principles calculations show strong localization of the excited state on the Eu site. $\text{Ba}_2\text{CsI}_5:\text{Eu}^{2+}$ has a density of about 5 g/cm³. These first reported scintillation properties make $\text{Ba}_2\text{CsI}_5:\text{Eu}^{2+}$ a very high-performance scintillator.

2.4.3 Scintillator performance testing method

There are many types of scintillator performances that can be evaluated. However, choosing a scintillator for radiation detection much depends on application. In common, three types of performances are usually tested: energy resolution, light yield and decay time. The methods for testing light yield are reported by I. Holl, E. Lorenz and G. Mageras [32]. They measured the light yield in photons/MeV of some common inorganic scintillating crystals with silicon photodiodes. Incident particles are gammas in the 1 MeV region. The light signal was calibrated against 60 keV gammas converted directly in the photodiode depletion layer. Among the tested materials, CsI:TI gave the highest light yield of 52,000 photons/MeV deposited energy. M. Moszyński, M. Kapusta, M. Mayhugh, D. Wolski and S.O. Flyckt [33] measured the absolute light outputs of BGO, CsI:TI and some new Ce-doped crystals to an accuracy of about 55% using calibrated XP2020Q photomultipliers and standard S3590-03 and S2740-03 photodiodes. The use of small crystals, 9 mm in diameter and 1 mm thick, reduces the corrections for imperfections in the light collection process and in the photoelectron collection by the photomultipliers. The measured light output of the BGO crystals was 8500 ± 350 ph/MeV. The carried out study highlighted the importance of the spread in the published emission spectra of the crystals which seems to limit measurement accuracy. Finally, a simple comparative method of measuring the light output to an accuracy of $\pm 10\%$ is proposed using an uncalibrated XP2020 photomultiplier and a 1 mm thick BGO crystal as a standard. Johan T. M. de Haas and Pieter Dorenbos [34] determined the absolute scintillation yield of recently developed $\text{LaBr}_3:\text{Ce}$, $\text{LaCl}_3:\text{Ce}$, and $(\text{Lu},\text{Y})_2\text{SiO}_5:\text{Ce}$ scintillators and traditional $\text{Lu}_2\text{SiO}_5:\text{Ce}$, $\text{Bi}_4\text{Ge}_3\text{O}_{12}$, NaI:TI , CsI:TI , and CsI:Na scintillators by means of a photomultiplier tube, a Si-photodiode, and a Si-avalanche photodiode. These are all well-known scintillators that cover emission wavelengths from 250 nm to 750 nm. By comparing the scintillation yield independently measured with the three different photon detectors, reliable yield values are obtained. E. Sysoeva, V. Tarasov and O. Zelenskaya [35] presented methods for determination of the physical light yield, based on measurements of pulse amplitude, single-electron pulses and intrinsic photomultiplier resolution are discussed. These methods have been used for the

measurements of light yield of alkali halide crystals and oxide scintillators. Repeatability and reproducibility of results were determined. All these methods are rather complicated in use, not for measurements, but for further data processing. Besides that, they demand a precise determination of photo-receiver's parameters as well as determination of the light collection coefficient of the scintillation detector. Therefore, such methods should be used only for special cases of certification of reference detectors. For routine measurements of scintillation light yields, a simple method based on comparison of signals from tested and certificated detectors was developed.



ศูนย์วิทยทรัพยากร
จุฬาลงกรณ์มหาวิทยาลัย

CHAPTER III

DESIGN AND DEVELOPMENT

In this research and development of a high performance inorganic scintillator for gamma-ray spectroscopy, the special furnace was designed and constructed for supporting the designed crystal growing method in both conventional and modified Bridgman-Stockbarger techniques. The glove box was utilized to prepare hygroscopic materials. Growth crystals were cut, polished and coupled with a PMT and a PIN photodiode for radiation detection performance testing, comparing to a commercial NaI:Tl crystal performance.

3.1 Equipment design and construction

In previous works [36], small size CsI:Tl scintillators of 10 mm diameter were successfully grown by a dual zone vertical furnace using conventional Bridgman-Stockbarger technique with a maximum temperature of 1000 °C and adjustable temperature gradient at the growing zone in the range of 10.00 to 50.00 °C/cm. In this research we intend to develop 25 mm diameter commercial, high resolution and ternary compound scintillation crystals of CsI:Tl, LaCl₃:Ce and Ba₂CsI₅:Tl, respectively. For the ternary compound crystal of Ba₂CsI₅:Tl, high resolution and high density performances are expected. The simple and economical equipment for crystal growing process is considered. Both conventional and modified Bridgman-Stockbarger crystal growing techniques are studied and compared. The criteria for furnace design are the highest melting point of 860 °C of LaCl₃ and the required crystal size of 25 mm in diameter with 6 cm in length.

3.1.1 Crystal growing furnace

The furnace system was designed to have two dual zone vertical furnaces. Each furnace has an operating temperature range of 400 to 1200 °C, electrical power consumption of 4 kW and physical dimensions of 45 × 45 × 39 cm³. A firebrick insulator and a 1 mm wire size Kanthal AF heating wire were employed to construct a heat shield tube furnace element with 15.2 cm length and 6 cm inside diameter, giving

a maximum temperature of 1300 °C. The growth zone of 7.6 cm in length and 5 cm in diameter is sandwiched in aligned axis position of upper and lower tube furnace elements. The differential temperature characteristics are independently controlled in the middle of the heating zones by two thermocouples installed on the tube wall of high and low temperature furnace elements, in conjunction with two temperature PID controller. Its thermal stability is enhanced by closing both ends of the furnace tube. The measured data from thermocouples during the growth process is acquired by a PIC microcontroller via an RS485 port and recorded to the built-in EEPROM as data logger. This recorded temperature distributions can be transferred to a personal computer via an RS232 port after the end of the growth process. The block diagram of the furnace system is shown in Fig. 3.1.

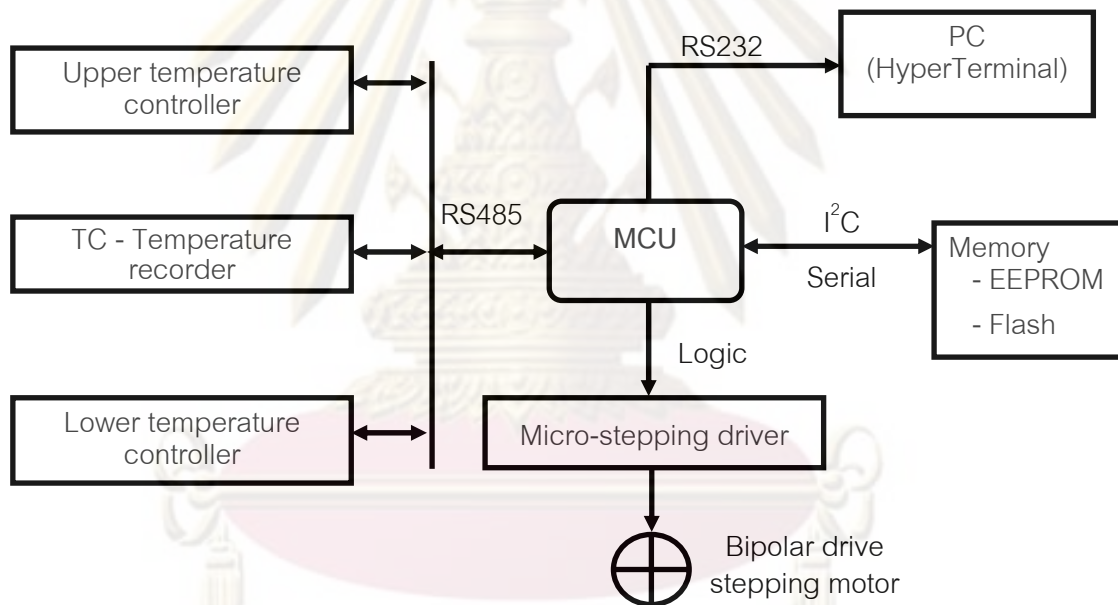


Fig. 3.1 The furnace system block diagram

The structure and technical features of both developed furnace systems for crystal growing are described as follows:

a) Conventional Bridgman-Stockbarger furnace

The crystal growth rate at the growth zone of the developed conventional Bridgman-Stockbarger furnace was controlled by the translation rate of the charge crucible relative to fixed furnaces using a top driving mechanism. The thermocouple

was installed at the crucible joint for temperature profile recording. The crucible and thermocouple were translated by direct driving of a stepping motor with a controlled translation rate of between 0.1 to 5 mm/h. The structural diagram and the developed conventional Bridgman-Stockbarger furnace system were shown in Fig. 3.2 and the right hand side of Fig. 3.4, respectively.

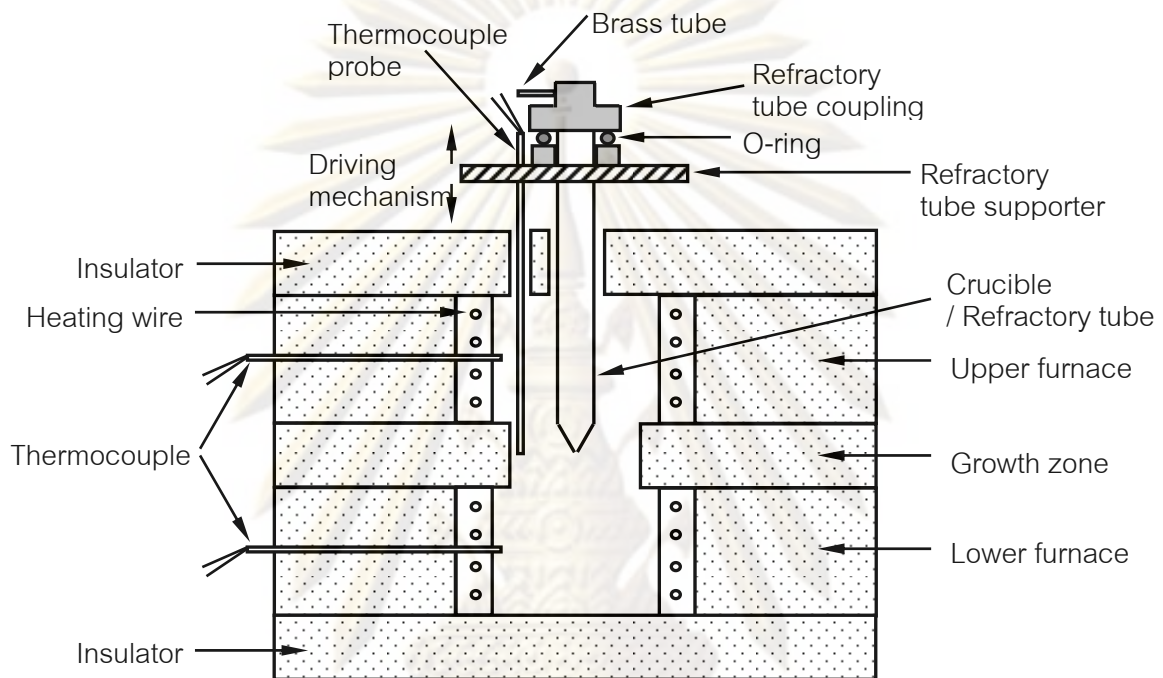


Fig. 3.2 Structural diagram of conventional Bridgman-Stockbarger furnace system

The bipolar drive stepping motor with micro-stepping control method by Intelligent Motion Systems, Inc model IM834 (Appendix A) was employed for driving the top loading vertical translation of linear screw drive mechanism and interfaced with a PIC microcontroller for motor speed control as mentioned in the diagram of Fig. 3.1. The translation rate can be controlled by varying the controlled clock speed, generated from a PIC microcontroller function, in the range of 4 – 70 Hz. This clock speed range represents the growth rate in the range of 0.3 to 5.0 mm/hr. Two high-precision temperature controllers were employed for controlling different temperature settings of upper and lower furnace elements.

b) Moving-temperature-gradient furnace

The moving-temperature-gradient principle is applied to modify the vertical Bridgman crystal growth process. The temperature gradient drift rate of the growth zone in the middle of high and low temperature furnaces were controlled by independently controlling each heating zone. Two high-precision temperature controllers with programmable ramp function are employed for controlling the temperature of furnaces. The same temperature reduction rate of both furnaces is arranged for generating a moving-temperature-gradient with a constant temperature gradient drift rate along the growth zone. The temperature probe driving mechanism part, isolated from the furnace system, is also designed and attached for recording temperature data of the growth zone. The moving-temperature-gradient furnace was applied for non-moving crucible and furnace during the growth process.

A moving-temperature-gradient is generated with a constant temperature gradient drift rate along the growth zone. Its thermal stability is enhanced by closing both ends of the furnace tube. The temperature heat up rate in the range of 0.1 to 500 °C/hr and the temperature gradient drift in the range of 5 to 50 °C/cm can be set. A driving mechanism of the thermocouple probe for temperature distribution measurement along the growth zone is installed at the bottom of the furnace. The structure diagram and the developed furnace are illustrated in Fig. 3.3 and the left hand side Fig. 3.4, respectively.

The differential temperature reduction rate is set to ensure perfect crystallization. Crystal growth rate of the moving-temperature-gradient method depends on the ratio of the temperature gradient drift rate and the temperature gradient as follows:

$$\text{Growth rate (cm/hr)} = \frac{\text{Temperature gradient drift rate (°C/hr)}}{\text{Temperature gradient (°C/cm)}} \quad (3.1)$$

From Eq. (3.1), the same growth rate can be obtained from various combinations of temperature gradient drift rates and temperature gradients. For example, the growth rate of 1 mm/hr could be a combination of (1 °C/hr and 10 °C/cm), (2 °C/hr and 20 °C/cm), (3 °C/hr and 30 °C/cm) and so on. Each combination can be

optimized by a temperature heat up rate setting in the programmable function of the upper and lower temperature controller.

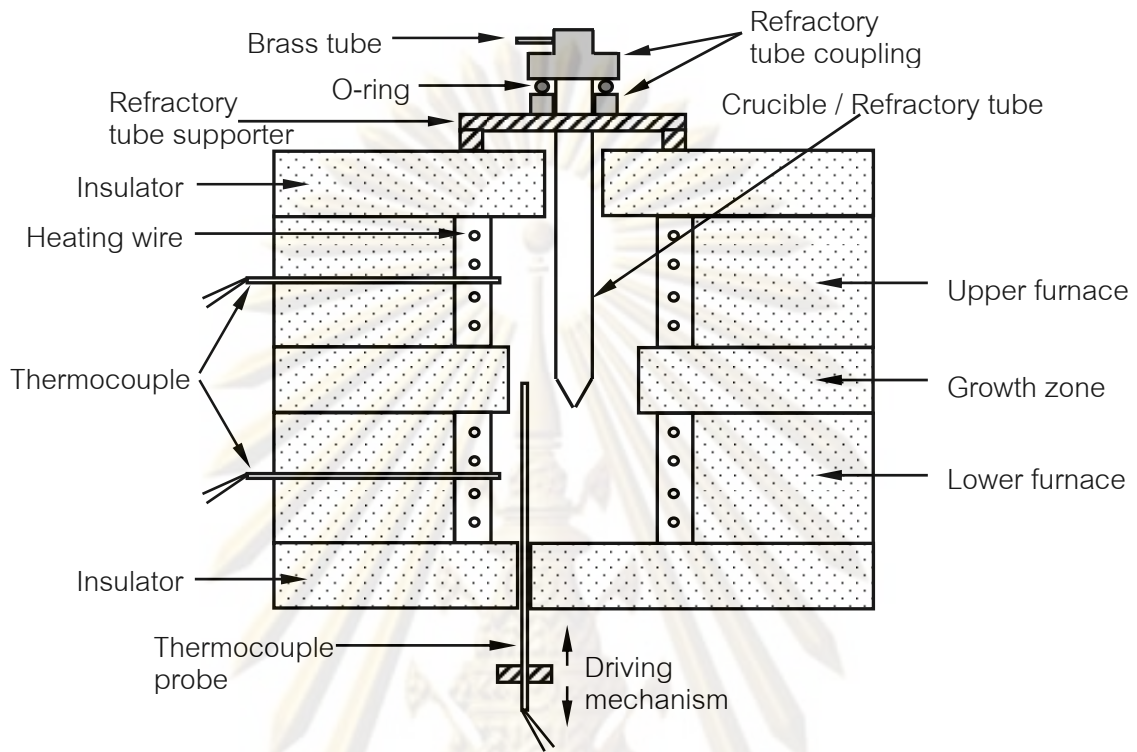


Fig. 3.3 Structural diagram of moving-temperature-gradient system

Generally, the temperature profile of the melt-mixing crystal growing process in the growth zone of the Bridgman method can be divided into 3 periods as charge melting, solidification and crystal cool down. Each configuration of the temperature profile depends on the type of compound elements to be grown. During the melting period, the temperature response depends on the heating rate of the furnace, while the profile at the solidification depends on the temperature gradient setting. The cool down period could be natural or step down temperature for preventing thermal stress in the growth crystal.

In the conventional Bridgman-Stockbarger furnace, the crystal growth rate could be controlled by setting different temperatures of upper and lower furnace elements and by setting the translation rate of the movable charge crucible. For the moving-temperature-gradient system applied to Bridgman-Stockbarger, the crystal growth rate could be controlled by setting the ramp-up and ramp-down temperature

function. The moving-temperature-gradient system was designed in order to eliminate a driving mechanism and in order to reduce subtle vibration which could adversely affect crystal quality; the charge crucible and the furnace are made stationary during the growth process.

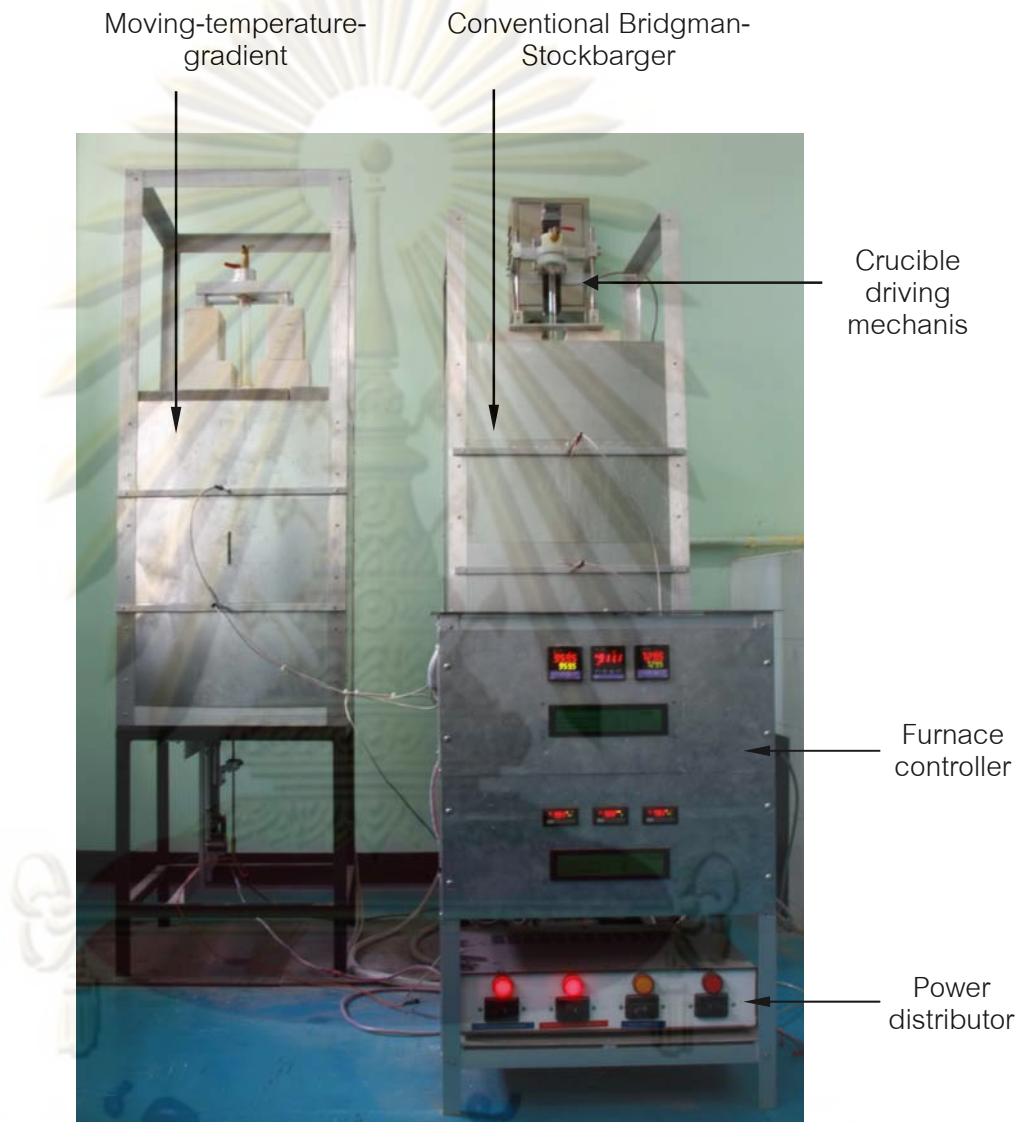


Fig. 3.4 Developed combined moving-temperature-gradient and conventional Bridgman-Stockbarger furnace system

3.1.2 Charge crucible

The highest melting point of all grown crystals is 860 °C from LaCl_3 , so a material used as a charge crucible must withstand a higher melting point. Quartz is a suitable material of choice. This research planned to grow crystals with three different

sizes which fit the quartz inside diameter of 10, 14 and 22 mm and length of between 40 and 60 mm. The crucible with a bottom conical shape was chosen and designed with two configurations as a sealed ampoule and an open-ended crucible in a pressurized gas condition. During crystal growing process the crucible will be supported in a refractory tube.

The ampoule crucible was fabricated from a long quartz tube with bottom conical shape and constricted at the sealed part as shown in Fig. 3.5. An aluminum flange with an evacuation outlet port was epoxy-sealed at the open end for vacuum pump evacuation. Sealing process will be done at the constricted part after charge loading and evacuated by melting and pulled with high temperature blowing frame. This type of crucible is suitable for hygroscopic charge elements.



Fig. 3.5 Prepared ampoule crucible with 22 mm inside diameter

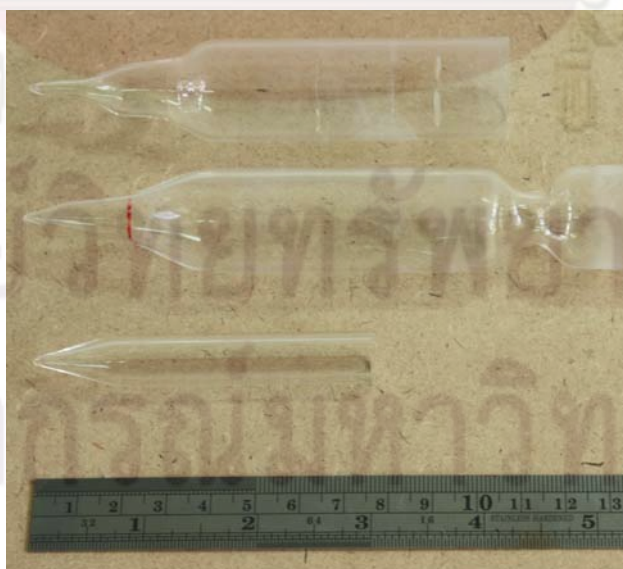


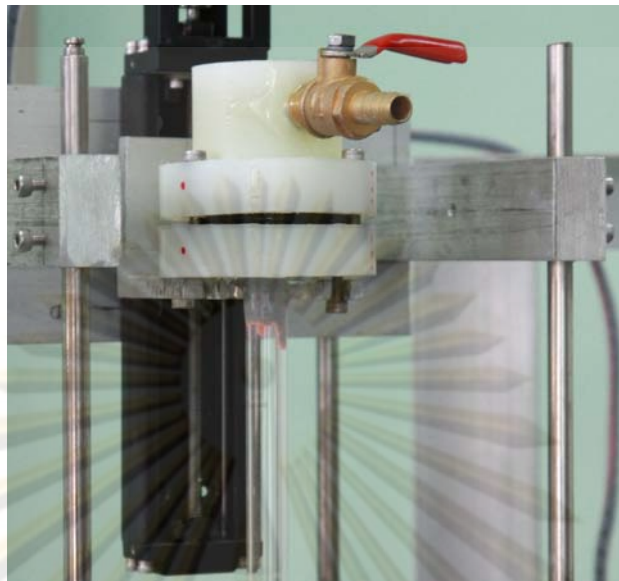
Fig. 3.6 Crucible for loading in refractory tube

The open-ended crucible was also fabricated from a quartz tube with the bottom end designed in various curves of conical shapes. The crucible is easy to make and is convenient for charge preparation. It can also be reused after special cleaning process. The fabricated open-ended crucibles in different sizes are compared with the ampoule crucible as shown in Fig. 3.6. This type of crucible is suitable for non-hygroscopic charge elements.

3.1.3 Refractory tube

A refractory tube is a jacket tube filled with Al_2O_3 for supporting the charge crucible in isolation from vibration and holding the crucible in the growth zone of the furnace. The quartz refractory tubes of 14, 22 and 25 mm inside diameter and 450 mm length were designed for loaded crucibles of 10, 14 and 22 mm inside diameter, respectively. The refractory tube is specially designed to permit easy crucible loading and reusing after cleaning. The top end of the refractory tube is mounted with an epoxy sealed aluminum flange or superlene while the other end is closed. A brass gas fitting connector of 5 mm inner diameter with a 2-way valve is fixed on the aluminum or superlene flange cover for vacuum pump evacuation outlet and argon gas pressurization inlet. Both aluminum flanges are coupled together with a vital O-ring to prevent air leakage. The refractory tube with the superlene coupling port is shown in Fig. 3.7a. and the refractory tube with the aluminum coupling port is shown in Fig. 3.7b.

In the modified Bridgman-Stockbarger crystal growing method using the moving-temperature-gradient technique, vibration is eliminated. Therefore, the refractory tube could be used directly as the growth tube crucible. With this benefit, the multi-crucible technique is applied to increase crystal production yield at each growth cycle. The multi-crucible growth tube was designed to support three crucibles of 14 mm inside diameter as shown in Fig. 3.7b. This crucible will be useful for studying at least three growth crystal samples with different dopant concentrations under the same condition of crystal growing parameter at the growth zone.



a) Refractory tube with superlene coupling port



b) Multi – crucible (Refractory) tube with aluminum coupling port

Fig. 3.7 Structure of refractory tube

ศูนย์วิทยทรัพยากร
จุฬาลงกรณ์มหาวิทยาลัย

3.1.4 Glove box

A glove box is an important equipment for crystal growing process with hygroscopic materials during the preparation process of loading charge materials into a crucible. A glove box not only prevents oxygen and moisture that can chemically react with charge materials during the preparation step, but also prevents moisture absorption into the growth crystal during the assembly step.

The glove box was designed and constructed in a laboratory using 1.5 cm thick acrylic in two sections with dimensions of $40 \times 70 \times 40 \text{ cm}^3$. Two latex gloves were used to manipulate inside the glove box during both crucible charge loading and loaded crucible transfer. The in-box Thermometer/Hygrometer gauge uses a SHT115 IC chip from Sensirion as a temperature and moisture sensor interfaced to a battery-operated PIC microcontroller. The function program was developed to calculate relative humidity and temperature for displaying on an LCD panel. The moisture detection could be down to 0% relative humidity with $\pm 2\%$ error at 10 to 90% relative humidity range and $\pm 4\%$ maximum error at less than 10% and more than 90% relative humidity.

Moisture in the developed glove box was reduced by three operation steps. Firstly, air in the glove box was pumped out by a diaphragm pump and argon gas was filled. Moisture could be reduced from generally 60 - 70% relative humidity down to 27 - 35% relative humidity. Secondly, moisture could be further reduced by silica gel absorber down to 13 - 15% relative humidity. Finally, moisture in the glove box was kept at a steady-state level of 4 - 7% relative humidity by SrCl_2 (strontium chloride) absorption prepared from heating of $\text{SrCl}_2 \cdot 6\text{H}_2\text{O}$ (Hexahydrate strontium chloride) at $320 \text{ }^\circ\text{C}$ [37].

In preparation of the charge loading process, CaSO_4 (Calcium sulfate) was also used to trap residue moisture from argon gas circulation in the glove box. During the process, the closed-loop argon gas with the diaphragm pump was circulated through CaSO_4 in a desiccant unit. By applying CaSO_4 as a desiccant, the moisture could be reduced more than 1% relative humidity. Moisture reduction is most important for prevention of chemical form transformation of hygroscopic materials, which seriously

affects single crystal formation during the solidification period. The developed glove box and its components are shown in Fig. 3.8

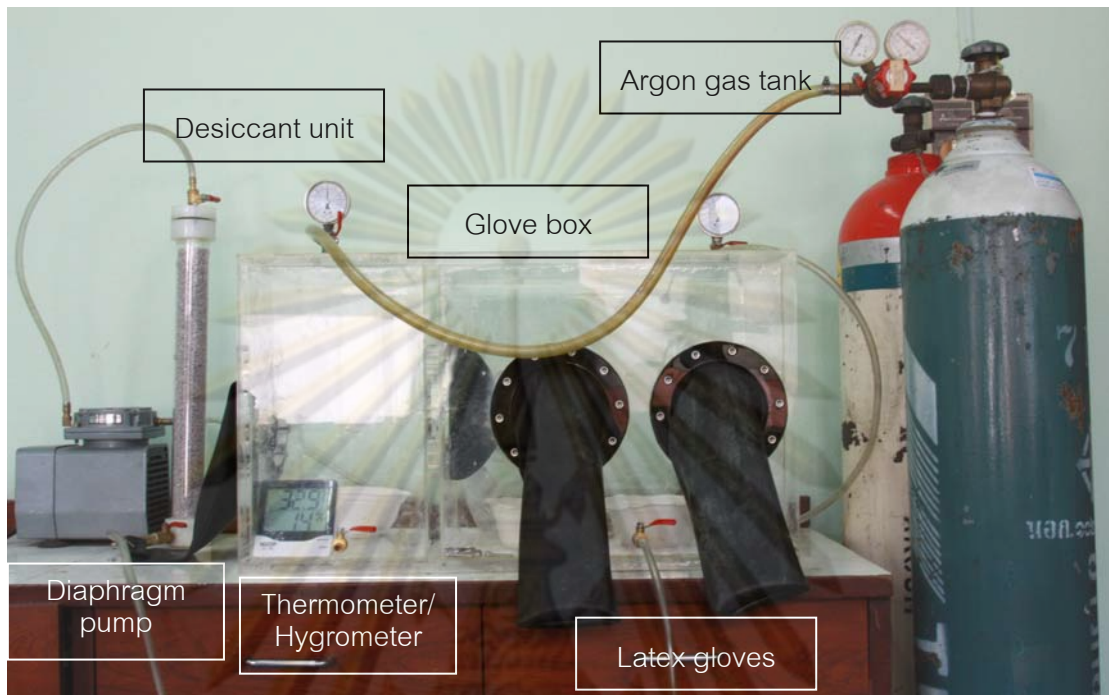


Fig. 3.8 Developed glove box in laboratory experiment

3.2 Scintillation crystal assembly

In this research, the growth crystals performance for gamma ray spectroscopy was examined. The crystal transparent to the wavelength of its own emission was tested by transmission meter from EDTM model SD2400. Mono-energetic gamma-ray at 662 keV energy of Cs-137 was used for energy resolution evaluation. The scintillation crystal must be encapsulated and coupled with a photosensitive device to form a scintillation detector. Both PMT and PIN photodiode were used as a photosensitive device to compare conversion efficiency in illumination light to electrical pulse height signal. Various energy spectra responses for many combinations of photosensitive devices and crystal types are discussed.

3.2.1 Scintillation Crystal Encapsulation

Encapsulation of a scintillation crystal is necessary for hygroscopic crystal to prevent absorption of moisture from the environment which can reduce

detection efficiency and also to prevent light interfering on a coupled photosensitive device. Normally, the crystal will be encapsulated in a thin aluminum cylinder housing with a closed-end plate of the same type of the housing material in one side, and the other side closed with a good optical transmitter of scintillation wavelength for coupling with a photosensitive device. Inside of the housing wall will be lined with a reflector. A reflector is an important material that can reflect scintillation photon back through a clear crystal to a photocathode of a photosensitive device for photon signal enhancement. There are many commercial types of reflector material such as MgO powder, white Teflon tape and BaSO₄ in polyvinyl alcohol [38]. For this research, we used a white Teflon tape as a reflector, borosilicate glass as a light guide and an aluminum tube with a closed-end plate as a crystal housing as shown in Fig. 3.9. The encapsulated scintillation crystal is called a scintillator.



Fig. 3.9 Scintillation crystal encapsulation components

3.2.2 Scintillator coupling

In the energy resolution testing, the scintillator was coupled to a suitable photosensitive device. The growth crystals in this research emitted the scintillation photon in different wavelengths, e.g., CsI:TI at 540 nm and LaCl₃:Ce at 330 and 352 nm [27]. Therefore, the photocathode response of each photosensitive device was determined. Two Ø2" Photomultiplier tubes (PMT) from RCA model 5819 and Hamamatsu model 52154-02 (Appendix B.1) were chosen for testing the energy

resolution of the scintillators in comparison with a PIN photodiode from Hamamatsu model S3590-8 (Appendix B.2) with an active area of 100 mm^2 . The scintillator was coupled on a photocathode of the photosensitive device using an optical fluid coupling for refractive index matching. The configuration of the scintillator coupling for coupling with the PMT and the PIN photodiode are shown in Fig. 3.10 and Fig. 3.11, respectively.

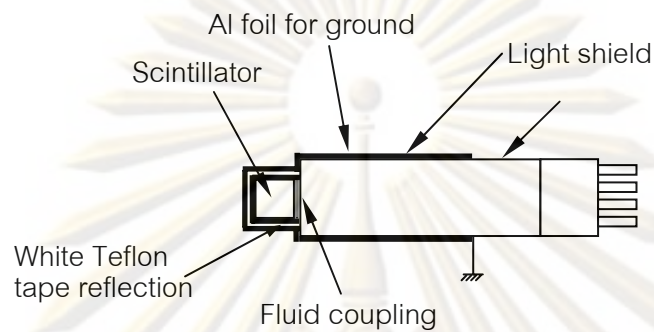


Fig. 3.10 Scintillator coupling with PMT for scintillation detector

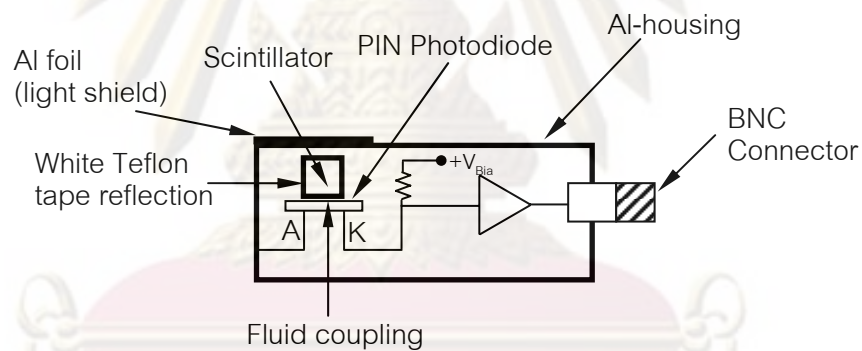


Fig. 3.11 Scintillator coupling with PIN photodiode for scintillation detector

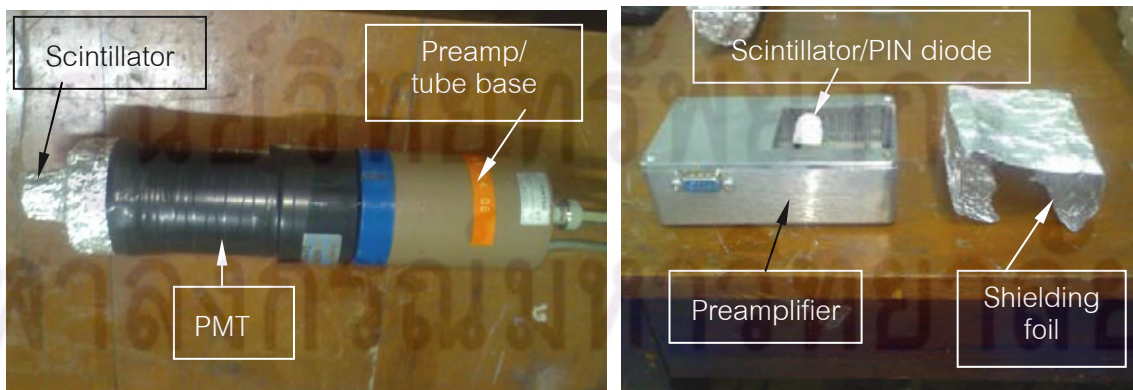


Fig. 3.12 Scintillator coupling with PMT and PIN photodiode for scintillation detector

3.3 Energy spectroscopy system

3.3.1 Test system configuration

The system for scintillation detection performance testing was configured as an energy spectroscopy system as shown in Fig. 3.13. Two front-end stages could be switched and one at a time was connected to the energy spectroscopy system in the NIM standard, containing a set up of Ortec model 478 high voltage, Canberra model 2022 spectroscopy amplifier, Tracor northern model TN1706 multichannel analyzer (MCA) interfaced with a notebook computer, for energy spectral data storage and calculation. The energy resolution evaluation program was also developed for readout of peak energy and full width at half maximum (FWHM) on the energy spectrum according to Equation 3.2, to support this performance testing.

$$\text{Energy resolution} = \frac{\text{FWHM}}{\text{Peak energy}} \times 100\% \quad (3.2)$$

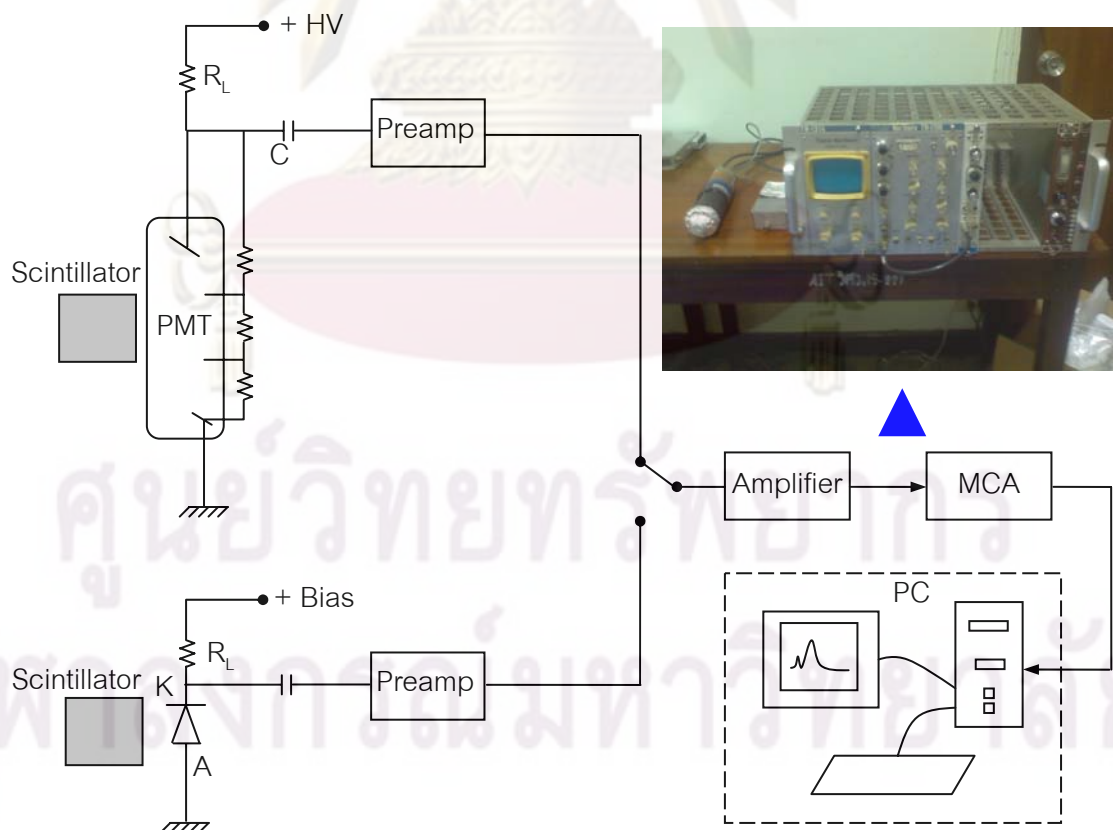


Fig. 3.13 Energy resolution test system for scintillator

3.3.2 Front-end under test stage

There were two front-end stages configured, the scintillator coupling with the PMT and the scintillator coupling with the PIN photodiode. In the scintillator coupling with the PMT assembly, the photomultiplier tube output was amplified by Ortec 276 preamplifier/tube base followed by a spectroscopy amplifier set to suitable shaping time and gain. This output was digitized including histogrammed with a multichannel analyzer and the analyzed data was sent to a computer via an RS232 port. For the scintillator coupling with the PIN photodiode assembly, the Cremat, Inc. CR-110 integrated circuit of charge sensitive preamplifier was employed for the front-end stage and configured as shown in Fig. 3.14. The signal output was sent to the spectroscopy system in the same process as with the PMT-coupled configuration.

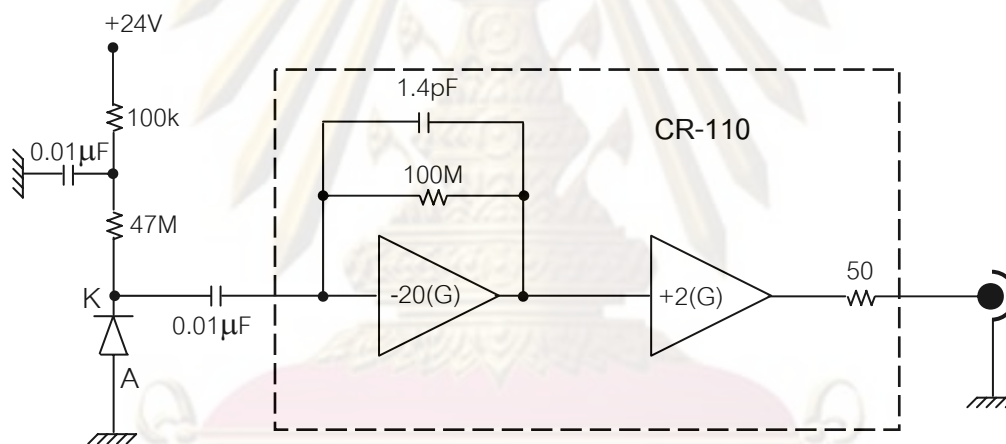


Fig. 3.14 Front-end stage configured of PIN photodiode for scintillator assembly

CHAPTER IV

EXPERIMENTS AND RESULTS

The developed equipment in Chapter III was employed for crystal growing experiments in 3 parts. Firstly, the conventional Bridgman and moving-temperature-gradient furnaces were tested for the performance and evaluated the temperature gradient and the growth rate. Secondly, three types of CsI:Tl, LaCl₃:Ce and Ba₂CsI₅:Tl crystals were grown with proper preparation and conditions of temperature gradient and growth rate. Finally, the scintillation crystals were encapsulated and coupled with a photosensitive device for radiation detection performance testing in comparison with commercial NaI:Tl crystal.

4.1 Furnace performance test

In this research we grew commercial CsI:Tl crystals, well-known high performance LaCl₃:Ce crystals and new Tl doped ternary compound of Ba₂CsI₅ crystals which were different in melting point and crystal size properties. These crystals were grown under different conditions. In furnace performance test, the furnace test run was based on the highest melting point of the crystal which is LaCl₃:Ce (860°C). And the furnace was operated with complete system set up but without materials loaded in the crucible. The temperature characteristic along the growth zone was recorded during the growth process to determine the start up response time and the temperature gradient of the developed furnace.

In melting period testing, the times to reach the melting point of both furnaces are nearly the same. It depended on the different temperature set points of higher temperature and lower temperature furnace elements. Normally, higher temperature will be set above the melting point and lower temperature was selected for the required temperature gradient. The furnace test run for LaCl₃:Ce crystal growing parameter was set at high and low temperature furnace of 950 and 900 °C, respectively and temperature histories at 3 positions were recorded: high temperature furnace, growth zone and low temperature furnace, as shown in Fig. 4.1. It was found that the furnace response time to reach the set point was 5 hours at the ramp up rate of

180 °C/hr. And it took approximately 8 – 11 hours for steady-state heating in the growth zone, after which the solidification period started.

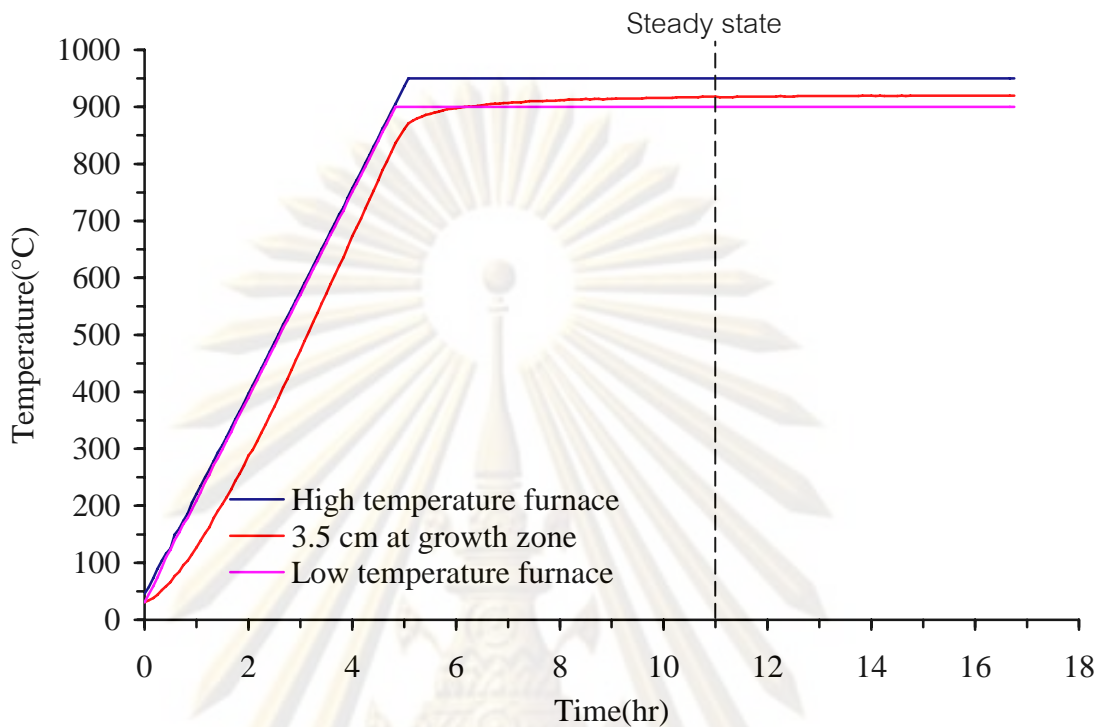


Fig. 4.1 Temperature response of the furnace during melting period for $\text{LaCl}_3:\text{Ce}$ growth

4.1.1 Temperature gradient of Conventional Bridgman furnace

For solidification period testing, the temperature gradient at the growth zone of the furnace was configured with three values between 10 – 30 °C/cm, depending on the growing parameter of the growth crystal. Because different charge materials exhibit different melting points, the high and low temperature set points must be changed for each crystal growth. In conventional Bridgman furnace, the temperature gradient of the furnace could be tentatively set by setting different temperature set points of higher temperature and lower temperature furnace elements, while keeping the temperature above the melting point at about 4 cm from the bottom of the growth zone.

Test runs of three different temperature gradients along the growth zone of the developed conventional Bridgman furnace for $\text{LaCl}_3:\text{Ce}$ crystal growing were illustrated. Each temperature profile was measured by moving a temperature probe in 5 mm step along the growth zone as shown in Fig. 4.2. Tested results showed three different temperature gradients of 11.2, 21.6 and 30.0 °C/cm. The growth rate could be

adjusted through the translation speed according to the length of the growth zone from 0.5 cm to 7.5 cm.

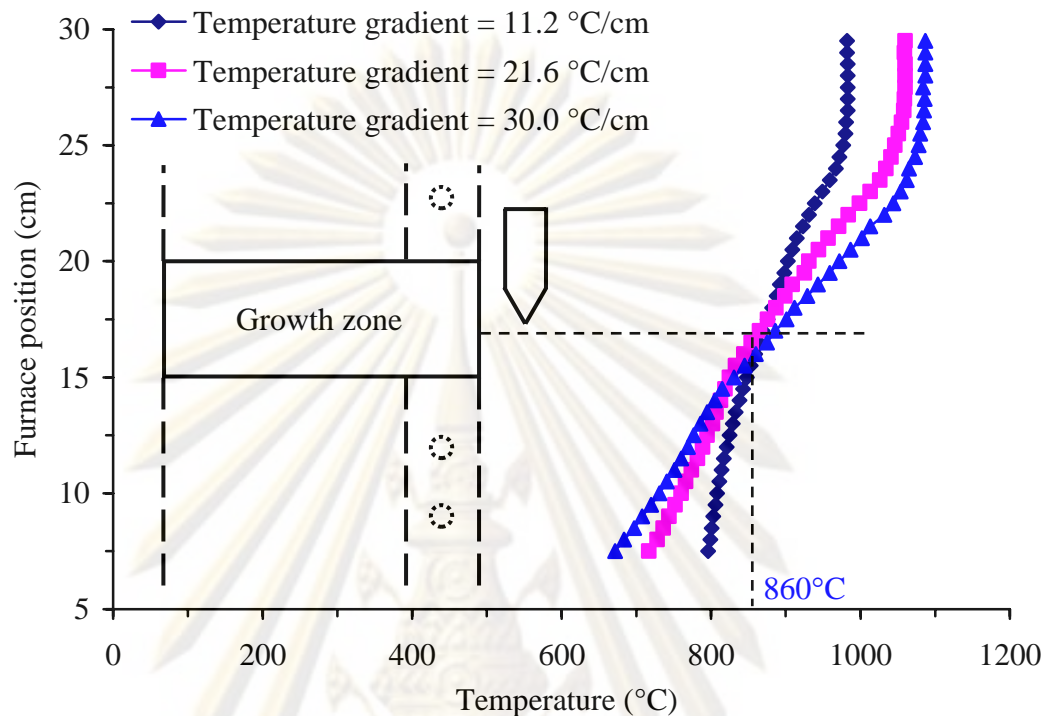


Fig. 4.2 Temperature gradient for $\text{LaCl}_3:\text{Ce}$ crystal growing

4.1.2 Temperature gradient of Moving-temperature-gradient furnace

In the moving-temperature-gradient furnace, the differential temperature reduction rates of higher and lower temperature furnace elements are independently controlled in the middle of the heating zone. Movement of the temperature gradient could be generated with constant temperature gradient drift rate of dual furnace elements along the growth zone by setting high and low temperature set points on the temperature controller.

For a test run of the furnace based on the melting point of the crystal such as CsI:Tl (621°C) at the expected crystal growth rate of 1 mm/hr using the differential ramp-down temperature gradient of 25.50°C/cm , the moving temperature along the 8 cm growth zone during the solidification period was evaluated. The temperature at each step of 5 mm position from the growth zone was measured every

10 hours for a period of 80 hours. A plot of the moving temperature gradient curves along the vertical axis of the crucible is shown in Fig. 4.3.

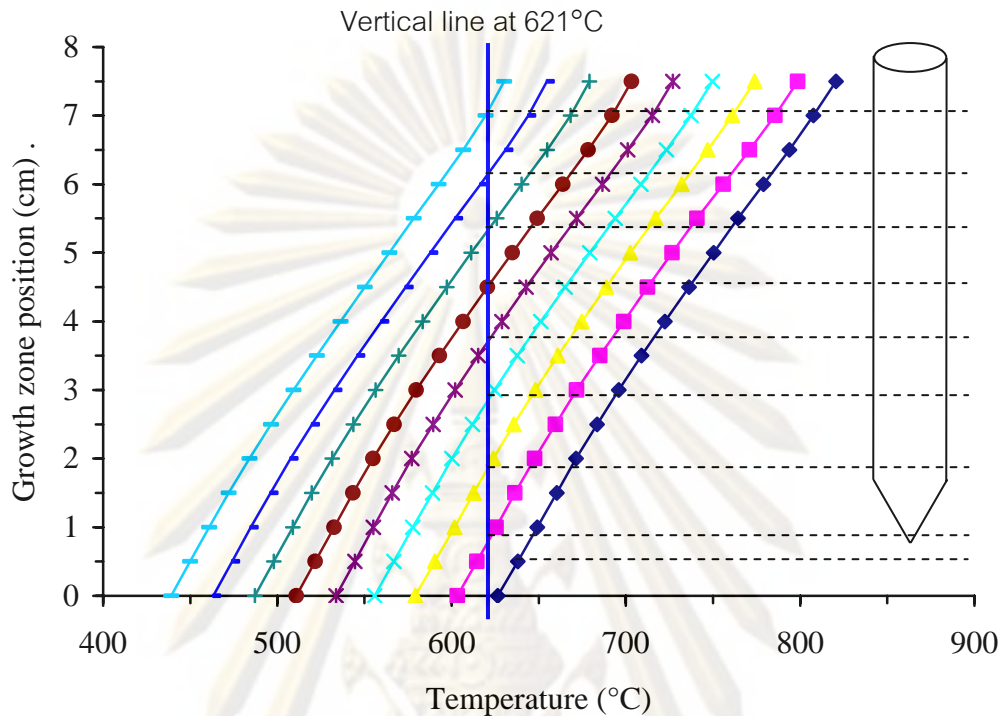


Fig. 4.3 Moving-temperature-gradients along the 8 cm growth zone

The temperature gradient on each curve at the vertical axis line of 25.50, 25.52, 25.36, 25.54, 25.84, 25.86, 26.00, 26.02 and 26.22 °C/cm was obtained from the bottom to the top zone of the growth zone, sequentially. It was found that the maximum difference of the temperature gradient of the growth zone was less than $\pm 2.82\%$. Fig. 4.4 illustrates the temperature gradient drift rates at 5 elevations along the furnace zone. Result of the controlled temperature gradient drift rate of high and low temperature heating zones is 2.5 °C/hr, while the temperature gradient drift rates of the growth zone at 1, 3 and 5 cm positions are 2.33, 2.32 and 2.31 °C/hr, respectively. A 6% maximum slope difference of the temperature gradient drift rate compared to the calculated trend line was found. From the combination of the temperature gradient drift rate and the temperature gradient, a crystal growth rate of 1 mm/hr was obtained according to Eq. (3.1). A plot of the furnace temperature profile at the vertical axis of the growth zone is shown in Fig. 4.5.

Different temperature profiles at the vertical axis of the growth zone could be changed by setting the differential ramp-down temperature gradient at the programmable temperature controller. The differential temperature reduction rates of higher and lower temperature furnace elements were generated.

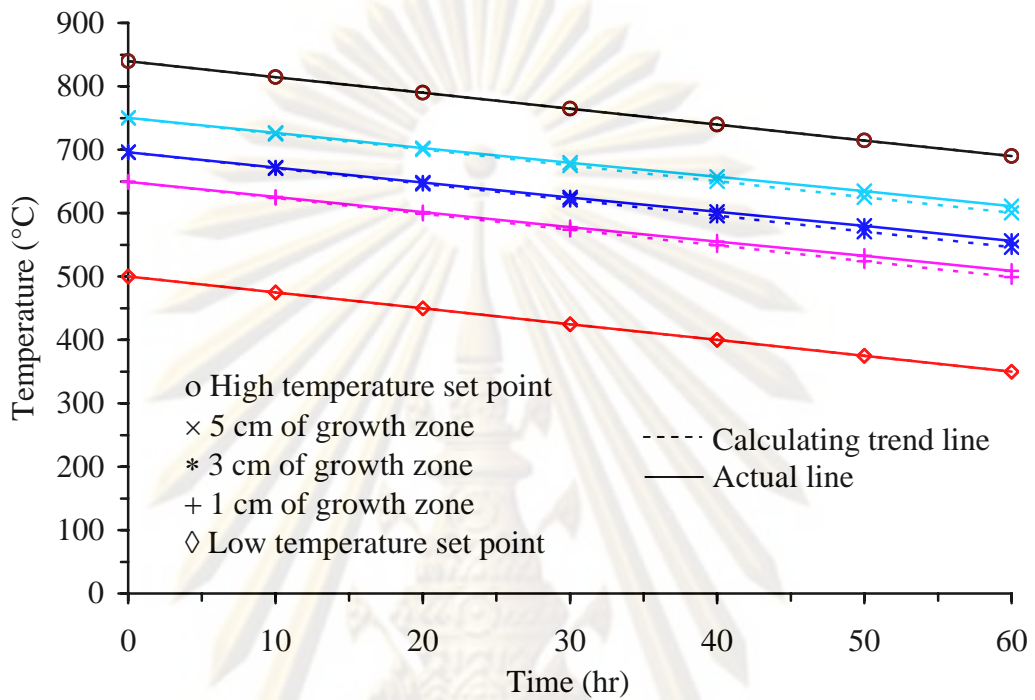


Fig. 4.4 Temperature gradient drift rate along the growth zone

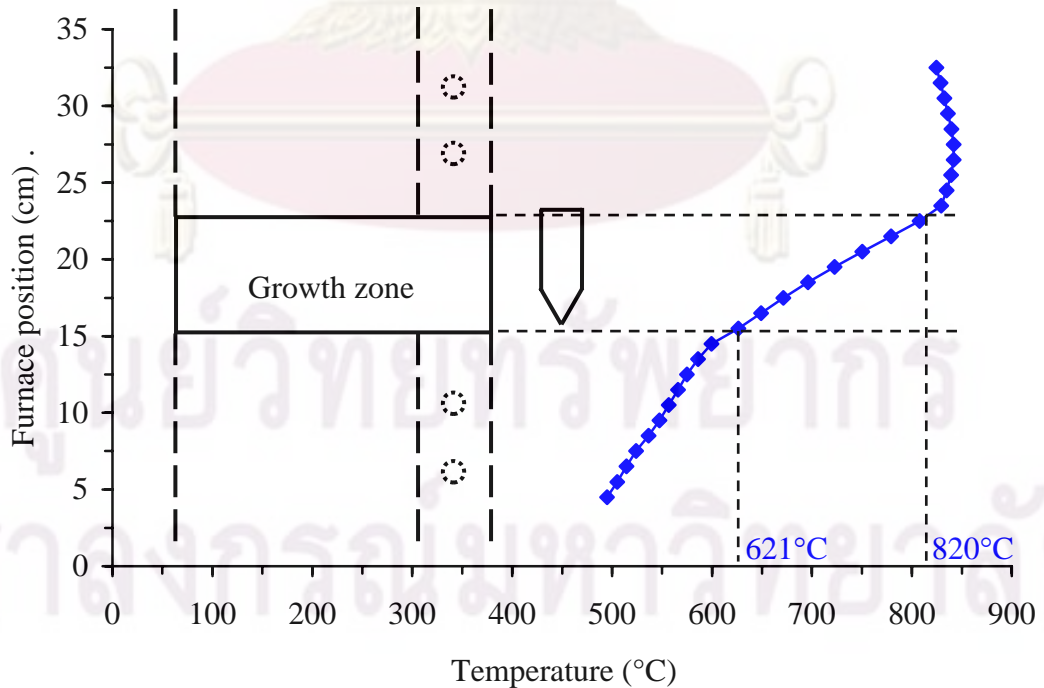


Fig. 4.5 Temperature profile at the temperature gradient of 25.50 °C/hr

4.1.3 Evaluation of furnace

Preliminary test runs for small-size CsI:Tl of 10 mm diameter crystal growing were done, with nearly the same charge preparation of CsI mixed with 0.6095 and 0.5935 wt% Tl for conventional and moving-temperature-gradient furnaces, respectively. The same growth condition with the growth rate of 1 mm/hr and the temperature gradient of 25.5 °C/cm in both conventional Bridgman and moving-temperature-gradient furnaces was used. New design of a crucible translation with direct coupling linear driving mechanic in conventional furnace helps to eliminate a gear box system, resulting in a much reduced vibration. In comparison, both grown crystals exhibited no significant crystal quality difference as shown in Table 4.1.

Table 4.1 The growth crystal quality from conventional and modified Bridgman furnaces

Furnace type	Visible light transmittance at λ 400-700 nm (%)	Crystal surface	Energy resolution at 662 keV (%)	Relative pulse height
Conventional	81	Clear	8.53	94
Modified Bridgman	81	Clear	8.30	100

4.2 Crystal growing

From the furnace tested results and the advantage of the moving-temperature-gradient technique, the moving-temperature-gradient furnace was mostly used in our experiments of this research. Three types of doped scintillators, e.g., commercial scintillator CsI:Tl, high energy resolution LaCl_3 :Ce and high density with high energy resolution ternary compound of Ba_2CsI_5 :Tl have been grown using the powder melt-mixing process.

Before the beginning of the crystal growing experiment, the compound materials to be grown as scintillation crystal were studied in chemical and physical properties, e.g., chemical form, chemical reaction, density, melting point, crystal structure, and phase diagram. Three properties of compounds for scintillation crystals, CsI:Tl, LaCl_3 :Ce, and Ba_2CsI_5 :Tl, are listed in Appendix C. From literature survey, the grown crystal of binary compound, CsI:Tl and LaCl_3 :Ce, should be a bulk single crystal without cracks while ternary compounds were hard to grow into crystal without cracks.

The performance of growth scintillation crystals for gamma-ray spectrometry is generally evaluated from the energy resolution and the pulse height signal, which are directly related to the bulk crystal quality. Improvement of crystal quality for energy resolution can be determined from the Poisson prediction of energy resolution limit from Eq. (2.3) which is given by $R = 2.35\sigma/\sqrt{n}$, where n is amount of electrons collected from the photocathode and multiplied in the photomultiplier tube. This carrier charge output from the PMT creates a pulse height signal corresponding to its energy absorption in the crystal. Photoelectrons from a photocathode, however, are generated from illumination of scintillated photon from a coupled crystal. Therefore, in order to improve the energy resolution, one must increase the number of photons per energy (Photon/MeV) or photon light yield at a photocathode. There are two ways in research planning for increasing the crystal photon light yield:

1. Crystal growing process control for improving scintillated light generation such as improvement of crystal density for gamma-ray energy absorption, varying doped concentration for suitable site center and designing growth parameters to achieve single crystal perfection with minimal defects (no crack and good optical quality).
2. Crystal assembly for scintillated light enhancement such as light reflection back to a photocathode, selection of matched photocathode type to crystal emission wavelength and applying fluid coupling for refractive index matching.

4.2.1 Commercial CsI:Tl crystal growing

In CsI:Tl crystal growing, the powder compound of CsI of 99.9% purity mixed with TlI dopant of 99.9% purity at concentration varying in the range of 0.0915 - 0.7110 wt% was grown with a size of 10 mm diameter and approximately 30 mm length (including the conical part) using open-ended crucible. The moving-temperature-gradient furnace parameter setting for the growth rate of 1 mm/hr from the temperature gradient of 25 °C/cm and the temperature gradient drift rate of 2.5 °C/hr was applied. The charge material preparation for 10 mm diameter CsI:Tl crystal is shown in Table 4.2.

Table 4.2 Charge material preparation for 10 mm diameter CsI:Tl

Sample	Mass of CsI (g)	Mass of TlI (mg)	wt% Tl
M001	11.1412	10.20	0.0915
M002	11.3070	40.51	0.3570
M003	12.4369	22.47	0.1803
M004	11.8062	84.54	0.7110
M005	09.1600	54.69	0.5935

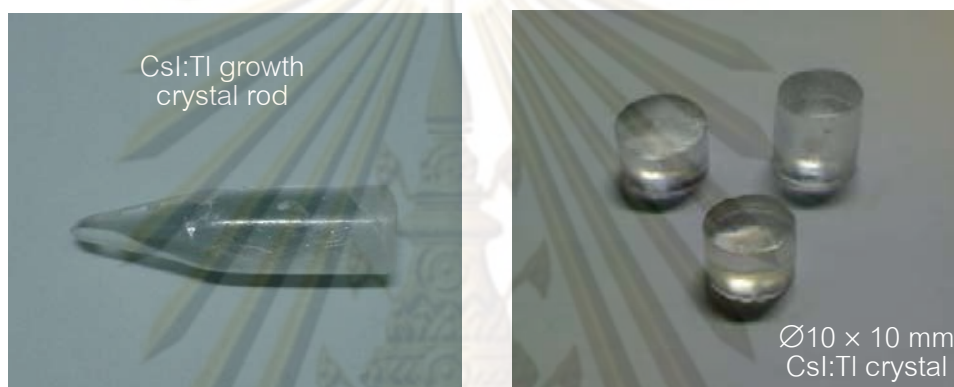
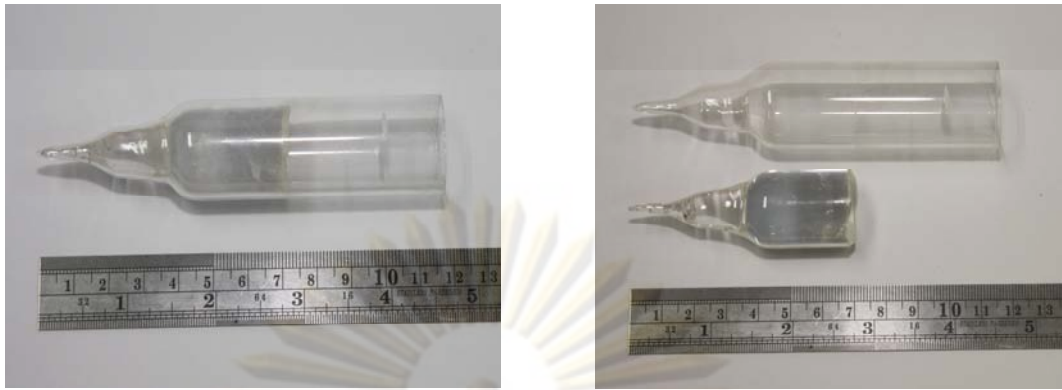


Fig. 4.6 Grown crystal of 10 mm diameter CsI:Tl

By visual inspection, the grown crystal rods appeared to be completely grown with clear color and no crack. The crystal light transmittances in range of 79 - 81% were found. Each growth crystal rod was cut into 10 mm length, polished at both ends as shown in Fig. 4.6, and assembled with a photomultiplier tube or a PIN photodiode to form a scintillation detector. Radiation detection performance tests in Section 4.3.1 showed that the highest energy resolution and the relative pulse height of small-size CsI:Tl crystal was found at 0.3570 wt% Tl and 80% light transmittance.

From those experimental results, the optimum Tl concentration was applied for charge material preparation and for growing a large $\text{Ø}22 \times 70 \text{ mm}^3$ CsI:Tl crystal. The grown crystal was also clear without cracks and it was easy to remove from the crucible as shown in Fig. 4.7. The grown CsI:Tl crystal was encapsulated and assembled with a photomultiplier tube or a PIN photodiode to form a scintillation detector. The energy resolution and relative pulse height tested results are illustrated in Section 4.3.1.



a) Grown crystal in crucible

b) Grown crystal after remove from crucible

Fig. 4.7 Crystal growth crucible and Csl:TI of 22 mm diameter and 70 mm length

4.2.2 High performance $\text{LaCl}_3:\text{Ce}$ crystal growing

In $\text{LaCl}_3:\text{Ce}$ crystal growing, the powder compound of LaCl_3 of 99.9% purity mixed with CeCl dopant of 99.9% purity at concentration varying in the range of 0.40 - 18.91 wt% were grown with diameter of 10, 14 and 22 mm and approximately 30, 50 and 70 mm length using sealed ampoule and open-ended crucible. The furnace parameter setting at crystal growth rate of 1 mm/hr with the temperature gradient of 25 °C/cm for conventional Bridgman and temperature gradient drift rate of 2.5 °C/hr for moving-temperature-gradient crystal growing were applied. Because LaCl_3 is hygroscopic and very chemical active, the charge material preparation must be done in the glove box. The preparation process is described in Chapter III.

The grown crystals were not completely grown, as most of the crystals cracked even in sealed ampoule type. By chemical soluble test, the crystals could not complete dissolve in water. These results indicated that the chemical reaction of LaCl_3 or CeCl_3 with moisture or oxygen took place and formed some compounds of LaOCl and CeOCl or La_2O_3 and CeO_2 . Obviously, the problem was originated from the impurity from the chemical reaction of $\text{LaCl}_3:\text{Ce}$ and moisture or oxygen during the solidification period. This means that the preparation process could not reduce moisture or oxygen low enough to prevent moisture absorption into the charge material or oxygen in a crucible. Fig. 4.8 illustrates a white powder and some solid substance formed in a cracked crystal. However, in an attempt to significantly reduce moisture or oxygen in the

preparation process of the 10 mm diameter crystal, the grown crystal appeared clearer but some cracks still formed in the crystal with the impurity coating on the crucible surface as shown in Fig. 4.9. This small piece of clear crystal was assembled with a PMT and its performance was evaluated. Radiation detection was done in the glove box for moisture prevention. The energy resolution tested results are illustrated in Section 4.3.2

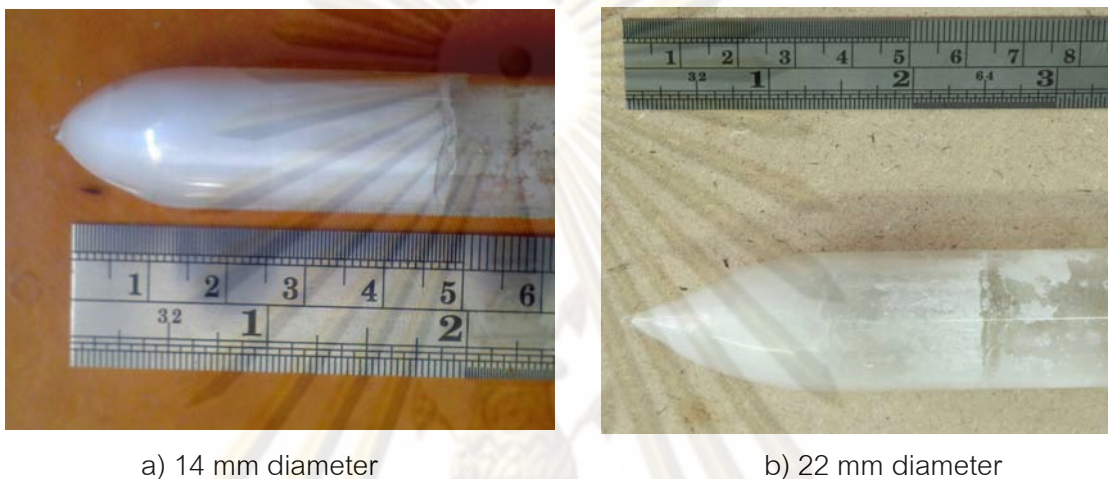


Fig. 4.8 Grown crystal of $\text{LaCl}_3:\text{Ce}$



Fig. 4.9 Grown crystal of $\text{LaCl}_3:\text{Ce}$ with clearer and partially cracked interior

จุฬาลงกรณ์มหาวิทยาลัย

4.2.3 Ternary compound of Ba₂CsI₅:Tl crystal growing

In growing the crystal of Ba₂CsI₅ ternary compound, the ternary compound of Ba₂CsI₅ was prepared from the chemical reaction between BaI₂ at 98% purity, CsI at 99.9% purity and TlI at 99.999% purity with a BaI₂:CsI mole ratio of 2:1. The chemical reaction is shown in Eq. (4.1).



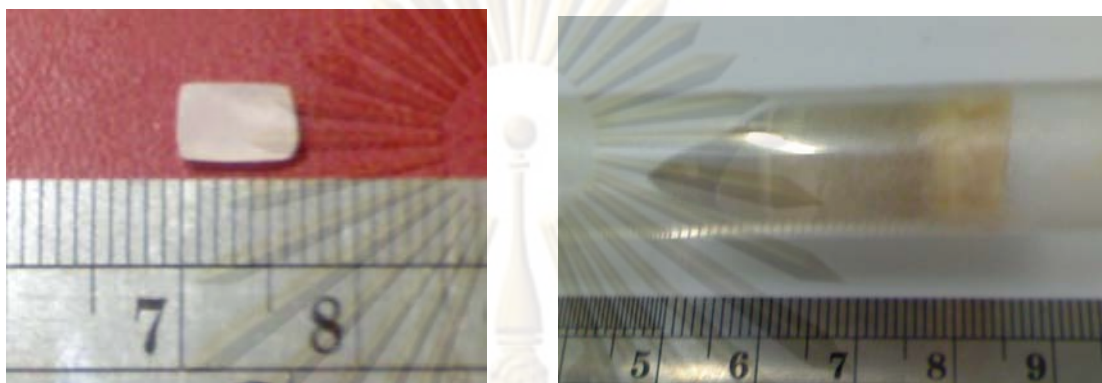
The powder mixtures of BaI₂ and CsI with TlI dopant at concentrations varying in the range of 0.0366 - 4.8190 wt% were prepared. Ba₂CsI₅:Tl crystals were grown with 10 mm diameter and approximately 30 mm length using open-ended and multi-crucible. The moving-temperature-gradient furnace parameter setting at the growth rate of 1 mm/hr from the temperature gradient of 25 °C/cm and the temperature gradient drift rate of 2.5 °C/hr was applied. The charge material preparation of 10 mm diameter Ba₂CsI₅:Tl crystals is shown in Table 4.3.

Table 4.3 Charge material preparation of 10 mm diameter crystals of Ba₂CsI₅:Tl

Sample	Mass of BaI ₂ (g)	Mass of CsI (g)	Mass of TlI (mg)	Tl wt%
M001	7.5117	2.5854	Undoped	-
M002	7.5126	2.4718	101.4	1.0050
M003	7.5705	2.5364	12.2	0.1211
M004	7.5678	2.53254	3.7	0.0366
M005	5.755	2.01961	39.1	0.5004
M006	5.6765	2.0481	179.1	2.2660
M007	5.7934	1.878	388.4	4.8190

Although the BaI₂ compound is hygroscopic, the charge material preparation could be done in normal atmosphere because the charge could be dried by thermal dehydration process before the start of crystal growth. All grown crystals cracked and they can easily be removed from the crucible. It was also found that iodide segregation on the top of the crystals appeared due to decomposition of iodide as shown in Figs. 4.10b and c. The grown crystal piece was selected and polished to

obtain a small sample with the size approximately $6 \times 3 \times 1 \text{ mm}^3$, as shown in Fig. 4.10a. The sample was assembled with a PMT for energy resolution test. Radiation detection was also done in the glove box for moisture prevention. The energy resolution tested results are shown in Section 4.3.2



a) Polished crystal

b) 10 mm diameter grown crystal



c) Multi-crucible grown crystals

Fig. 4.10 Grown crystals of $\text{Ba}_2\text{CsI}_5:\text{Tl}$

4.3 Crystal performance test

Grown crystals of $\text{CsI}:\text{Tl}$, $\text{LaCl}_3:\text{Ce}$ and $\text{Ba}_2\text{CsI}_5:\text{Tl}$ were observed in crystal quality and tested for radiation detection performances on both the energy resolution and the detection efficiency. Cut and polished crystals were brought to test the light transmittance before coupled with a matched PMT for scintillation detection. Only $\text{CsI}:\text{Tl}$ was coupled with both a PMT and a PIN photodiode for scintillation detection, because its emission wavelength matched the spectral response of the PIN

photodiode. Besides, the CsI:TI crystal was encapsulated and the effect of photon signal enhancement with a white Teflon tape reflector was also studied.

4.3.1 CsI:TI scintillation crystal

a) Tested results of energy resolution and relative pulse height of CsI:TI are presented. The relationships of energy resolution and relative pulse height with respect to the TI dopant concentration, when coupling the scintillation crystal with the white Teflon tape reflector to photosensitive devices of the Hamamatsu model 52154-02 PMT and the Hamamatsu model S3590-8 PIN photodiode are listed in Table 4.4. The plots of energy resolution and relative pulse height with respect to the TI dopant concentration are shown in Figs. 4.11 and 4.12, respectively.

Table 4.4 Results of energy resolution and relative pulse height of CsI:TI

Sample	TI doped (wt%)	Coupling with PMT		Coupling with PIN photodiode	
		Energy resolution (%)	Relative pulse height (%)	Energy resolution (%)	Relative pulse height (%)
M001	0.0915	14.86	57.86	22.54	62.21
M002	0.3570	7.19	100	8.60	100
M003	0.1803	8.74	73.91	10.56	84.35
M004	0.7110	10.46	64.88	13.77	68.32
M005	0.5935	8.30	83.10	10.50	86.64

Theoretically, the pulse height signal is proportional to the scintillation light yield emission of CsI:TI crystal and is dependent on the TI concentration. In this experiment, the highest energy resolution and relative pulse height are found at 0.3570 wt% TI. In larger size CsI:TI crystal growth, the crystal size of 22 mm diameter and 70 mm length with a 0.3602 wt% TI was successfully grown. Comparison of the energy resolution from a Cs-137 gamma-ray spectrum between $\text{Ø}10 \times 10 \text{ mm}^3$ and $\text{Ø}22 \times 22 \text{ mm}^3$ CsI:TI crystals coupling with a PMT is shown in Fig. 4.13. The energy resolution of $\text{Ø}10 \times 10 \text{ mm}^3$ and $\text{Ø}22 \times 22 \text{ mm}^3$ CsI:TI crystals were found to be 7.19% and 7.53%, respectively.

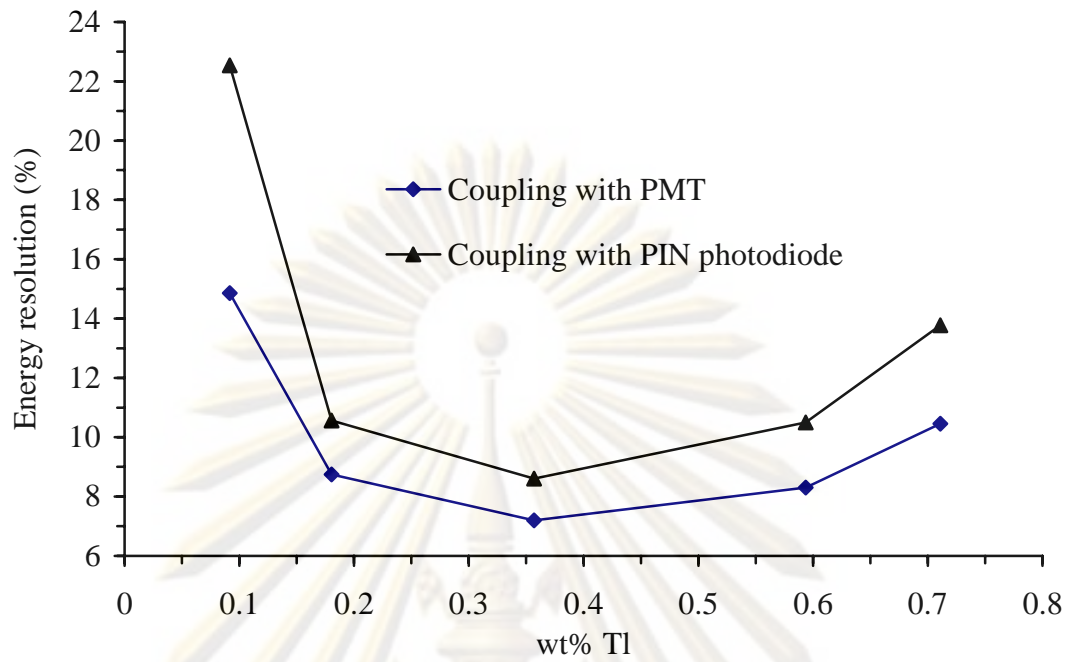


Fig. 4.11 Relationship between TI dopant concentration and energy resolution

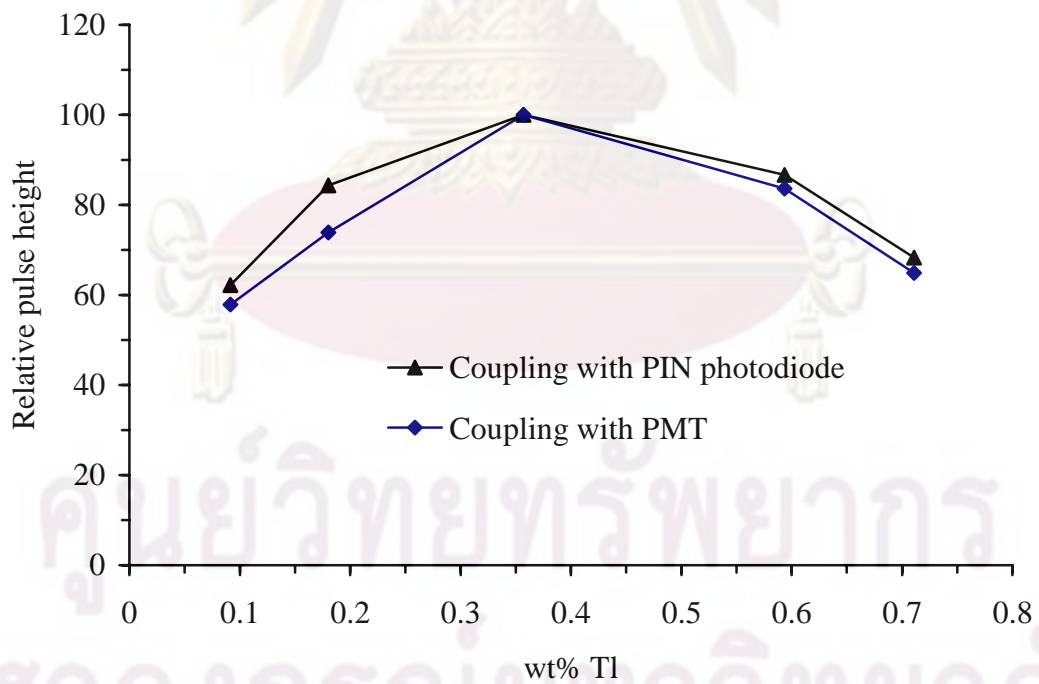


Fig. 4.12 Relationship between TI dopant concentration and relative pulse height

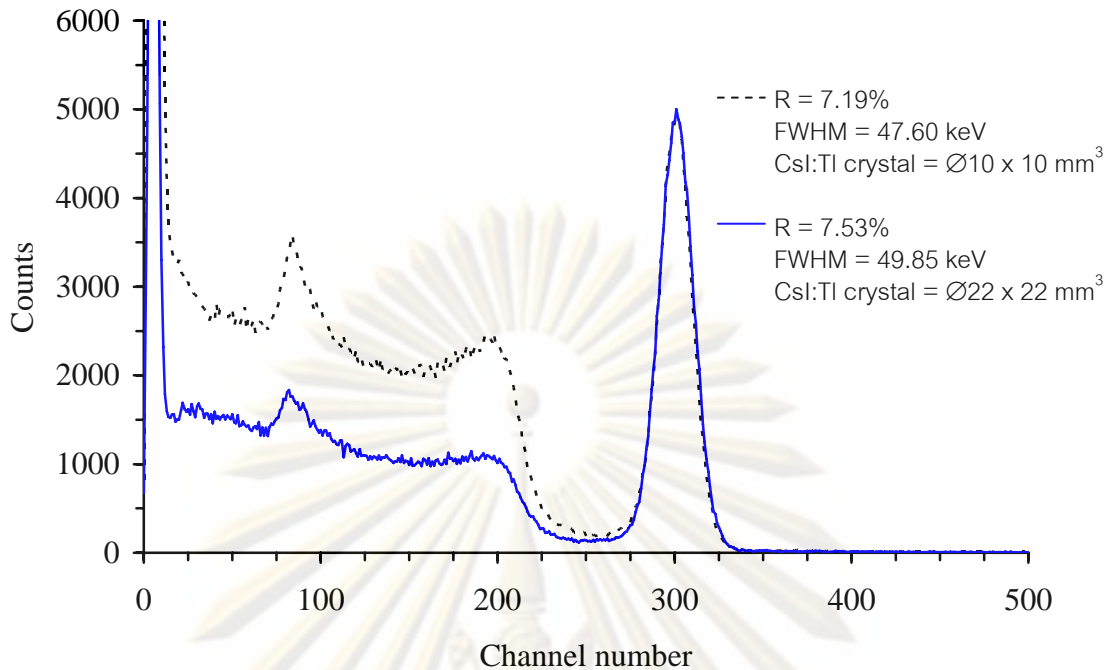


Fig. 4.13 Comparison of Cs-137 gamma energy spectrum of $\text{Ø}10 \times 10 \text{ mm}^3$ and $\text{Ø}22 \times 22 \text{ mm}^3$ CsI:Tl coupling with PMT

b) The crystals transparent to the wavelength of its own scintillated light emission were tested using a transmission meter from EDTM model SD2400. Visible light transmittance at λ between 400 - 700 nm was selected for testing the 3 CsI:Tl crystals as shown in Table 4.5. The percentage transmittance of the crystal size of $\text{Ø}10 \times 10 \text{ mm}^3$, and $\text{Ø}22 \times 22 \text{ mm}^3$ were found to be approximately 80% and 74%, respectively.

Table 4.5 The grown crystal quality from conventional and modified Bridgman furnaces

Growing method	Crystal size (mm^3)	% transmittance at 400 – 700 nm
Conventional Bridgman-Stockbarger	$\text{Ø}10 \times 10$	81
Moving-temperature-gradient	$\text{Ø}10 \times 10$	80
Moving-temperature-gradient	$\text{Ø}22 \times 22$	74

c) For scintillated light yield enhancement, the energy resolution and the pulse height were tested for comparing with the use of reflecting material and encapsulation on CsI:Tl $\text{Ø}22 \times 22 \text{ mm}^3$. Three configurations were tested: aluminum foil

wrapped with non encapsulation, white Teflon tape reflector with non encapsulation and complete encapsulation with Teflon tape reflector and borosilicate light guide. The results are shown in Table 4.6.

Table 4.6 The scintillated light yield enhancement of CsI:TI crystals

Test condition	Energy resolution (%)	Relative pulse height (%)
Al foil wrapped with non encapsulation	10.05	86
Teflon tape reflector with non encapsulation	7.53	100
Encapsulation with Teflon tape and light guide	7.78	94

The results indicated that using a white Teflon tape reflector increased the energy resolution and the pulse height by 2% compared with the aluminum foil wrapped crystal. However, in complete encapsulation with borosilicate light guide, the pulse height decreased due to the absorption of the scintillated light in the light guide.

d) The Bicron model 1M1/2P commercial scintillation detector with NaI:TI crystal with a size of $\text{Ø}25 \times 25 \text{ mm}^3$ was tested on the performance of energy resolution. The gamma spectrum of Cs-137 from NaI:TI crystal in comparison with the developed CsI:TI crystal with a size of $\text{Ø}22 \times 22 \text{ mm}^3$ was shown in Fig. 4.14. The developed crystal exhibited a higher energy resolution and an intrinsic peak efficiency. Actually, the commercial high-grade crystals of NaI:TI and CsI:TI were found to be 6% and 7%, respectively, as shown in Appendix D.

e) The $\text{Ø}10 \times 10 \text{ mm}^3$ CsI:TI crystal with the white Teflon tape reflector was tested by coupling with a PIN photodiode as shown in Fig. 4.15. The energy resolution was found to be 8.60%, but some interference appeared at the low energy peak location of Ba characteristic x-ray in Cs-137 gamma spectrum due to a PIN photodiode noise. The junction diode noise is usually a disadvantage of the large area PIN diode and the cost is still high in comparison with a photomultiplier tube. The CsI:TI crystal coupled with a PIN photodiode is very popular in high energy applications requiring compact size, because CsI:TI exhibits a rather high density and is non-hygroscopic.

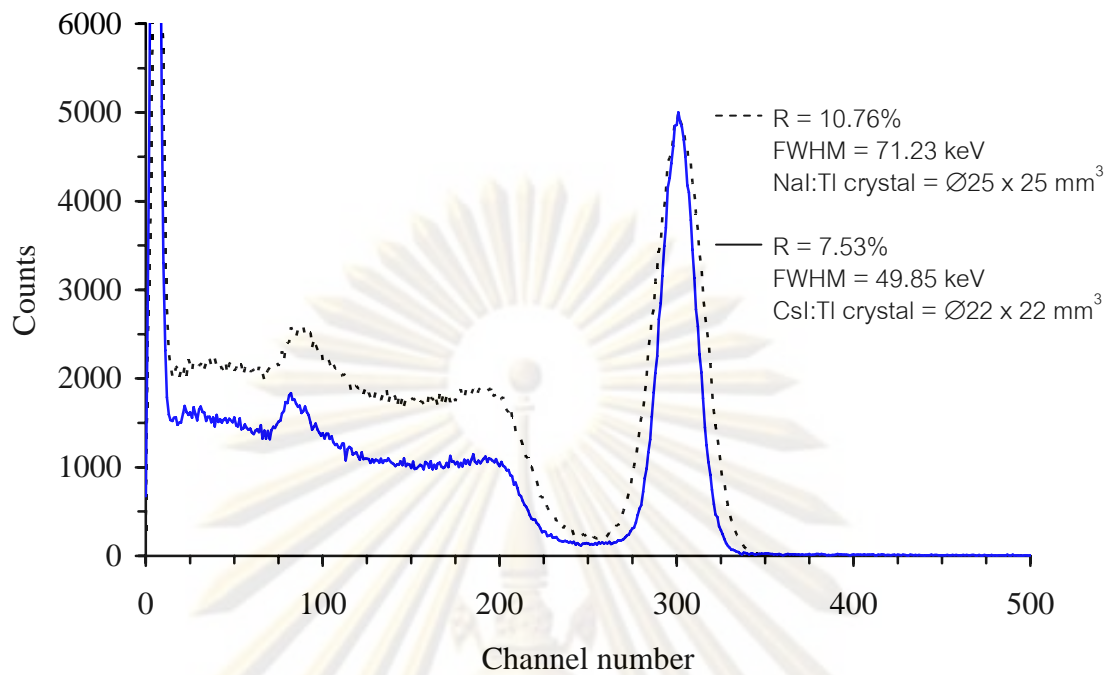


Fig. 4.14 Comparison of Cs-137 gamma energy spectrum of $\text{Ø}25 \times 25 \text{ mm}^3$ NaI:TI crystal and $\text{Ø}22 \times 22 \text{ mm}^3$ CsI:TI coupling with a PMT

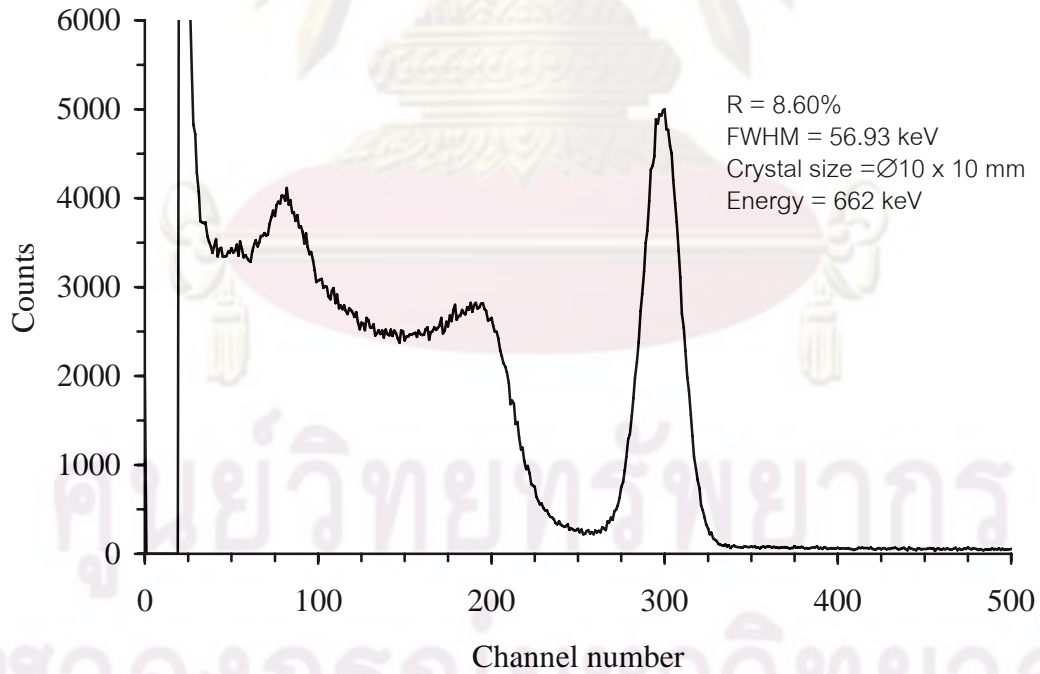


Fig. 4.15 Gamma energy spectrum of $\text{Ø}10 \times 10 \text{ mm}^3$ CsI:TI coupling with PIN photodiode

f) The detection efficiencies of $\text{Ø}10 \times 10 \text{ mm}^3$ CsI:TI crystal coupled with a PMT and a PIN photodiode were compared by detecting a Cs-137 spectrum at the counting time of 1000 seconds under the same source and detector geometry. The tested result was shown in Fig. 4.16 with total full energy peak counts of 108,082 and 108,172 for photosensitive device of PMT and PIN photodiode, respectively. By calculating the detection efficiency, it was found that the intrinsic peak energy of both detectors was not much different with the intrinsic peak energy difference of 0.08%. The results show that both PMT and PIN photodiode were equally detection efficiency.

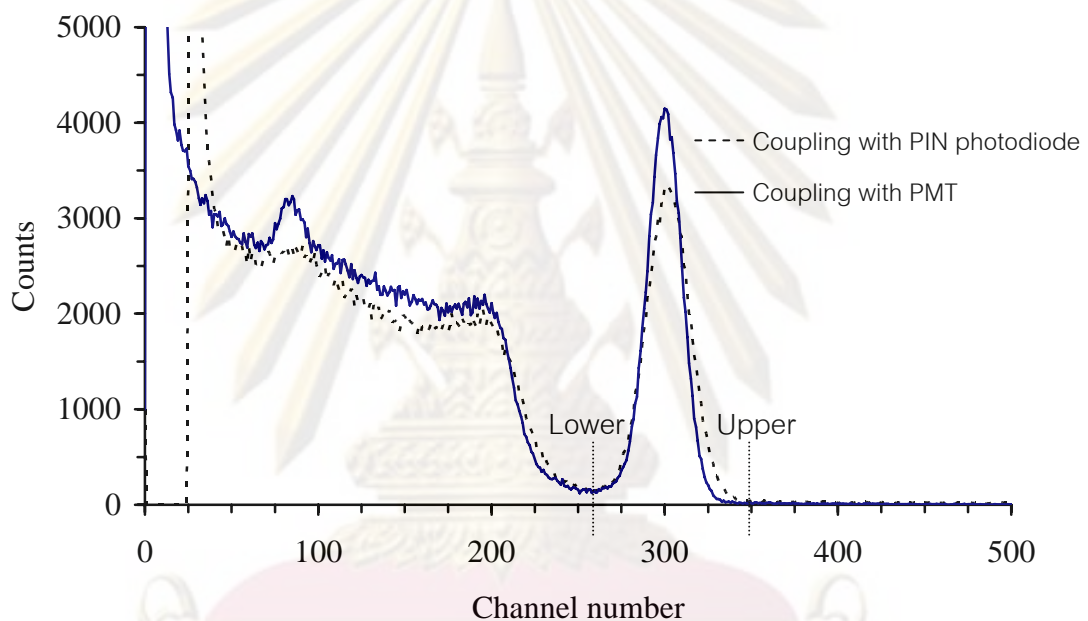


Fig 4.16 Comparison of photosensitive devices coupling with $\text{Ø}10 \times 10 \text{ mm}^3$ crystal

g) The developed CsI:TI crystals with crystal sizes of $\text{Ø}22 \times 22 \text{ mm}^3$ and $\text{Ø}10 \times 10 \text{ mm}^3$ and commercial NaI:TI medium grade crystal with a size of $\text{Ø}25 \times 25 \text{ mm}^3$ were tested. The standard gamma radiation sources of 122 keV, 662 keV and 1.33 MeV energy from Co-57, Cs-137 and Co-60, respectively, in different activities were employed for detection efficiency test. All measured spectrums are shown in Fig. 4.17. The calculation of intrinsic peak efficiency and peak efficiency is illustrated in Appendix E. Summary of grown crystals detection efficiency results is listed in Table 4.7. From the CsI:TI crystal growing experiment, it was illustrated that long crystals could be completely grown in the laboratory-scale level.

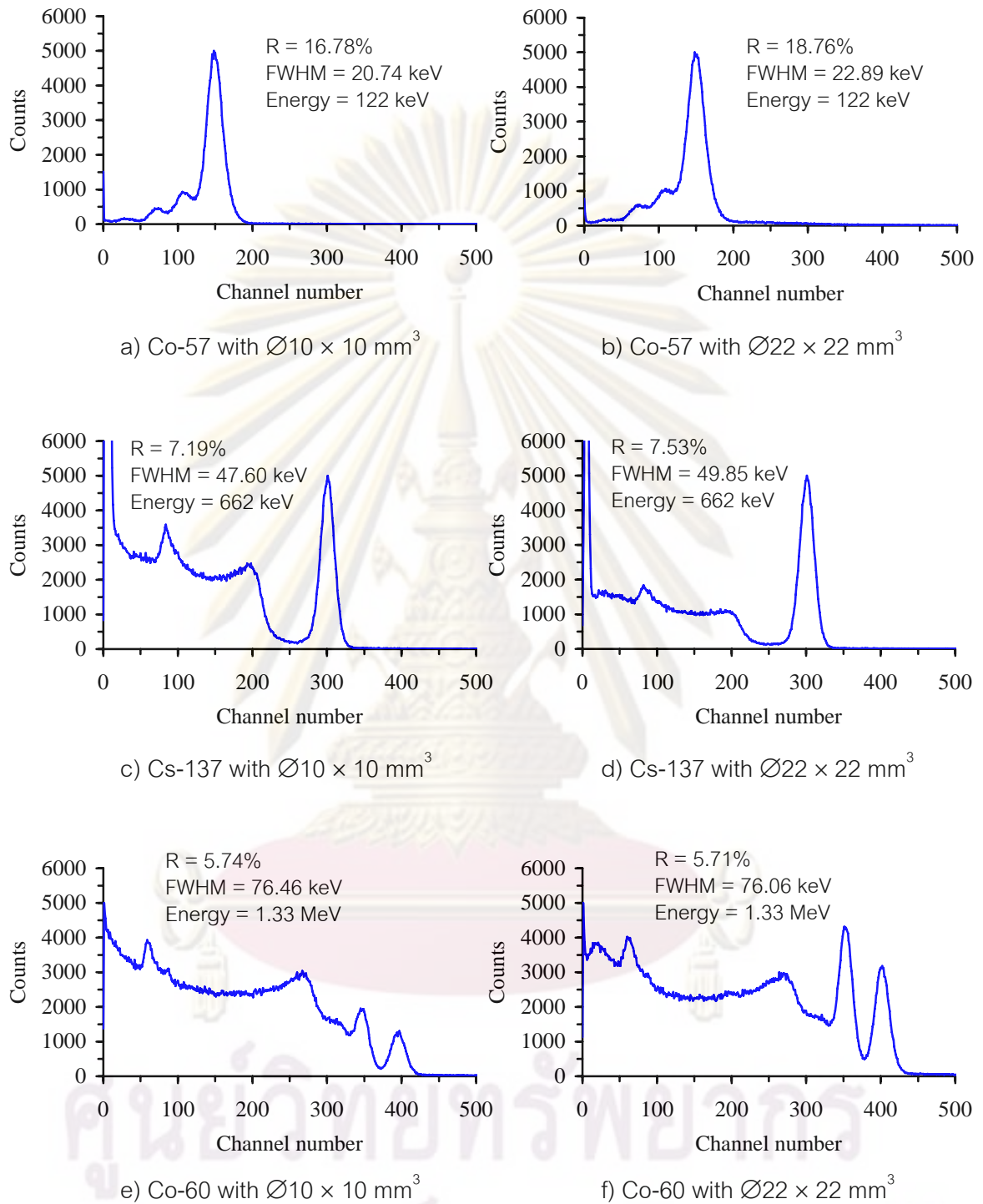


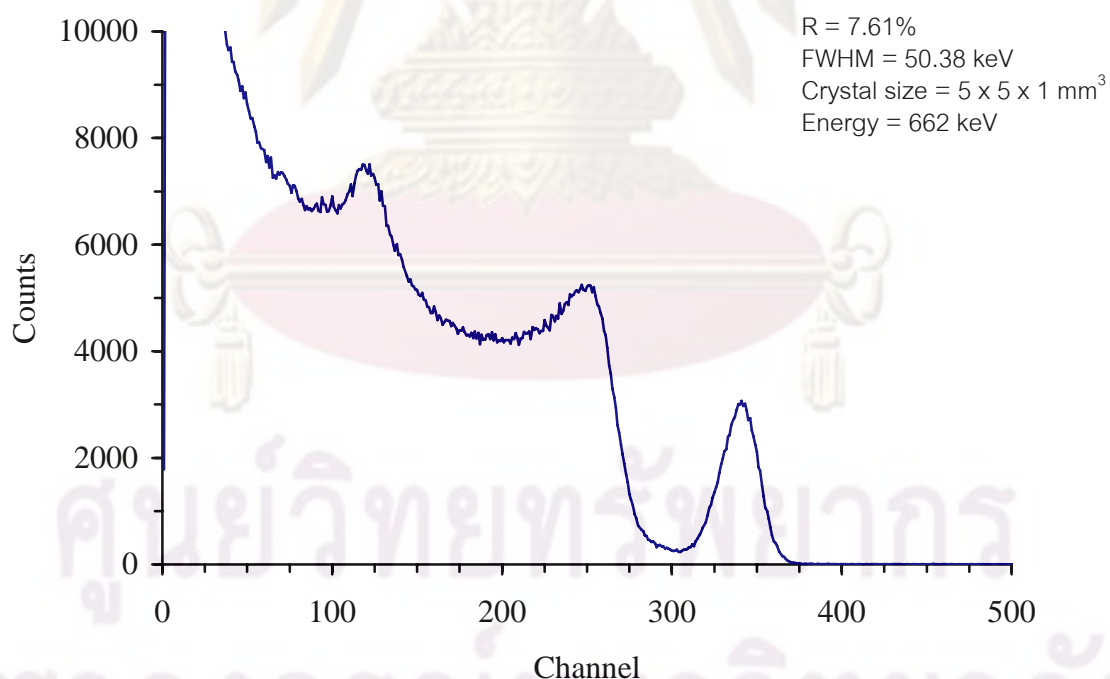
Fig. 4.17 Gamma spectrum under different energies for detection efficiencies evaluation

Table 4.7 Results of the detection efficiency of grown CsI:Tl crystal

Sample size (mm ³)	Tl doped (wt%)	Intrinsic peak efficiency (%)			Peak to Compton ratio	
		122 keV	662 keV	1.33 MeV	662 keV	1.33 MeV
Ø10 × 10	0.3570	56.68	2.50	0.36	2.28	0.51
Ø22 × 22	0.3602	94.90	10.35	2.08	4.58	1.30

4.3.2 LaCl₃:Ce scintillation crystal

The selection of clear piece of cracked LaCl₃:Ce crystal with dimensions 5 × 5 × 1 mm³ was tested for radiation detection in glove box. It was found that the energy resolution was 7.61% and that a small piece of crystal gave more Compton area in the spectrum as shown in Fig. 4.18. In comparing the energy resolution with CsI:Tl crystal in our experiment, even though the LaCl₃:Ce crystal was not completely grown, its energy resolution was compatible.

Fig. 4.18 Gamma energy spectrum of 5 × 5 × 1 mm³ LaCl₃:Ce

4.3.3 Ba₂CsI₅:Tl scintillation crystal

Tested results of energy resolution and relative pulse height with respect to the loaded Tl concentration of the Ba₂CsI₅:Tl ternary compound are shown in Table 4.8. The plots of energy resolution and relative pulse height with respect to the Tl dopant concentration are shown in Figs. 4.19 and 4.20, respectively. Undoped and 0.0366 wt% doped Tl could detect radiation, however, the photo peak cannot be separated from the Compton peak, which makes it hard to identify the photo peak. The energy resolution and the relative pulse height are optimized with the loaded Tl concentration of 1.0050 wt%.

Table 4.8 Results of energy resolution and relative pulse height of Ba₂CsI₅:Tl

Sample	Tl doped (wt%)	Energy resolution (%)	Relative pulse height (%)
M001	Undoped	NA	NA
M002	1.0050	12.53	100.00
M003	0.1211	15.79	58.30
M004	0.0366	NA	NA
M005	0.5004	12.94	79.76
M006	2.2660	13.28	70.45
M006	4.8190	17.03	52.23

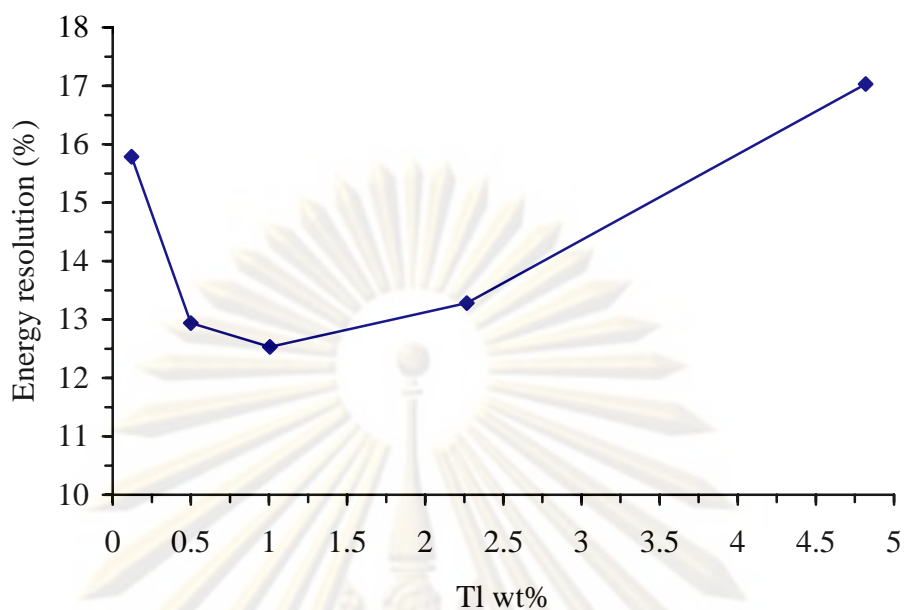


Fig. 4.19 Relation of doped Tl concentration with respect to energy resolution

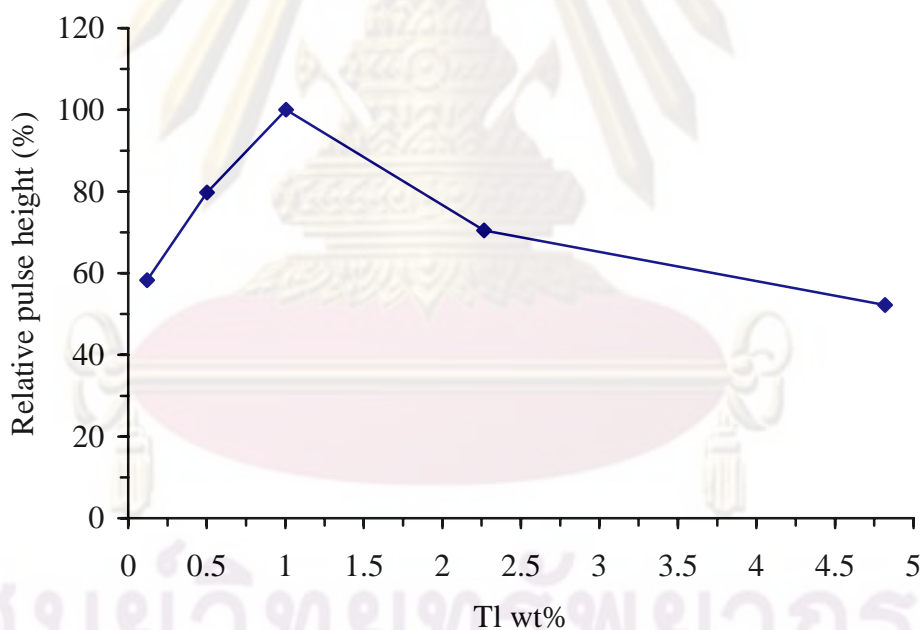


Fig. 4.20 Relation of doped Tl concentration with respect to relative pulse height

The selected clear piece of cracked $\text{Ba}_2\text{CsI}_5:\text{Tl}$ crystal with dimensions $6 \times 3 \times 1 \text{ mm}^3$ was tested for radiation detection in a glove box. It was found that the energy resolution was 12.53% at 1.005 wt% of Tl loaded in Ba_2CsI_5 as shown in Fig. 4.21. The energy resolution is quite low and, from literatures, this ternary compound should exhibit an energy resolution of about 4%.

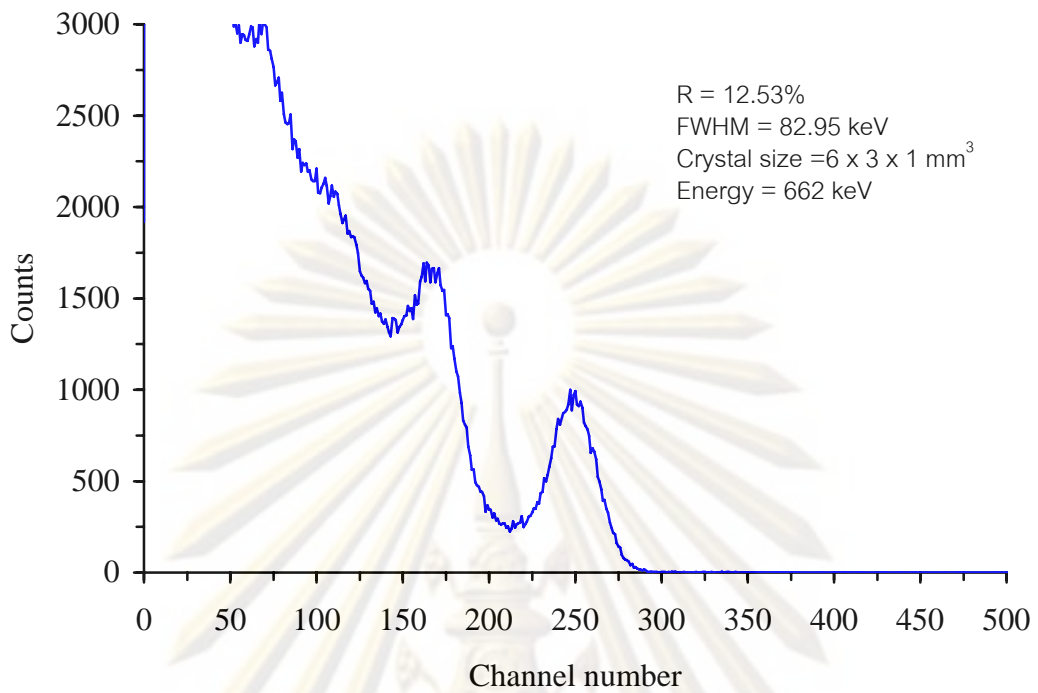


Fig. 4.21 Cs-137 gamma energy spectrum of $6 \times 3 \times 1 \text{ mm}^3$ $\text{Ba}_2\text{Csl}_5:\text{Tl}$

ศูนย์วิทยทรัพยากร
จุฬาลงกรณ์มหาวิทยาลัย

CHAPTER V

CONCLUSION DISCUSSION AND SUGGESTION

5.1 Conclusion

This research presents the successful development of the economical equipment for Bridgman crystal growing process and simple growing process of commercial CsI:Tl scintillator of 22 mm in diameter for gamma spectroscopy. In development of $\text{LaCl}_3:\text{Ce}$, the high resolution crystal, and ternary compound of $\text{Ba}_2\text{CsI}_5:\text{Tl}$, even though the experimental results reveal imperfection in large crystal size, they provide numerous details for future improvements and the trend to success. The experimental results can be concluded as follows:

5.1.1 Furnace development

The economical conventional furnace and moving-temperature gradient furnace for Bridgman-Stockbarger crystal growing method were developed using parts and components locally available. The furnace temperature can be precisely controlled in the range of 400°C to 1200°C at an electrical power consumption of 4 kW with high thermal stability. The largest crystal size of 25 mm in diameter and 70 mm in length could be grown. The temperature recording system is also attached and recorded data can be transferred to a personal computer. Comparison of grown crystals from both furnaces revealed no significant crystal quality difference due to the technical design concept on vibration elimination. Furnace system controls have special features as follows:

a) **Conventional Bridgman Furnace.** The simple top loading crucible vertical translation was moved by a linear screw drive mechanic coupling to a bipolar driving stepping motor with micro-stepping control. The system was interfaced with a PIC microcontroller for a wide range translation of the growth rate between 0.1 to 5 mm/h. New design of a crucible translation with direct coupling linear driving mechanic in conventional furnace eliminates a gear box system that results in a much reduced vibration.

b) **Moving-Temperature-Gradient furnace.** This technique helps to eliminate a driving mechanism and reduces subtle vibration, which could adversely affect crystal quality, because the charge crucible and the furnace are made stationary during the growth process. The temperature gradient drift rate of 0.1 to 500 °C/hr and the temperature gradient in the range of 5 to 50 °C/cm can be set for growth rate control. These conditions can be easily programmed on differential temperature ramp up of upper and lower furnace elements at the temperature controller. The system can also be set for a temperature ramp down rate for cooling down the grown crystal.

5.1.2 Charge material preparation

In our research, two types of quartz crucible, ampoule and open-ended crucible with refractory tube, were designed for hygroscopic and non- hygroscopic materials preparation, respectively. It was found that the advantages of open-ended crucible with refractory tube type are as follows:

a) In the open-ended quartz crucible, if the grown crystal is loose and can easily be removed from the crucible, the quartz crucible can be reused after cleaning by dilute acid solution followed by ultrasonic cleaning. This helps save crucible preparation time and cost.

b) Due to the absence of vibration in the moving-temperature-gradient growing process, the refractory tube can be directly used as a crucible. Therefore, the 3-core, multi-crucible system was developed and applied in this research. In the multi-crucible system, 3 grown crystals under the same growing conditions were obtained simultaneously in each crystal growth process that avails to save experimental time and power consumption.

5.1.3 Crystals growing

The CsI:Tl was successfully grown in a laboratory-scale furnace with size of $\text{Ø}22 \text{ mm} \times 22 \text{ mm}$ in the moving-temperature-gradient furnace using the open-ended crucible loaded with the refractory tube. The performance in gamma spectroscopy tested with 662 keV on energy resolution, intrinsic peak efficiency and peak to Compton ratio were found to be 7.53%, 10.35% and 4.58:1, respectively. This is compatible to the

commercial high-grade NaI:Tl. The binary compound with cerium doped of $\text{LaCl}_3\text{:Ce}$ and the ternary compound with thallium doped of $\text{Ba}_2\text{CsI}_5\text{:Tl}$ crystal growing process need more improvement in the charge material preparation process and the growing condition to be completely grown without cracks. Conclusions of all experimental results are described as follows:

a) In CsI:Tl crystal growing, charge materials were prepared from 99.9% pure CsI mixed with 99.999% pure TlI dopant. The crystals were grown by the moving-temperature-gradient furnace using the open-ended crucible loaded with the refractory tube at the crystal growth rate of 1 mm/hr from the temperature gradient of 25.5 °C/cm and the temperature gradient drift rate of 2.5 °C/hr. The grown crystals coupling with Hamamatsu model 52154-02 PMT or Hamamatsu model S3590-8 PIN Photodiode as scintillation detector were tested in radiation detection performance using gamma radiation sources of energy 122 keV, 662 keV and 1.33 MeV from Co-57 , Cs-137 and Co-60 , respectively. Enhancement of scintillated photon with the white Teflon tape reflector and crystal optical quality were also achieved. Summary of tested results is shown in Table 5.1.

The highest energy resolution of 7.19% and 7.53% was achieved with Tl dopant concentration of 0.3570 wt% and 0.3602 wt%, respectively, with grown crystals of 10 mm and 22 mm diameter tested with 662 keV Cs-137 source. The intrinsic peak efficiencies were obtained at 2.50% and 10.35% with peak to Compton ratio at 2.28:1 and 4.58:1, respectively. The average light transmittance of crystals of about 80% was achieved.

b) In $\text{LaCl}_3\text{:Ce}$ crystal growing, hygroscopic charge materials were prepared from 99.9% pure LaCl_3 and 99.9% pure CeCl_3 in the glove box for moisture reduction. The crystals were grown by both conventional Bridgman and moving-temperature-gradient furnaces using ampoule and open-ended crucible loaded with refractory tube at the crystal growth rate of 1 mm/hr from the temperature gradient of 25 °C/cm and the temperature gradient drift rate of 2.5 °C/hr at crystal sizes of 10, 14 and 22 mm diameter with 30, 50 and 70 mm length, respectively. All crystals could not completely grow and white solid substances appeared with cracked crystal pieces in the growth crystal. The crystal surface was rather harder than that of CsI:Tl . The small

cracked clear crystal with 18.91 wt% CeCl₃ dopant was cut and polished to a size of 5 × 5 × 1 mm³ in the glove box. The energy resolution was tested to be 7.61%. Summary of tested results is shown in Table. 5.1

c) In Ba₂CsI₅:Tl crystals, they were grown from 98% pure BaI₂, 99.9% pure CsI and 99.999% pure TlI dopant. The crystals were grown by the moving-temperature-gradient furnace using the multi- crucible technique at the crystal growth rate of 1 mm/hr from the temperature gradient of 25 °C/cm and the temperature gradient drift rate of 2.5 °C/hr at the crystal size of 10 mm diameter and 30 mm length. The growth crystals were clear but cracked into small pieces and were hygroscopic. The small piece of cracked and clear crystal with size of 6 × 3 × 1 mm³ with 1.0050 wt% TlI dopant yielded the energy resolution of 12.53%. Summary of tested results is shown in Table 5.1.

Table 5.1 Summary on tested results of grown scintillation crystals

Scintillator	Size (mm ³)	Dopant concentration (wt%)	Energy resolution (%)	Intrinsic peak efficiency (%)	Peak to Compton ratio	Visible light transmittance at λ 400 - 700 nm (%)
CsI:Tl	Ø10 × 10	0.3570	7.19	2.50	2.28:1	80
	Ø10 × 10 ^a	0.3570	8.60	2.50	1.90:1	80
CsI:Tl	Ø22 × 22	0.3602	7.53	10.35	4.58:1	74
LaCl ₃ :Ce	5 × 5 × 1	18.91	7.61	-	-	-
Ba ₂ CsI ₅ :Tl	6 × 3 × 1	1.0050	12.53	-	-	-
Na:Tl ^b	Ø25 × 25	-	10.76	8.43	2.72:1	-

^a Coupling with PIN photodiode

^b Commercial scintillator from Bicron model 1M1/2P

5.2 Discussion

From the conclusions, there are both complete and incomplete crystal growth experiments. Analysis of incomplete crystals provides different methods to improve the charge preparation and crystal growing process as follows:

a) Due to the crystal properties of CsI:Tl which has no cleavage plane, is non hygroscopic and exhibits a simple cubic crystal structure, they was easy to grow at

large size for high quality scintillator. To improve the process, compound purity should be optimized with respect to the radiation detection performance that affects the crystal cost. In scintillation detector assembly, for compact size, the crystal emission wavelength is matched to a PIN photodiode. However, recently the cost of a large area photodiode is still expensive compared to a PMT with equivalent photocathode area. The other issue is noise interference from diode junction at low energy of gamma spectrum.

b) The $\text{LaCl}_3:\text{Ce}$ is a high performance binary compound scintillator, just commercially announced from a few companies with the energy resolution of 3.4% at 662 keV. However, the hygroscopic nature of LaCl_3 or CeCl_3 is a major problem in charge preparation. The moisture contained in this compound can hydrolysis to LaOCl or CeOCl impurity, which exhibits a high melting point in a crystal and leads to crystal cracking into small pieces. The chemical reaction of LaCl_3 or CeCl_3 with oxygen and moisture can also form some compounds of La_2O_3 and CeO_2 , which complicated crystal formation and resulted in thermal stress due to thermal expansion. There are some discussions and comments in literature [39] for moisture and oxygen reduction processes.

c) From literature [31], the ternary compound of $\text{Ba}_2\text{CsI}_5:\text{Eu}$ was reported as a new high density and high energy resolution scintillator. The results were very promising considering that the crystal quality can still be improved and optimized. This leads our research to enhance the crystal density by doing with Tl to become $\text{Ba}_2\text{CsI}_5:\text{Tl}$. The scintillated photon light yield is expected to increase due to increased gamma energy absorption coefficient and trapped center formed in the crystal system. From experimental results, it was hard to grow the ternary crystal without cracks by the simple melt-mixing process because of the incomplete chemical reaction from two binary compounds to the ternary compound during the melt period. Another possible reason is the thermal stress effect.

5.3 Suggestion

In charge preparation, moisture absorption into hygroscopic compounds is a serious problem as the hydrolysis reaction can change the compound into an impurity in a crystal. Thermal dehydration cannot remove moisture. An inert gas glove box should be used to prevent moisture and to remove oxygen. A glove box should be prepared to remove oxygen and moisture by copper catalyst such as BASF R3-15 and molecular sieve such as type 13X [39].

For the ternary compound grown from two binary compounds in powder form using solid-solid reaction, the compound should be mixed in a ball mill for homogeneity, and then pressed into a dense pellet before loading into a crucible for complete chemical reaction from two binary compounds to the ternary compound before the melt period. This method should be grown with large crystal size. To avoid crystal cracking, slow growth rate and annealing during the stepped cool down to prevent thermal stress need to be applied.

As rare earth halide is expensive, preparation of rare earth halide is possible from the reaction of rare earth oxide with hydrochloric acid and ammonium chloride. This preparation method can reduce the cost of compounds, which makes scintillation crystal growing from rare earth halide possible.

From this research, even though crystals from some new compounds were not completely grown and cracks formed, the small size crystals can be assembled into an array of scintillation detector and applied into radiation imaging. However, in using hygroscopic crystals, it is necessary to well-encapsulate with a photosensitive device.

ศูนย์วิทยทรัพยากร

จุฬาลงกรณ์มหาวิทยาลัย

REFERENCES

- [1] Eijk, C.W.E. Inorganic-scintillator development. Nuclear Instruments and Methods in Physics Research A 460 (2001) : 1-14.
- [2] Knoll, G.F. Radiation detection and measurement. 3rd New York : John Wiley & Sons, Inc., 1999.
- [3] Vij, D.R. Thermoluminescent Materials. New Jersey : PTR Prentice Hall, 1993.
- [4] Derenzo, S.E., Weber, M.J., Courchesne, E.B., and Klintonberg, M.K. The quest for the ideal inorganic scintillator. Nuclear Instruments and Methods in Physics Research A 505 (2003) : 111-117.
- [5] Loef, E.V.D. Halide Scintillators. Doctoral Thesis, Radiation Technology Group, Interfaculty Reactor Institute, Delft University of Technology, 2003.
- [6] Dorenbos, P., Haas, J.T.M., Visser, R., Eijk, C.W.E., and Hollander, R.W. Absolute light yield measurements on BaF₂ crystals and the quantum efficiency of several photomultiplier tubes. IEEE Transactions on Nuclear Science 40 (1993) : 424-430.
- [7] Kapoor, S.S., and Ramamurthy, V.S. Nuclear radiation Detections. 1st New Delhi : New age international (P) Ltd., 1986.
- [8] Hamamatsu. Photomultiplier tubes. Hamamatsu Photonics K.K., Electron Tube Center, 1998.
- [9] Electronic Industries Association. Relative spectral response data for photosensitive devices ("S" curves). JEDEC Publication 50 (1964).
- [10] Held., G. Introduction to Light Emitting Diode Technology and Applications. CRC Press, 2008.
- [11] Hamamatsu. Si Photodiode. Hamamatsu Photonics K.K., Solid state division, 2002.
- [12] Wang, L.C., Liu, Y.C., Yu, W.C., Roux, B., Lyubimova, T.P., and Lan, C.W. Segregation control of vertical Bridgman growth of Ga-doped germanium crystals by accelerated crucible rotation: ACRT versus angular vibration. Journal of Crystal Growth 311 (2009) : 684-687.
- [13] Saucedo, E., Rudolph, P., and Dieguez, E. Modified Bridgman growth of CdTe crystals. Journal of Crystal Growth 310 (2008) : 2067-2071.

- [14] Zawilski, K.T., Custodio, M.C.C., Robert, C.D., and Feigelson, R.S. Control of growth interface shape using vibroconvective stirring applied to vertical Bridgman growth. Journal of Crystal Growth 282 (2005) : 236-250.
- [15] Kokh, K.A., Nenashev, B.G., Kokh, A.E., and Shvedenkov, G.Y. Application of a rotating heat field in Bridgman–Stockbarger crystal growth. Journal of Crystal Growth 275 (2005) : e2129-e2134.
- [16] Xu, J., Fan, S., and Lu, B. Growth of $\varnothing 4''$ $\text{Li}_2\text{B}_4\text{O}_7$ single crystals by multi-crucible Bridgman method. Journal of Crystal Growth 264 (2004) : 260-265.
- [17] Szeles, C., Cameron, S.E., Ndap, J.O., and Chalmers, W.C. Advances in the crystal growth of semi-insulating CdZnTe for radiation detector applications. IEEE Transactions on Nuclear Science 49 (2002) : 2535-2540.
- [18] Ren, G., William, C., Chen, X., Pei, Y., Li, H., and Xu, H. Dehydration and oxidation in the preparation of Ce-doped LaCl_3 scintillation crystals. Journal of Alloys and Compounds 467 (2009) : 120–123.
- [19] Chen, H., Yang, P., Zhou, C., and Jiang, C. Bridgman growth of $\text{LaCl}_3:\text{Ce}^{3+}$ crystal in non-vacuum atmosphere. Journal of Alloys and Compounds 449 (2008) : 172–175.
- [20] Meyer, G., and Ax, P. An analysis of the ammonium chloride route to anhydrous rare-earth metal chlorides. Materials Research Bulletin 17 (1982) : 1447-1455.
- [21] Meyer, G., Dötsch S., and Staffel, T. The ammonium-bromide route to anhydrous rare earth bromides MBr_3 . Journal of the Less-Common Metal 127 (1986) : 155-160.
- [22] Kim, H.S., Ha, J.H., Park, S.H., Cho, S.Y., and Kim, Y.K. Fabrication and performance characteristics of a CsI(Tl)/PIN diode radiation sensor for industrial applications. Applied Radiation and Isotopes 67 (2009) : 1463-1465.
- [23] Balamurugan, N., et al. Growth and characterization of undoped and thallium doped cesium iodide single crystals. Journal of Crystal Growth 286 (2006) : 294-299.

- [24] Ren, G., Chen, X., Lu, S., Li, Z., Xue, X., and Shen, D. Non-uniformity of light output in large-sized CsI(Tl) crystals grown by non-vacuum Bridgman method. Nuclear Instruments and Methods in Physics Research A 564 (2006) : 364-369.
- [25] Guillot-Noël, O., Haas, J.T.M., Dorenbos, P., Eijk, C.W.E., Krämer, K., and Güdel, H.U. Optical and scintillation properties of cerium-doped LaCl₃, LuBr₃ and LuCl₃. Journal of Luminescence 85 (1999) : 21-35.
- [26] Andriessen, J., et al. Experimental and theoretical study of the spectroscopic properties of Ce³⁺ doped LaCl₃ single crystals. Optics Communications 178 (2000) : 355–363.
- [27] Loef, E.V.D., Dorenbos, P., Eijk, C.W.E., Krämer, K., and Güdel, H. U. Scintillation properties of LaCl₃:Ce³⁺ crystals: fast, efficient, and high-energy resolution scintillators. IEEE Transactions on Nuclear Science 48 (2001) : 341-345.
- [28] Alliera, C.P., et al. Readout of a LaCl₃(Ce³⁺) scintillation crystal with a large area avalanche photodiode. Nuclear Instruments and Methods in Physics Research A 485 (2002) : 547-550.
- [29] Glodo, J., Shah, K.S., Klugerman, M., Wong, P., and Higgins, B. Thermoluminescence of LaBr₃:Ce and LaCl₃:Ce crystals. Nuclear Instruments and Methods in Physics Research A 537 (2005) : 93-96.
- [30] Bourret-Courchesne, E.D., Bizarri, G., Hanrahan, S.M., Gundiah, G., Yan, Z., and Derenzo, S.E. BaBr:Eu²⁺, a new bright scintillator. Nuclear Instruments and Methods in Physics Research A 613 (2010) : 95-97.
- [31] Bourret-Courchesne, E.D., et al. Eu²⁺-doped Ba₂CsI₅, a new high-performance scintillator. Nuclear Instruments and Methods in Physics Research A 613 (2009) : 138-142.
- [32] Holl, I., Lorenz, E., and Mageras, G. A Measurement of the light yield of common inorganic scintillators. IEEE Transactions on Nuclear Science 35 (1988) : 105-109.
- [33] Moszyński, M., Kapusta, M., Mayhugh, M., Wolski, D., and Flyckt, S.O. Absolute light output of scintillators. IEEE Transactions on Nuclear Science 44 (1997) : 1052-1061.

- [34] Haas, J.T. M., and Dorenbos, P. Advances in yield calibration of scintillators. IEEE Transactions on Nuclear Science 55 (2008) : 1086-1092.
- [35] Sysoeva, E., Tarasov, V., and Zelenskaya, O. Comparison of the methods for determination of scintillation light yield. Nuclear Instruments and Methods in Physics Research A 486 (2002) : 67-73.
- [36] Manit Jitpukdee. Development a simple process for growing CsI(Tl) crystal. Master Thesis, Department of Nuclear Technology, Faculty of Engineering, Chulalongkorn University, 2003.
- [37] MacMillan, J. P., Park, J. W., Gerstenberg, R., Wagner, H., and Köhler, K., and Wallbrecht, P. Strontium and Strontium Compounds in Ullmann's Encyclopedia of Industrial Chemistry. Wiley-VCH : Weinheim, 2005.
- [38] Eiji, S. Recent measurements on scintillator-photodetector systems. IEEE Transactions on Nuclear Science 34 (1987) : 418-422.
- [39] Higgins, W.M., et al. Bridgman growth of LaBr₃:Ce and LaCl₃:Ce crystals for high-resolution gamma-ray spectrometers. Journal of Crystal Growth 287 (2006) : 239-242.



Appendices

ศูนย์วิทยทรัพยากร
จุฬาลงกรณ์มหาวิทยาลัย

Appendix A Microstepping drive specification

IMS™

INTELLIGENT MOTION SYSTEMS, INC.

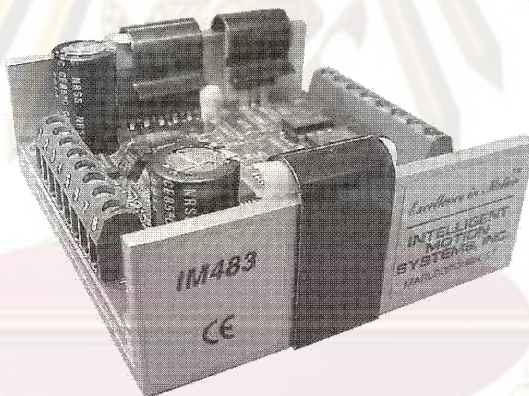
Excellence in Motion™

IM483

HIGH PERFORMANCE MICROSTEPPING DRIVE

STANDARD DRIVER
CONNECTOR OPTIONS
DUAL STEP CLOCK INPUT VERSION
COOLING SOLUTIONS
ACCESSORIES

OPERATING INSTRUCTIONS



CE

370 N. MAIN ST., PO BOX 457, MARLBOROUGH, CT 06447

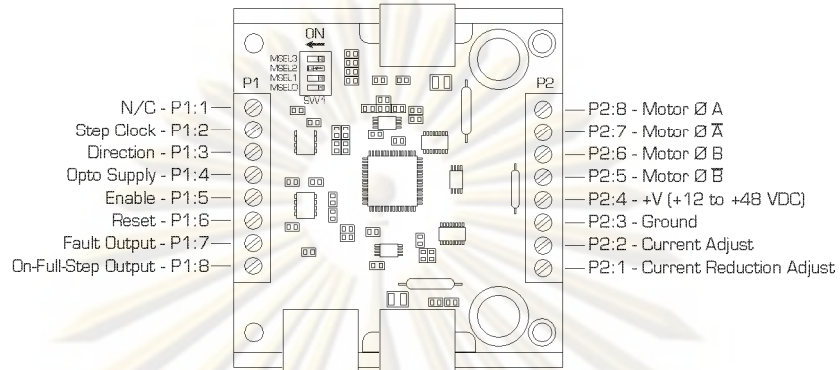
PH. (860) 295-6102, FAX (860) 295-6107

Internet: <http://www.imshome.com>, E-Mail: info@imshome.com

ศูนย์วิจัยทรัพยากร

จุฬาลงกรณ์มหาวิทยาลัย

Pin Assignment and Description



Connector P1

IM483 Connector P1 Configuration		
PIN #	FUNCTION	DETAILS
1	N/C	No connection.
2	Step Clock Input	A positive going edge on this input advances the motor one increment. The size of the increment is dependent upon the settings of the resolution select switch SW1.
3	Direction Input	This input is used to change the direction of the motor. Physical direction also depends upon the connection of the motor windings.
4	Opto Supply	This +5VDC input is used to supply power to the isolated logic inputs. A higher voltage may be used, but care must be taken to limit the current through the opto-coupler.
5	Enable/Disable Input	This input is used to enable/disable the output section of the driver. When in a Logic HIGH state (open), the outputs are enabled. However, this input does not inhibit the step clock, therefore, the outputs will update by the number of clock pulses (if any) applied to the driver while it was disabled.
6	Reset Input	When LOW, this input will reset the driver (phase outputs will disable). When released, the driver will be at its initial state (Phase A OFF, Phase B ON).
7	Fault Output	This output indicates that a short circuit condition has occurred. This output is active LOW.
8	On-Full-Step Output	This open collector output indicates when the driver is positioned at full step. This output can be used to count the number of full steps the motor has moved, regardless of the number of microsteps in between. This output is active LOW.

Connector P2

IM483 Connector P2 Configuration		
PIN #	FUNCTION	DETAILS
1	Current Reduction Adjust	Phase Current Reduction Adjustment Input. A resistor connected between this pin and pin 2 will proportionately reduce the current in both motor windings approximately .5 seconds after the last positive edge of the step clock input. The amount of current reduced will depend upon the value of the resistor used.
2	Current Adjustment	Phase Current Adjustment. A resistor is connected between this pin and P2:3 (GND) to adjust the maximum phase current in the motor. A resistor MUST be connected to this input or the IM483 WILL latch into fault.
3	GND	Power Ground. The ground, or return, of the power supply is connected here.
4	+V	Motor Supply Voltage. +12 to +48VDC.
5	Phase B̄	\overline{OB} of the stepping motor.
6	Phase B	OB of the stepping motor.
7	Phase Ā	\overline{OA} of the stepping motor.
8	Phase A	OA of the stepping motor.

Resolution		Microstep Select DIP Switch Settings			
Microsteps/Step	Steps/Rev	SW 1:1 (MSEL0)	SW 1:2 (MSEL1)	SW 1:3 (MSEL2)	SW 1:4 (MSEL3)
in r Microstep Resolution Settings (1.8° Motor)					
2	400	ON	ON	ON	ON
4	800	OFF	ON	ON	ON
8	1,600	ON	OFF	ON	ON
16	3,200	OFF	OFF	ON	ON
32	6,400	ON	ON	OFF	ON
64	12,800	OFF	ON	OFF	ON
128	25,600	ON	OFF	OFF	ON
256	51,200	OFF	OFF	OFF	ON

Decimal Microstep Resolution Settings (1.8° Motor)					
Microsteps/Step	Steps/Rev	SW 1:1 (MSEL0)	SW 1:2 (MSEL1)	SW 1:3 (MSEL2)	SW 1:4 (MSEL3)
5	1,000	ON	ON	ON	OFF
10	2,000	OFF	ON	ON	OFF
25	5,000	ON	OFF	ON	OFF
50	10,000	OFF	OFF	ON	OFF
125	25,000	ON	ON	OFF	OFF
250	50,000	OFF	ON	OFF	OFF

Invalid Resolution Settings : May Cause Erratic Operation					
Microsteps/Step	Steps/Rev	SW 1:1 (MSEL0)	SW 1:2 (MSEL1)	SW 1:3 (MSEL2)	SW 1:4 (MSEL3)
		ON	OFF	OFF	OFF
		OFF	OFF	OFF	OFF

Appendix B.1 PMT specification

HAMAMATSU**PHOTOMULTIPLIER TUBES
R2154-02****For Scintillation Counting and High Energy Physics
51 mm (2 Inch) Diameter, Fast Time Response,
Bialkali Photocathode, 10-stage, Head-on Type****GENERAL**

Parameter		Description/Value	Unit
Spectral Response		300 to 650	nm
Wavelength of Maximum Response		420	nm
Photocathode	Material	Bialkali	—
	Minimum Effective Area	φ46	mm
Window Material		Borosilicate glass	—
Dynode	Structure	Linear focused	—
	Number of Stages	10	—
Base		14-pin base JEDEC No. B14-38	—
Operating Ambient Temperature		-30 to +50	°C
Storage Temperature		-30 to +50	°C
Suitable Socket		E678-14W (Sold Separately)	—

MAXIMUM RATINGS (Absolute Maximum Values)

Parameter		Value	Unit
Supply Voltage	Between Anode and Cathode	1600	V
	Between Anode and Last Dynode	350	V
Average Anode Current		0.1	mA

CHARACTERISTICS (at 25 °C)

Parameter		Min.	Typ.	Max.	Unit
Cathode Sensitivity	Luminous (2856 K)	60	90	—	μA/lm
	Blue Sensitivity Index (CS 5-58)	—	10.5	—	—
	Radiant at 420 nm	—	85	—	mA/W
	Quantum Efficiency at 420 nm	—	26	—	%
Anode Sensitivity	Luminous (2856 K)	20	90	—	A/W
	Radiant at 420 nm	—	8.5×10^4	—	A/W
Gain		—	1.0×10^6	—	—
Anode Dark Current (after 30 minutes storage in darkness)		—	5	20	nA
Time Response	Anode Pulse Rise Time	—	3.4	—	ns
	Transit Time Spread (FWHM)	—	3.6	—	ns
Pulse Linearity (at ± 2 % Deviation)*		—	150	—	mA

NOTE: Anode characteristics are measured with the voltage distribution ratio "A" except for Pulse Linearity.

* Measured with the special voltage distribution ratio "B".

VOLTAGE DISTRIBUTION RATIO "A"

Electrodes	K	Dy1	Dy2	Dy3	Dy4	Dy5	Dy6	Dy7	Dy8	Dy9	Dy10	P
Ratio	2	1	1	1	1	1	1	1	1	1	1	1

Supply Voltage: 1250 V, K: Cathode, Dy: Dynode, P: Anode

SPECIAL VOLTAGE DISTRIBUTION RATIO "B" FOR HIGH PULSE LINEARITY

Electrodes	K	Dy1	Dy2	Dy3	Dy4	Dy5	Dy6	Dy7	Dy8	Dy9	Dy10	P
Ratio	2	1	1	1	1	1	1.2	1.5	2.2	3.6	3	
Capacitors(μF)	—	—	—	—	—	—	0.01	0.01	0.01	0.01	0.02	

Supply Voltage: 1500 V, K: Cathode, Dy: Dynode, P: Anode

Subject to local technical requirements and regulations, availability of products included in this promotional material may vary. Please consult with our sales office.
Information furnished by HAMAMATSU is believed to be reliable. However, no responsibility is assumed for possible inaccuracies or omissions. Specifications are subject to change without notice. No patent rights are granted to any of the circuits described herein. ©2006 Hamamatsu Photonics K.K.

PHOTOMULTIPLIER TUBE R2154-02

Figure 1: Typical Spectral Response

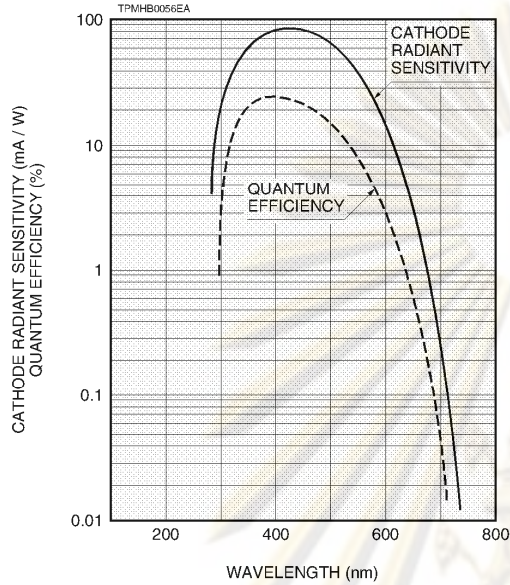


Figure 2: Typical Gain Characteristics

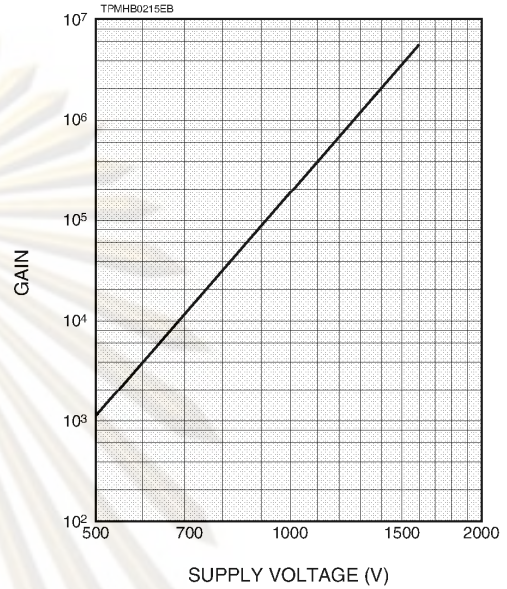
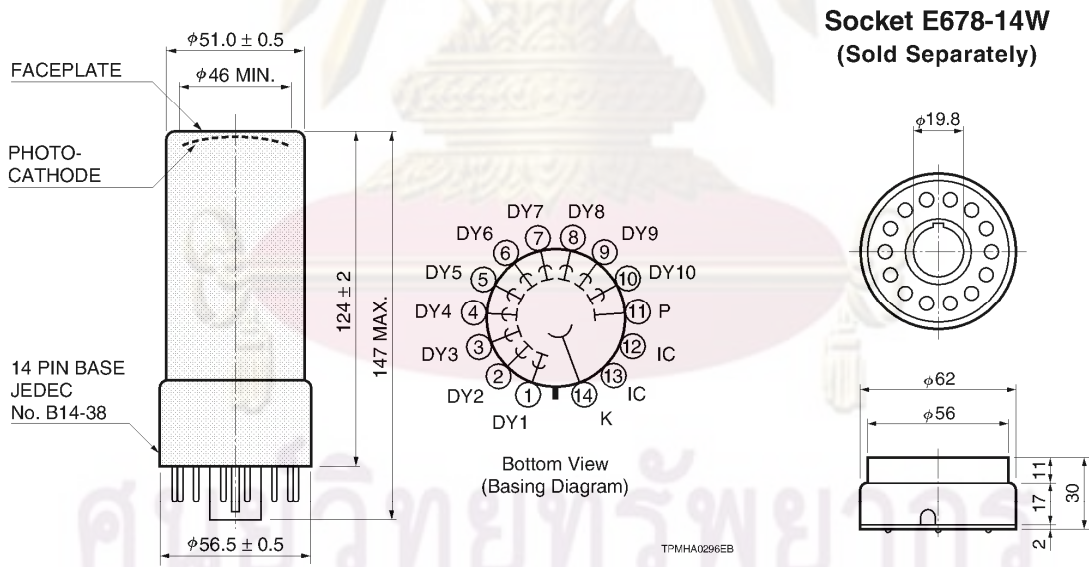


Figure 3: Dimensional Outline and Basing Diagram (Unit: mm)



HAMAMATSU

WEB SITE www.hamamatsu.com

HAMAMATSU PHOTONICS K.K., Electron Tube Division

314-5, Shimokanzo, Iwata City, Shizuoka Pref., 438-0193, Japan, Telephone: (81)539/62-5248, Fax: (81)539/62-2205

U.S.A.: Hamamatsu Corporation, 360 Foothill Road, P. O. Box 6910, Bridgewater, N.J. 08807-0910, U.S.A., Telephone: (1)908-231-0960, Fax: (1)908-231-1218 E-mail: usa@hamamatsu.com

Germany: Hamamatsu Photonics Deutschland GmbH, Arzbergerstr. 10, D-82211 Herrsching am Ammersee, Germany, Telephone: (49)8152-375-0, Fax: (49)8152-2658 E-mail: info@hamamatsu.de

France: Hamamatsu Photonics France S.A.R.L., 19, Rue du Saule Trapu, Parc du Moulin de Massy, 91882 Massy Cedex, France, Telephone: (33)1 69 53 71 00, Fax: (33)1 69 53 71 10 E-mail: infos@hamamatsu.fr

United Kingdom: Hamamatsu Photonics UK Limited, 2 Howard Court, 10 Tewin Road Welwyn Garden City Hertfordshire AL7 1BW, United Kingdom, Telephone: 44-(0)1707-294888, Fax: 44(0)1707-325777 E-mail: info@hamamatsu.co.uk

North Europe: Hamamatsu Photonics Norden AB, Smidesvägen 12, SE-171-41 SOLNA, Sweden, Telephone: (46)8-509-031-00, Fax: (46)8-509-031-01 E-mail: info@hamamatsu.se

Italy: Hamamatsu Photonics Italia: S.R.L., Strada della Moia, 1/E, 20020 Arese, (Milano), Italy, Telephone: (39)02-935 81 733, Fax: (39)02-935 81 741 E-mail: info@hamamatsu.it

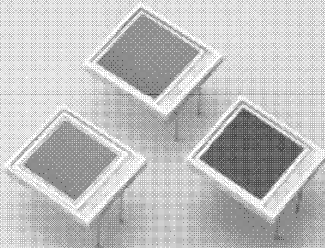
TPMH1089E05
JUL. 2006 IP

Appendix B.2 PIN photodiode specification

PHOTODIODE

Si PIN photodiode S3590 series

Large area sensors for scintillation detection



Features

- Higher sensitivity and low dark current than conventional type
- Sensitivity matching with BGO and CsI (TI) scintillators
- High quantum efficiency: QE=85 % ($\lambda=540$ nm)
- Low capacitance
- High-speed response
- High stability
- Good energy resolution

Applications

- Scintillation detectors
- Calorimeters
- Hodoscopes
- TOF counters
- Air shower counters
- Particle detectors, etc.

■ General ratings / Absolute maximum ratings

Type No.	Window material	Active area (mm)	Absolute maximum ratings			
			Reverse voltage VR Max.	Power dissipation P (mW)	Operating temperature T _{opr} (°C)	Storage temperature T _{stg} (°C)
S3590-01	Epoxy resin	10 × 10	50	100	-20 to +60	-20 to +80
S3590-02	Window-less					
S3590-05	Epoxy resin	9 × 9	150			
S3590-06	Window-less					
S3590-08	Epoxy resin	10 × 10	100			
S3590-09	Window-less					

■ Electrical and optical characteristics (Typ. Ta=25 °C, unless otherwise noted)

Type No.	Spectral response range λ (nm)	Peak sensitivity wavelength λ_p (nm)	Photo sensitivity S				Short circuit current I _{sc} 100 lx (μ A)	Dark current I _D		Temp. coefficient of I _D T _{CI_D} (times/°C)	Cut-off Frequency f _c (MHz)	Terminal capacitance C _t f=1MHz (pF)	NEP V _R =70 V (W/Hz ^{1/2})
			$\lambda=\lambda_p$ (A/W)	LSO 420 nm (A/W)	BGO 480 nm (A/W)	CsI(Tl) 540 nm (A/W)		Typ.	Max.				
S3590-01	320 to 1060	920	0.58	0.19	0.26	0.31	80	1.5 *1	5 *1	1.12	35 *1	75 *1	3.9 × 10 ⁻¹⁴
S3590-02			0.62	0.23	0.32	0.39					20 *2	25 *2	8.4 × 10 ⁻¹⁴
S3590-05	320 to 1120	980	0.62	0.19	0.25	0.30	77	8 *2	30 *2	1.12	40 *3	40 *3	3.8 × 10 ⁻¹⁴
S3590-06			0.64	0.23	0.32	0.39							
S3590-08	320 to 1100	960	0.66	0.20	0.30	0.36	100	2 *3	6 *3				
S3590-09			0.66	0.22	0.33	0.41							

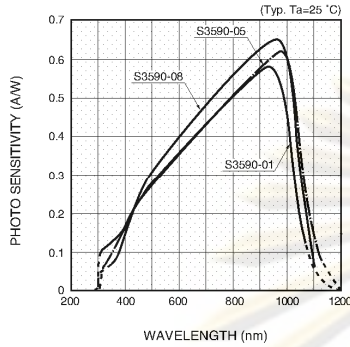
*1: V_R=30 V*2: V_R=100 V*3: V_R=70 V

SOLID STATE DIVISION

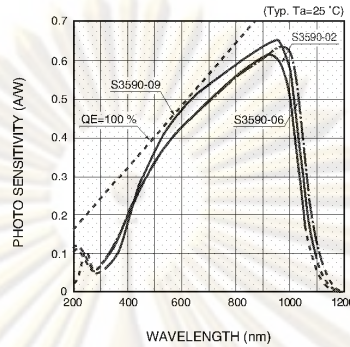
HAMAMATSU

Si PIN photodiode S3590 series

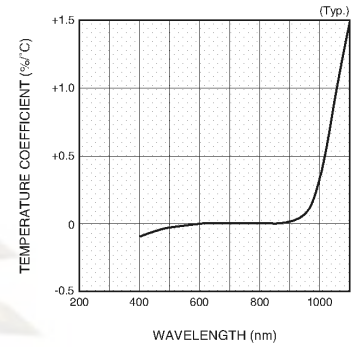
■ Spectral response



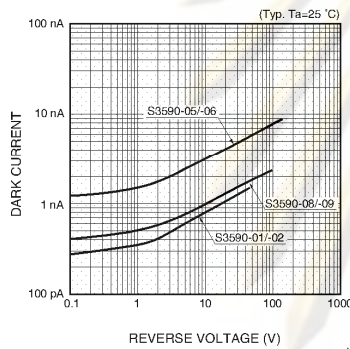
■ Spectral response (without window)



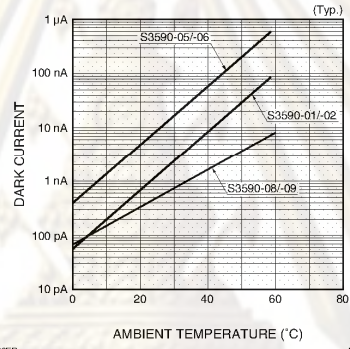
■ Photo sensitivity temperature characteristic



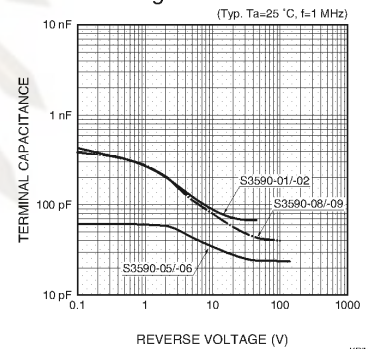
■ Dark current vs. reverse voltage



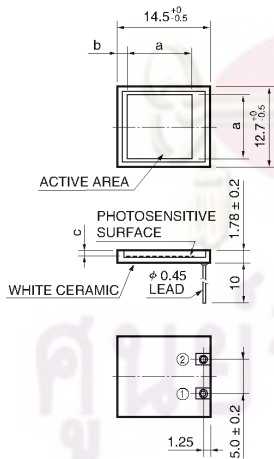
■ Dark current vs. ambient temperature



■ Terminal capacitance vs. reverse voltage



■ Dimensional outline (unit: mm)



The coating resin may extend a maximum of 0.1 mm beyond the upper surface of the package.

	-01	-05	-08
a	10.0	9.0	10.0
b	1.4	1.9	1.4
c	0.8	0.5	0.7

KPINA0014EE

HAMAMATSU

Information furnished by HAMAMATSU is believed to be reliable. However, no responsibility is assumed for possible inaccuracies or omissions. Specifications are subject to change without notice. No patent rights are granted to any of the circuits described herein. ©2003 Hamamatsu Photonics K.K.

HAMAMATSU PHOTONICS K.K., Solid State Division

1126-1 Ichino-cho, Hamamatsu City, 435-8558 Japan, Telephone: (81) 053-434-3311, Fax: (81) 053-434-5184, <http://www.hamamatsu.com>

U.S.A.: Hamamatsu Corporation: 360 Foothill Road, P.O. Box 6910, Bridgewater, N.J. 08807-0910, U.S.A., Telephone: (1) 908-231-0960, Fax: (1) 908-231-1218

Germany: Hamamatsu Photonics Deutschland GmbH: Arzbergerstr. 10, D-82211 Herrsching am Ammersee, Germany, Telephone: (49) 08152-3750, Fax: (49) 08152-2658

France: Hamamatsu Photonics France S.A.R.L.: 8, Rue du Saule Trapu, Parc du Moulin de Massy, 91882 Massy Cedex, France, Telephone: 33-(1) 69 53 71 00, Fax: 33-(1) 69 53 71 10

United Kingdom: Hamamatsu Photonics UK Limited: 2 Howard Court, 10 Tewin Road, Welwyn Garden City, Hertfordshire AL7 1BW, United Kingdom, Telephone: (44) 1707-294888, Fax: (44) 1707-325777

North Europe: Hamamatsu Photonics Norden AB: Smidesvägen 12, SE-171 41 Solna, Sweden, Telephone: (46) 8-509-031-00, Fax: (46) 8-509-031-01

Italy: Hamamatsu Photonics Italia S.R.L.: Strada della Moia, 1/E, 20020 Arese, (Milano), Italy, Telephone: (39) 02-935-81-733, Fax: (39) 02-935-81-741

Appendix C Grown crystal properties

Properties	CsI:Tl	LaCl ₃ :Ce	Ba ₂ CsI ₅ :Tl
Maximum emission wave length λ_{\max} (nm)	540	350	-
Light yield (photons per MeV)	52,000	50,000	-
Density (g/cm ³)	4.51	3.84	4.8
Melting point (°C)	621	860	575±25
Crystal structure	Cubic	Hexagonal	Monoclinic
Space group	Pm3m	P6 ₃ /m	P2 ₁ /C
Cleavage plane	No	Yes	-
Hydroscopic	slightly	high	high
Refractive index	1.79	1.90	-

ศูนย์วิทยทรัพยากร
จุฬาลงกรณ์มหาวิทยาลัย

Appendix D Commercial NaI:Tl spectroscopy

Amptek Advance Product

Gamma Ray & X-Ray Spectroscopy System Hand-Held, High Efficiency NaI:Tl Detector

Energy resolution for the standard
76 x 76 mm³ NaI:Tl crystal is
typically 6.9% at 662 keV and 4.7%
at 1.33 MeV.

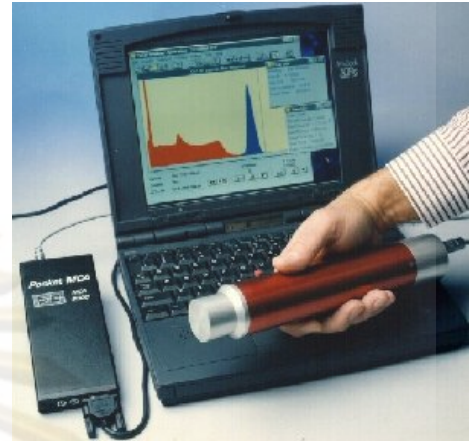


Figure 1. Gamma-8000
shown with a special order
30 x 30 mm NaI:Tl probe

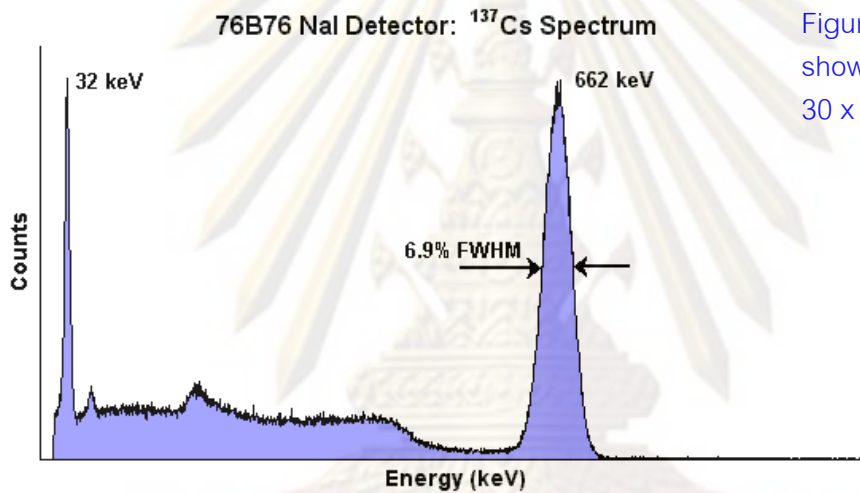


Figure 2. Cs-137 spectrum

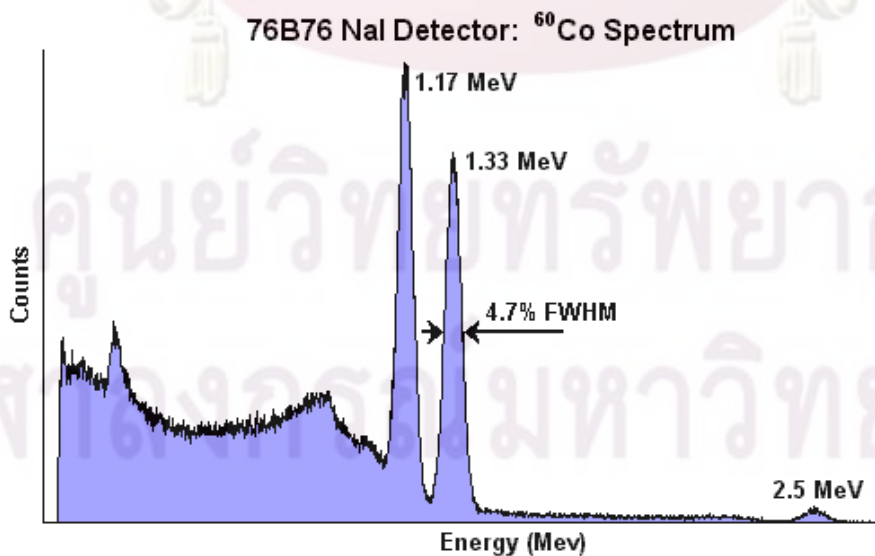


Figure 3. Co-60 spectrum

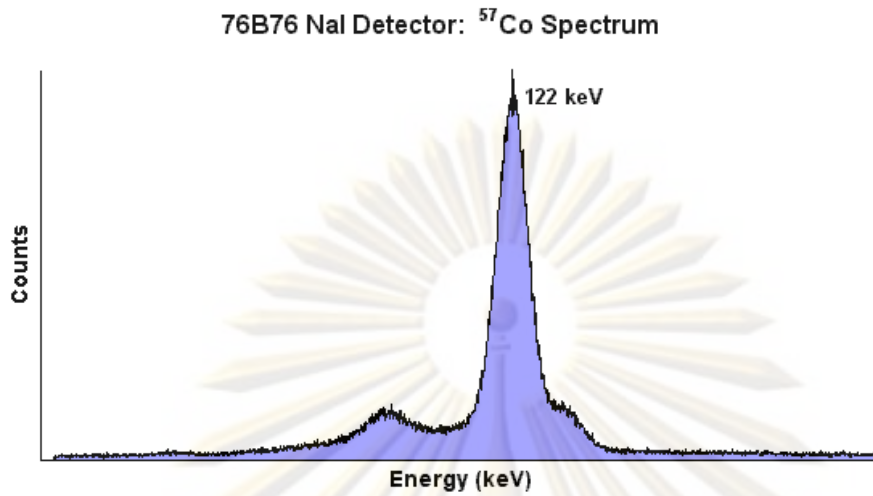
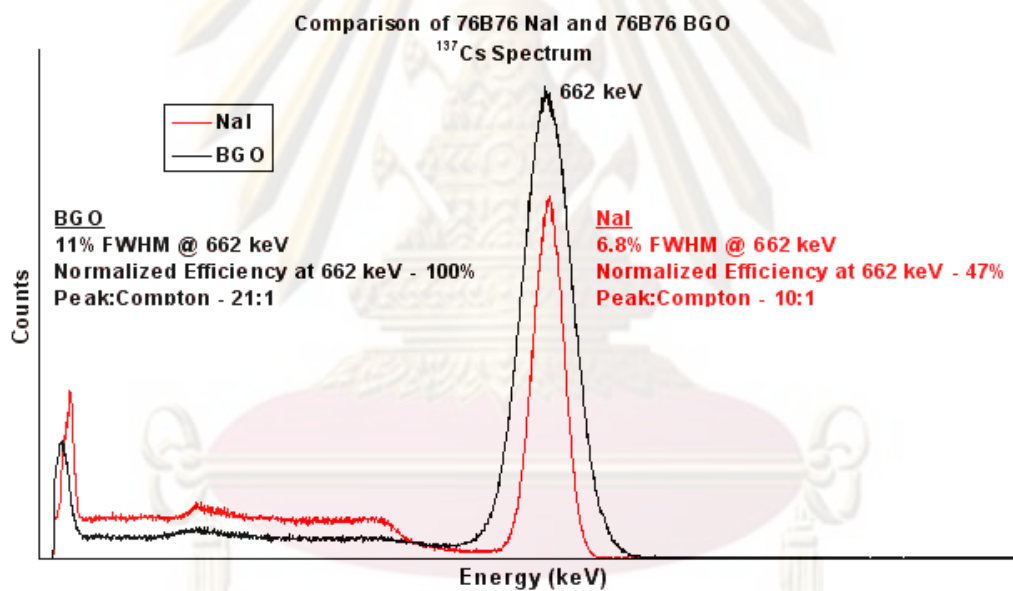


Figure 4. Co-57 spectrum

Figure 5. Comparison of 76 x 76 mm³ NaI:TI and 76 x 76 mm³ BGO

Amptek, Inc.

14 De Angelo Drive, Bedford, MA 01730 U.S.A.

TEL: +1 (781) 275-2242 FAX: +1 (781) 275-3470

E-mail: sales@amptek.com

Appendix E Calculation of intrinsic peak efficiency and peak to Compton ratio

Intrinsic peak efficiency calculation

$$\varepsilon_{\text{int}} = \frac{4\pi N}{\Omega S}$$

N = full energy peak counts.

S = number of radiation quanta.

S = Decay branching ratio × Radioactivity (Ci) × 3.7×10^{10} × time (s)

Ω = solid angle subtended by the detector at the source position. For the common case, a point source located along the axis of a right circular cylindrical detector is assumed:

$$\Omega = 2\pi \left(1 - \frac{d}{\sqrt{d^2 + a^2}}\right)$$

Where d = source-detector distance

a = detector radius

Intrinsic peak efficiency of $\varnothing 10 \times 10 \text{ mm}^3$ CsI:TI at difference energies

Parameters	Co-57	Cs-137	Co-60
Peak energy (keV)	122	662	1332
Decay branching percentage (%)	85.6	85.1	100
Radioactivity (μCi)	17.20	0.5921	0.5775
Source to detector distance (mm)	155	2	2
Detection time (s)	712	827	1374
Full energy peak counts (N) × 10^3	159	121	33
Solid angle (Ω)	0.0043	3.9497	3.9497
Number of radiation quanta (S) × 10^6	824	16	29
Intrinsic peak efficiency (%)	56.68	2.50	0.36

Intrinsic peak efficiency of $\text{Ø}22 \times 22 \text{ mm}^3$ CsI:TI at difference energies

Parameters	Co-57	Cs-137	Co-60
Peak energy (keV)	122	662	1332
Decay branching percentage (%)	85.6	85.1	100
Radio activity (μCi)	17.20	0.5921	0.5775
Source to detector distance (mm)	285	15	10
Detection time (s)	777	674	1132
Full energy peak counts (N) $\times 10^3$	186	126	82
Solid angle (Ω)	0.0058	1.2164	2.0566
Number of radiation quanta (S) $\times 10^6$	423	13	24
Intrinsic peak efficiency (%)	94.90	10.35	2.08

The following is an example of intrinsic peak efficiency calculation for scintillator with 22 mm diameter. The radioactive Cs-137 source of 662 keV energy with activity of 0.59 μCi and source to distance at 15 mm were used. The number of pulses of full energy peak was recorded at 125,903 counts in 674 seconds. The intrinsic peak efficiency can be calculated from:

$$S = 0.899 \times 0.5921 \times 10^{-6} \times 3.7 \times 10^{10} \times 674 = 13,274,445$$

$$\Omega = 2\pi \left(1 - \frac{15}{\sqrt{15^2 + 11^2}}\right) = 1.2164$$

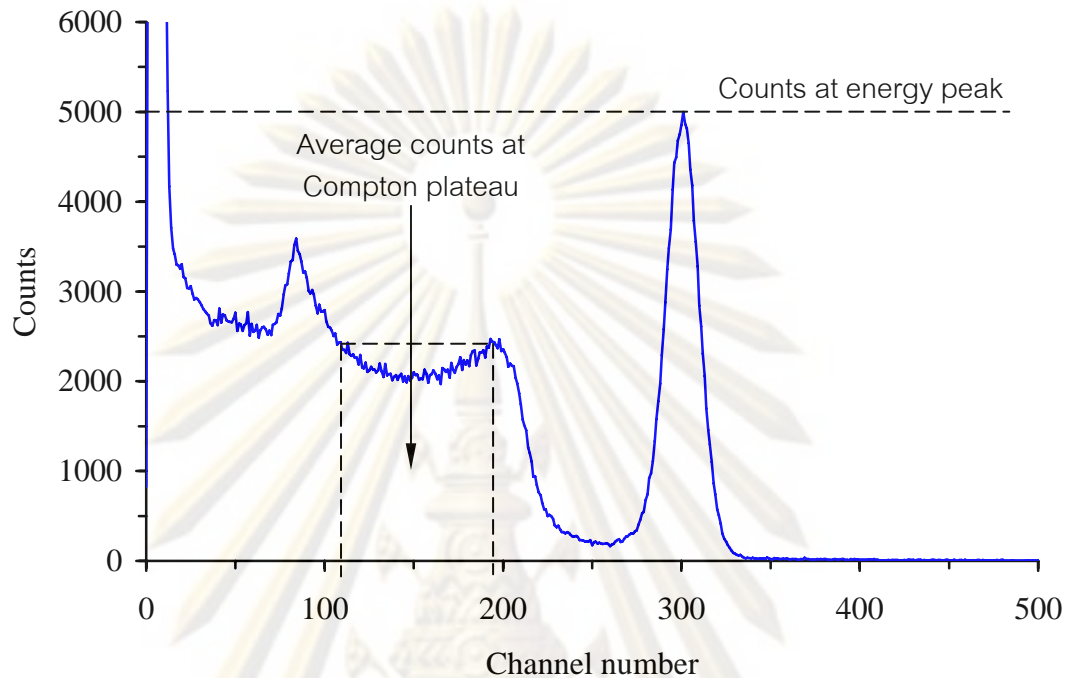
$$\epsilon_{\text{int}} = \frac{4\pi \times 125903}{1.2164 \times 13274445}$$

$$\epsilon_{\text{int}} = 0.0980 \quad \text{or} \quad \epsilon_{\text{int}} = 9.80\%$$

ศูนย์วิทยุแพทยากร
จุฬาลงกรณ์มหาวิทยาลัย

Peak to Compton ratio calculation

$$\text{Peak to Compton ratio} = \frac{\text{Counts at energy peak}}{\text{Average counts at Compton plateau}}$$



Peak to Compton ratios of $\text{Ø}10 \times 10 \text{ mm}^3$ and $\text{Ø}22 \times 22 \text{ mm}^3$ CsI:Tl

Parameters	$\text{Ø}10 \times 10 \text{ mm}^3$		$\text{Ø}22 \times 22 \text{ mm}^3$	
Radioisotope source	Cs-137	Co-60	Cs-137	Co-60
Peak energy (keV)	662	1332	662	1332
Counts at energy peak	5000	1309	5001	3185
Average counts at Compton plateau	2192	2557	1090	2458
Peak to Compton ratio	2.28:1	0.51:1	4.58:1	1.30:1

For an example of the Cs-137 spectrum detected by the CsI:Tl crystal size of $\text{Ø}22 \times 22 \text{ mm}^3$, the counts at energy peak of 662 keV is 5001 and the average counts at Compton plateau is 1090. Thus, the peak to Compton ratio can be calculated as

$$\text{Peak to Compton ratio} = \frac{5001}{1090} = 4.58:1$$

Biography

Mr. Manit Jitpukdee was born on May 2, 1977 in Putthalung, Thailand. I got my Bachelor degree from the Department of Chemical Engineering, Faculty of Engineering, Kasetsart University in 1999 and Master degree from Department of Nuclear Technology, Faculty of Engineering, Chulalongkorn University in 2004. In June 2005, I studied in the Doctoral degree at the Department of Nuclear Technology, Faculty of Engineering, Chulalongkorn University.



ศูนย์วิทยทรัพยากร
จุฬาลงกรณ์มหาวิทยาลัย